Titre: Title:	Solvent-Cast Three-Dimensional Printing of Polylactide Multifunctional Microsystems
Auteur: Author:	Shuangzhuang Guo
Date:	2014
Type:	Mémoire ou thèse / Dissertation or Thesis
Référence: Citation:	Guo, S. (2014). Solvent-Cast Three-Dimensional Printing of Polylactide Multifunctional Microsystems [Ph.D. thesis, École Polytechnique de Montréal]. PolyPublie. https://publications.polymtl.ca/1430/

UNIVERSITÉ DE MONTRÉAL

SOLVENT-CAST THREE-DIMENSIONAL PRINTING OF POLYLACTIDE MULTIFUNCTIONAL MICROSYSTEMS

SHUANGZHUANG GUO

DÉPARTEMENT DE GÉNIE MÉCANIQUE

ÉCOLE POLYTECHNIQUE DE MONTRÉAL

THÈSE PRÉSENTÉE EN VUE DE L'OBTENTION

DU DIPLÔME DE PHILOSOPHIAE DOCTOR

(GÉNIE MÉCANIQUE)

JUIN 2014

UNIVERSITÉ DE MONTRÉAL

ÉCOLE POLYTECHNIQUE DE MONTRÉAL

Cette thèse intitulée:

SOLVENT-CAST THREE-DIMENSIONAL PRINTING OF POLYLACTIDE MULTIFUNCTIONAL MICROSYSTEMS

présentée par: GUO Shuangzhuang

en vue de l'obtention du diplôme de : Philosophiae Doctor

a été dûment acceptée par le jury d'examen constitué de :

M. CARREAU Pierre, Ph.D., président

M. THERRIAULT Daniel, Ph.D., membre et directeur de recherche

Mme HEUZEY Marie-Claude, Ph.D., membre et codirectrice de recherche

M. BARON Luc, Ph.D., membre

M. KAMAL Musa, Ph.D., membre

DÉDICACE

“*To my lovely wife, cheerful son, and beloved family mom, dad, sister and brother*”

ACKNOWLEDGEMENTS

I wish to thank all those who supported me in the completion of this study or helped me in any way during my living in Canada.

First of all, I would like to express the deepest appreciation to my supervisor, Professor Daniel Therriault and Professor Marie-Claude Heuzey, who provide me with fundamental advices. I am very grateful for their continued support throughout the whole projects as well as the many interesting discussions. I am also very grateful for the things that I learnt from them; not only the scientific matters, but also lots of knowledge which are very helpful in all aspects of my life. It had been a true privilege to learn from such competent and sincere supervisors.

I would also like to send a heartfelt acknowledgment to the members of Laboratory of Multiscale Mechanics (LM^2) research group who made the working place a fascinating area. My especial thanks are due to Dr. Rouhollah Dermanaki Farahani for his encouragements, advices and many things that I have learnt from him during all my study.

I like to acknowledge financial support from CSC (China Scholarship Council).

Finally, I could not have accomplished this without all the supports of my family, especially my lovely wife, Xiao-Yang. They are the driving forces behind all of my successes. To them I tribute a fervent thanks.

RÉSUMÉ

Les progrès faits en termes de microstructuration tridimensionnelle (3D) permettent la configuration d'architectures complexes, qu'elles soient faites de polymère seul ou renforcé. Ces architectures peuvent participer à l'essor de nouvelles applications technologiques ou améliorer des applications existantes.

Plusieurs stratégies et technologies ont récemment émergé pour la fabrication rapide et peu coûteuse de micro-appareils 3D faits à base de polymères thermoplastiques. La déposition par fusion ou « fused deposition modeling » est la méthode la plus populaire pour la fabrication de produits 3D à base de thermoplastiques. Par contre, la dégradation thermomécanique causée par les hautes températures du procédé de déposition et par la haute viscosité de la plupart des polymères fondus peut rendre difficile l'application de cette méthode aux nanocomposites. En effet, les nanoparticules augmentent de façon significative la viscosité du matériau. Bien que le procédé d'électro-filage ou « electrospinnig » ait été utilisé pour produire des structures polymériques diverses, la complexité des structures 3D obtenues est relativement limitée. L'objectif général de cette thèse est le développement d'une technique de fabrication permettant d'élaborer des structures 3D à base de matériaux nanocomposites constitués d'un polymère thermoplastique, le polylactide (PLA), et de nanotubes de carbone multi-parois.

Cette thèse présente le développement d'une méthode de fabrication par écriture directe qui étend significativement les possibilités offertes par la microfabrication de structures 3D en nanocomposites thermoplastiques. Cette méthode commence par la déposition robotisée d'un filament de polymère dissout dans un solvant par micro-extrusion. L'évaporation rapide du solvant permet la solidification directe du filament extrudé. On peut donc donner à celui-ci des formes complexes en 3D comme par exemple des filaments, des tours, des échafaudages ou des spirales à forme libre. De plus, cette technique par évaporation de solvant a été démontrée comme étant abordable, hautement flexible et robuste pour la fabrication de microsystèmes dont des fibres microstructurées à haute ténacité, des canaux microfluidiques ou des micro-antennes.

Nous avons également caractérisé le procédé en utilisant des solutions de PLA pour analyser l'écoulement des solutions, la cinétique d'évaporation du solvant et les effets des paramètres du procédé sur la cristallisation des filaments extrudés. La rhéologie rotationnelle montre un comportement presque Newtonien des solutions de PLA pour des taux de cisaillement faibles ou modérés. Pour des taux de cisaillement plus élevés, des analyses d'écoulement capillaire montrent un comportement rhéofluidifiant. Les essais d'évaporation de solvant suggèrent que la diffusion de ce dernier à l'intérieur du filament est le facteur dominant du retrait de solvant du polymère. Avec l'augmentation de la complexité géométriques des microstructures déposées allant d'un filament 1D, un réseau de fibres 2D jusqu'à un échafaudage 3D et une spirale à forme libre, le filament imprimé doit se solidifier de plus en plus rapidement. C'est pourquoi une cartographie des paramètres du procédé de fabrication a été définie. Celle-ci démontre que la plage utile des paramètres devient de plus en plus restreinte avec l'augmentation de la complexité géométrique. Les résultats de calorimétrie différentielle à balayage ont aussi montré que l'évaporation plus lente du solvant augmente la propension du PLA à compléter sa cristallisation pendant la phase de séchage, ce qui peut être souhaitable dans certains cas.

Des nanocomposites composés de PLA renforcés de nanotubes de carbone multi-parois ont été préparés en combinant des mélanges à l'état fondu et en solution. Les solutions de PLA/nanotubes ont démontré un comportement rhéofluidifiant. L'amplitude de leur viscosité a été affectée par la présence de nanotubes lorsque les taux de chargement étaient supérieurs à 1 % par unité de poids. La viscosité apparente était 40% supérieure à celle du PLA lorsque le taux de charges atteignait 5 % en poids.

Finalement, des structures nanocomposites 3D multifonctionnelles à forme libre ont été imprimées grâce à la technique développée dans cette thèse. Leurs fonctionnalités ont été examinées dans le cadre d'une application d'un détecteur de liquide testé à l'aide de quatre solvants organiques (i.e., acétone, toluène, éthyle acétate et l'éthanol). L'augmentation de surface de contact induite par la géométrie hélicoïdale du détecteur de liquide a permis une excellente

sensibilité et sélectivité, même pour des temps d'immersion très courts. Lors de ces essais, la sensibilité était principalement gouvernée par la combinaison du paramètre d'interaction polymère/solvant et par la pression de vapeur du solvant. Les essais lors de longues immersions ont aussi démontré que la sensibilité du détecteur était principalement fonction du paramètre d'interaction polymère/solvant.

La technique d'impression 3D par évaporation de solvant développée dans cette thèse ouvre de nouvelles perspectives pour la création de microstructures 3D multifonctionnelles pouvant trouver de nombreuses applications dans des micro et nano systèmes pour des mesures de précision, dans la détection de polluants, la fabrication d'échafaudages pour la croissance tissulaire ou dans le contrôle à distance d'appareils autonomes.

ABSTRACT

Three-dimensional (3D) structures fabricated from polymers and their nanocomposites may find widespread technological applications which either require, or could benefit from, the ability to pattern micro-sized features in complex 3D architectures. Several strategies and technologies have recently emerged to rapidly and cost-effectively fabricate thermoplastic polymer-based 3D microdevices. Fused deposition modeling (FDM) stands out as the most popular procedure to manufacture 3D products. However, the thermal degradation caused by high processing temperatures and the high viscosity of most polymer melts may prevent the application of this technique to functional nanocomposite devices, since nanoparticles can significantly increase material viscosity. Also, electrospinning has been used to produce fiber-based polymer structures but is limited in terms of 3D structure complexity. The overall objective of this thesis is the development of a manufacturing technique allowing the fabrication of 3D structures of thermoplastic polymers and their nanocomposites.

This thesis reports the development of a direct-write fabrication technique that greatly extends the fabrication space for 3D thermoplastic nanocomposite structures. The solvent-cast 3D printing of microstructures uses a thermoplastic polymer or its nanocomposite solution as the ink. The method employs the robotically-controlled micro-extrusion of a filament combined with a rapid solvent evaporation. Upon drying, the increased rigidity of the extruded filament enables the creation of complex 3D shapes such as filaments, towers, scaffolds and freeform spirals. For a typical circular spiral, the average coil diameter was 966 $\pm$ 6 μm and the average pitch was 530 $\pm$ 25 μm. Both values were very close to the programmed deposition path (*i.e.*, coil diameter of 1.0 mm, pitch of 500 μm). The layer-by-layer scaffold and the micro-cup were almost identical to their respective programmed deposition paths because the printing layer was supported by the underlying layer. The main limitation remains the freeform deposition of sharp turns which lead to some geometric discrepancies. Furthermore, the solvent-cast printing technique has been demonstrated to be a low-cost, highly flexible and powerful fabrication route of microsystems

including high-toughness microstructured fibers, microfluidic channels, and micro antennas.

We performed a comprehensive characterization of the process using PLA solutions by analyzing the flow behavior of the solutions, the solvent evaporation kinetics and the effects of process-related parameters on the crystallization of the extruded filaments. Rotational rheometry at low to moderate shear rates showed a nearly Newtonian behavior of the PLA solutions, while capillary flow analysis based on process-related data indicated shear-thinning at higher shear rates. Solvent vaporization tests suggested that the internal diffusion of the solvent through the filaments controlled the solvent removal of the extrudates. As the fabrication complexity of micro geometries evolves from one-dimensional (1D) filament, two-dimensional (2D) fiber array to 3D scaffold and freeform spiral, the rigidity of the filament needs to increase faster as well. Thus the processing map, which has been defined, gets narrower for the most complex geometries. The results of differential scanning calorimetry also revealed that slow solvent evaporation could increase the ability of PLA to complete its crystallization process during the filament drying stage.

Subsequently, PLA/MWCNT composite solutions were prepared using a combination of melt mixing and solution processes. The inks of PLA/MWCNT solutions exhibited shear-thinning, and the magnitude of the apparent viscosity was affected by the presence of the nanoparticles for MWCNT loadings of 1 wt% and above. The process-related viscosity of the ink with 5 wt% MWCNT loading was 40% higher than that of the neat PLA ink.

Finally, 3D multifunctional helical liquid sensors were fabricated using the solvent-cast printing technique with PLA nanocomposite solutions as inks. The performance of these sensors was examined in four different organic solvents (i.e. acetone, toluene, ethyl acetate, and ethanol). The structural feature of liquid trapping prompted the helical-shaped liquid sensor with excellent sensitivity and selectivity, even for very short immersion time in the solvent, where the sensing response was governed by a combination of the polymer/solvent interaction parameter and the solvent vapor pressure. In addition, it was found that the sensing ability of the helix was mainly determined by the polymer/solvent interaction parameter in long immersion tests.

The solvent-cast 3D printing manufacturing technique demonstrated here open new prospects for the fabrication of 3D multifunctional microstructures that could find applications in micro- and nanoscale systems such as precision measurements, pollutants detection in natural environments, tissue engineering scaffolds and remote-controlled smart devices.

TABLE OF CONTENT

LIST OF TABLES

LIST OF FIGURES

LIST OF APPENDICES

INTRODUCTION

Background and problematic

There has been a lot of interest in the development of conductive polymer nanocomposites (CPN) where conductive nanoparticles are dispersed within insulating polymer matrices to generate a new kind of advanced materials [1-3]. After being first reported by Iijima in 1991[4], carbon nanotubes (CNT) were investigated as fillers for CPN because of their great properties, lightweight and that the relatively low percolation threshold that can be achieved due to their high aspect ratio. Also the CPN can exhibit multifunctional properties such as high mechanical strength and stiffness, along with thermal and electrical conductivity at relatively low CNT loadings, which make them suitable for a broad range of potential applications such as sensors [5], actuators [6], electromagnetic interference shielding [7], as well as energy and gas storage [8].

These applications either require, or could benefit from, the ability to pattern micro-sized features in complex three-dimensional (3D) architectures. Direct-write (DW) assembly is a 3D printing technique that employs a computer-controlled translation stage, which moves an ink-deposition nozzle, to create materials with prescribed 3D architecture and composition [9]. Many ink materials have been employed such as organic fugitive inks [10], concentrated polyelectrolyte complexes [11], colloidal suspensions [12-14], hydrogels [15, 16] and thermoset polymers [17]. These inks solidify through different mechanisms such as viscoelastic recoil [10], coagulation in reservoir [11], suppression of repulsive forces [12], and UV polymerization [15-17].

As a thermoplastic polymer, polylactide (PLA) is one of the most popular bio-based materials because it is widely available commercially, biodegradable, biocompatible and has a relative high-strength, high-modulus and good processability [18]. Several strategies and technologies using PLA to fabricate microscale 3D geometries have been developed. For example, a fused deposition modeling (FDM) method can elaborate PLA solid objects due to the material rigidity increase after the temperature-triggered phase transition from molten to solid state [19]. However this method exhibits limited precision of the printed features, and the high viscosity and/or thermal degradation at high temperature of the PLA melt may restrict this approach. In addition, two other methods including surface tension driven direct-write [20] and soft lithographic approaches [21] were reported to fabricate 3D PLA scaffolds for tissue

engineering. However, these techniques were unable to build complex or freeform 3D structures. Thus, new fabrication methods of multifunctional microstructures using thermoplastic polymers and their nanocomposites would foster larger utilization of their based materials in potential applications.

Organization of the thesis

This thesis is based on three articles that have been published or submitted to scientific journals and comprises the following sections:

Chapter 1 provides a critical literature survey of PLA properties, factors in the preparation of electrically conductive nanocomposites, the various microfabrication techniques, and the CPN used as liquid sensors. Research objectives and the coherence between the specific objectives and the three articles are described in Chapter 2. The main achievements of the thesis are given in the format of three peer reviewed scientific papers in Chapter 3, 4, and 5. Chapter 2 (Article 1) reports on the fabrication of microstructures using the solvent-cast 3D printing method and PLA solutions as the inks. This article mainly focuses on demonstrating the new 3D printing technique to be low-cost, highly flexible and powerful fabrication route by different microsystems including high-toughness microstructured fibers, microfluidic channels, and micro antennas. Chapter 4 (Article 2) deals with the effects of process-related parameters (i.e., applied pressure, nozzle diameter and robot velocity) and material-related parameters (i.e., PLA content, rheology, solvent evaporation) on the processability and the crystallinity of the fabricated filaments. In Chapter 5 (Article 3), PLA/MWCNT nanocomposites have been developed and used to fabricate multifunctional 3D helical liquid sensors. Finally, a general discussion of the main results is presented in Chapter 6, while conclusions and recommendations are stated in Chapter 7.

CHAPTER 1: Literature Review

A multifunctional material is a composite that simultaneously perform (a) multiple structural functions, (b) combined non-structural and structural functions, or (c) both [22]. Structural functions include mechanical properties like strength, stiffness, fracture toughness, and damping. Non-structural functions include electrical and/or thermal conductivity, sensing and actuation, energy harvesting/storage, self-healing capability, electromagnetic interference (EMI) shielding, recyclability and biodegradability [23]. Nanocomposite materials, defined as multiphase materials that incorporate nanosized fillers into a polymer matrix, have drawn specific interest in the development of multifunctional material systems due to their unique mechanical, thermal and electrical properties [24].

Before processing the nanocomposites in their potential applications, it is important to have a basic understanding of the properties of polymer matrix, which is polylactide (PLA) in this project. Then the factors including nanofiller type, polymer matrix and processing method for the preparation of electrically conductive nanocomposite are discussed. Afterwards, the manufacturing techniques for the fabrication of 3D microdevices for different applications are reviewed. Finally, a literature survey concerning the utilization of nanocomposites for sensor applications is discussed.

1.1 Polylactide

Table 1.1 Physical and mechanical properties of selected thermoplastic polymers [25].

Properties	PLA	PET	PP	PS	PEEK
Density (g cm^{-3})	1.25	1.37	0.9	1.05	1.32
Young's modulus (MPa)	350-2800	2800–3100	1100-1550	3000-3500	3600
Tensile strength (MPa)	10-60	55–75	30-38	32-60	90-100
Elastic limit (%)	1.5-380	50–150	200-700	2.8-4	50
Glass temperature (℃)	60-65	75	-10	80-98	143
Melting point (℃)	173-178	254	165	-	343
Thermal Conductivity (W mK^{-1})	0.13	0.24	0.12-0.22	0.14-0.16	0.25
Water absorption (%)	0.5-50	0.16	0.01	0.1	0.5

Polylactide (PLA) is a compostable polymer derived from renewable sources (mainly starch

and sugar) and viewed as a promising material to reduce solid waste disposal. Moreover, PLA has relatively high mechanical properties when compared to other thermoplastic polymers (Table 1.1) and is considered as a good candidate material for food packaging and for other consumer products [26].

PLA is formed either by direct condensation of lactic acid or via the cyclic intermediate dimer (lactide), through a ring opening process [18]. Lactic acid is simple chiral molecule which exists as two optical isomers, *L*- and *D*-lactic acid. The majority of lactic acid from biological sources exists as *L*-isomer. It is possible to control the ratio and sequence of *L*- and *D*-lactic acid units in the final polymer by controlling residence time and temperature in combination with catalyst type and concentration in the polymerization process [27].

1.1.1 Thermal properties of polylactide

As a thermoplastic polymer, semicrystalline PLA exhibits a glass transition (T_g) and melting temperature (T_m). The T_g of PLA varies according to the molecular weight (M_n) and the optical purity (OP, the fraction of the isomer sequences in the whole molecular chain) of the polymer. Lim et al. found that the T_g increases with molecular weight, and at infinite molecular weight reaches maximum values of 60.2, 56.4 and 54.6 ℃ for PLA consisting of 100, 80, and 50 % *L*-stereoisomer contents, respectively [28]. However, Ahmed et al. reported that optically pure polylactide, poly(*L*-lactide) (PLLA) and poly(*D*-lactide) (PDLA), are crystalline polymers with T_g ~ 66 ℃, while the atactic polymer, poly-(*DL*-lactide) is an amorphous material (occurring about when OP < 0.78) with a glass transition temperature of 50-57 ℃ [29].

Typical T_m values for PLA range between 130 and 160 ℃, and are also a function of its OP. The maximum practical obtainable T_m for stereochemically pure PLA is around 180 ℃, with an enthalpy of 40-50 J g^{-1}. As the OP decreases, the T_m decreases by as much as 50 ℃ [28]. Besides, it was reported that the T_m and enthalpy of crystal fusion of PLLA increased as M_n increased from 1100 to 27500 g mol^{-1} [29].

1.1.2 Thermal degradation and biodegradation of polylactide

PLA has a tendency to undergo thermal degradation in the molten state, which can be due to several reasons such as (a) hydrolysis by trace amounts of water, (b) zipper-like depolymerization, (c) oxidative, random main-chain scission, and (d) intermolecular transesterification to monomer

and oligomeric esters [30]. PLA is a hygroscopic polymer where amorphous parts of the polymer tend to absorb much more water than that of crystalline phase [31]. Rheological measurements showed that the thermal degradation of PLA is accelerated when the moisture content of the polymer increased and optimal drying conditions are required to reduce the thermal degradation during melt mixing [32].

In the presence of catalyst during thermal degradation, PLA will undergo a zipper-like depolymerization [32]. The catalysts promote the cleavage of ester bonds in the polymer backbone, facilitating the fragmented polymer ends to undergo chain backbiting and thus depolymerization. The effects of the catalyst type and concentration on the degradation has been reported [33].

PLA biodegradation has been found to be dependent of a range of factors such as molecular weight, crystallinity, purity, temperature, pH, presence of terminal carboxyl or hydroxyl groups, water permeability, and additives acting catalytically that may include enzymes, bacteria or inorganic fillers [34]. However, PLA biodegradation is relatively slow in most cases, and the loss of strength is usually observed after several weeks, with complete biodegradation often taking years [35]. Acceleration of hydrolytic degradation may be achieved in several ways including high degradation temperatures, high acidity degradation media, and catalysts [30].

1.1.3 Rheological properties of polylactide

Rheological properties are used to evaluate the behavior of thermoplastics during processing operations. Intrinsic factors affecting the flow characteristics of PLA are molecular weight and distribution, degree and type of branching (though commercial PLA grades are mostly linear), optical composition, optical block length distributions, and melt stability.

Melt rheological properties of PLA are highly dependent on temperature, molecular weight and shear rate. Melt viscosity of high-molecular-weight PLAs is in the order of 500-1000 Pa·s at shear rates of 10-50 s^{-1} [36]. As shear rates increase, the viscosity of the melt decreases considerably and the polymer melt exhibits a shear-thinning behavior. However, low molecular weight PLA (~40,000 g mol^{-1}) shows Newtonian-like behavior at shear rates typical of film extrusion [37]. The zero shear viscosity, (η_0), for linear PLA is found to roughly scale with the expected 3.4 to 4 power with molecular weight [38, 39]. Besides, Lehermeier found that both η_0

and shear thinning increased with the addition of branched PLA. For both linear and branched PLA, the shear viscosity decreases as the temperature increases [40].

Most of the researches about the rheological properties of PLA dissolved in solvents focus on the intrinsic viscosity ([η]) of dilute solution, which is frequently evaluated to determine the molecular weight, chain flexibility, and defining solvent quality. The relationship between viscosity and molecular weight of PLA in dilute solution is commonly modeled using the Mark-Houwink equation:

$$[\eta] = K \times M_v^a \tag{1.1}$$

where [η] is the intrinsic viscosity, K and a are constant values, and M_v is the experimental viscosity-average molecular weight. The Mark-Houwink equation is dependent on the type of PLA, the solvent used, and the temperature of the solution [28].

1.1.4 Crystallization behavior of polylactide

The physical, mechanical and barrier properties of PLA are dependent on the solid-state morphology and crystallinity. Essentially, the crystallization behavior of PLA depends on the thermal history, amount and type of additives and stereo sequence distribution, and OP [29]. By measuring the heat of fusion ΔH_m and heat of cold crystallization ΔH_c, the degree of crystallinity can be calculated based on the following equation:

$$\chi_c = \frac{\Delta H_m - \Delta H_c}{\Delta H_m^0} \times 100 \tag{1.2}$$

where ΔH_m^0 (93.6 J g^{-1}) is the enthalpy of fusion of 100% crystalline PLA [41].

The process of quenching the optically pure PLA from the melt phase (e.g., during injection molding process) may lead to a quite amorphous polymer. Results from the literatures showed that quenching the polymer from melt at high cooling rate resulted in an large cold crystallization peak on the differential scanning calorimetry (DSC) thermogram and a lower crystallinity, while slow cooling produced a polymer with higher crystallinity with much lower enthalpy of cold crystallization [30, 42, 43]. The tendency for PLA to crystallize upon reheat also depended on the heating rate, as well as the OP of the polymer. The attainable percentage of crystallinity decreases with decreasing optical purity, and crystallization is essentially nonexistent when OP < 0.78 [29]. It was reported that PLA with greater than $\sim$ 8% *D*-isomer remained amorphous even after 15h

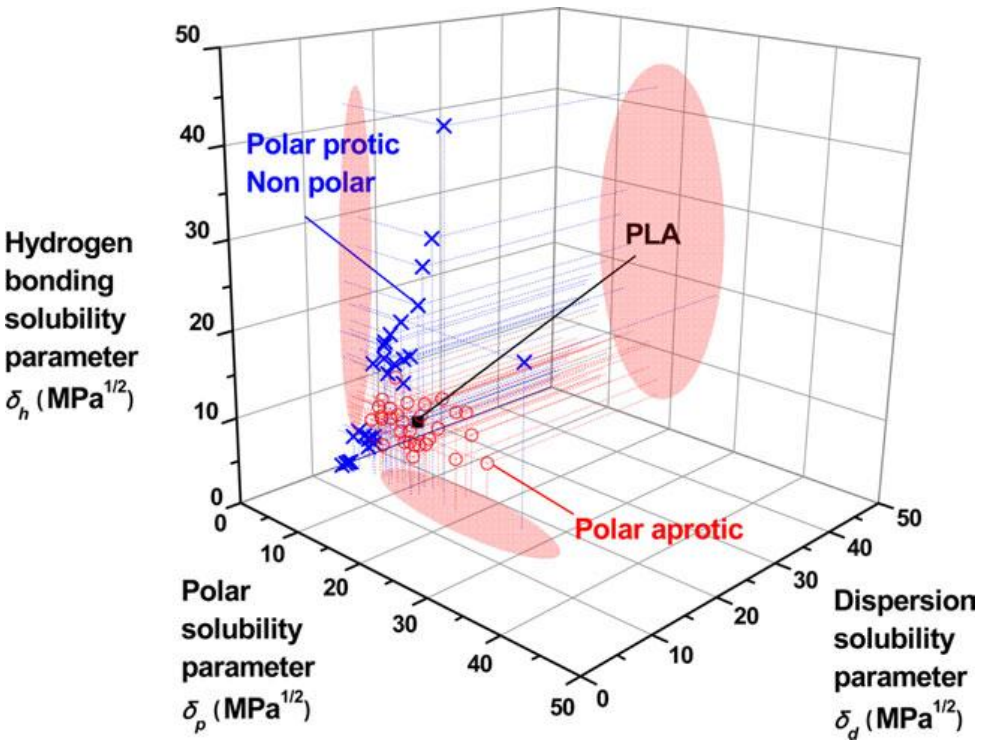

Figure 1.1 Solubility window of PLA in various organic solvents in the Hansen space. Solvent type: polar aprotic (◯), polar protic and non polar (×) [46].

of isothermal treatment at 145 ℃. In contrast, at 1.5% *D*-isomer level, the quenched sample still had a minimal crystallinity [44].

1.1.5 Interaction of polylactide with solvents

Generally, the relative affinity of a polymer and a solvent can be assessed using Hansen solubility parameter δ_T, which can be calculated by

$$\delta_T^2 = \delta_d^2 + \delta_p^2 + \delta_h^2 \quad (1.3)$$

where δ_d, δ_p and δ_h are, respectively, the dispersive, polar and hydrogen bonding contributions of the total solubility parameter [45]. The solubility parameter of PLA was 21.2 MPa$^{1/2}$ [46]. Basically, the closer are the values of δ_T of the polymer and the solvent, the better is the affinity between each other. Sato et al. systematically investigated the effects of 60 organic solvents on PLA (Figure 1.1), and found that PLA was insoluble in 11 of 16 polar solvents (protic acids and alcohols), 9 of 11 nonpolar solvents (aromatic hydrocarbons and paraffins), but was soluble in 28 of 32 aprotic solvents (amines and esters) [46].

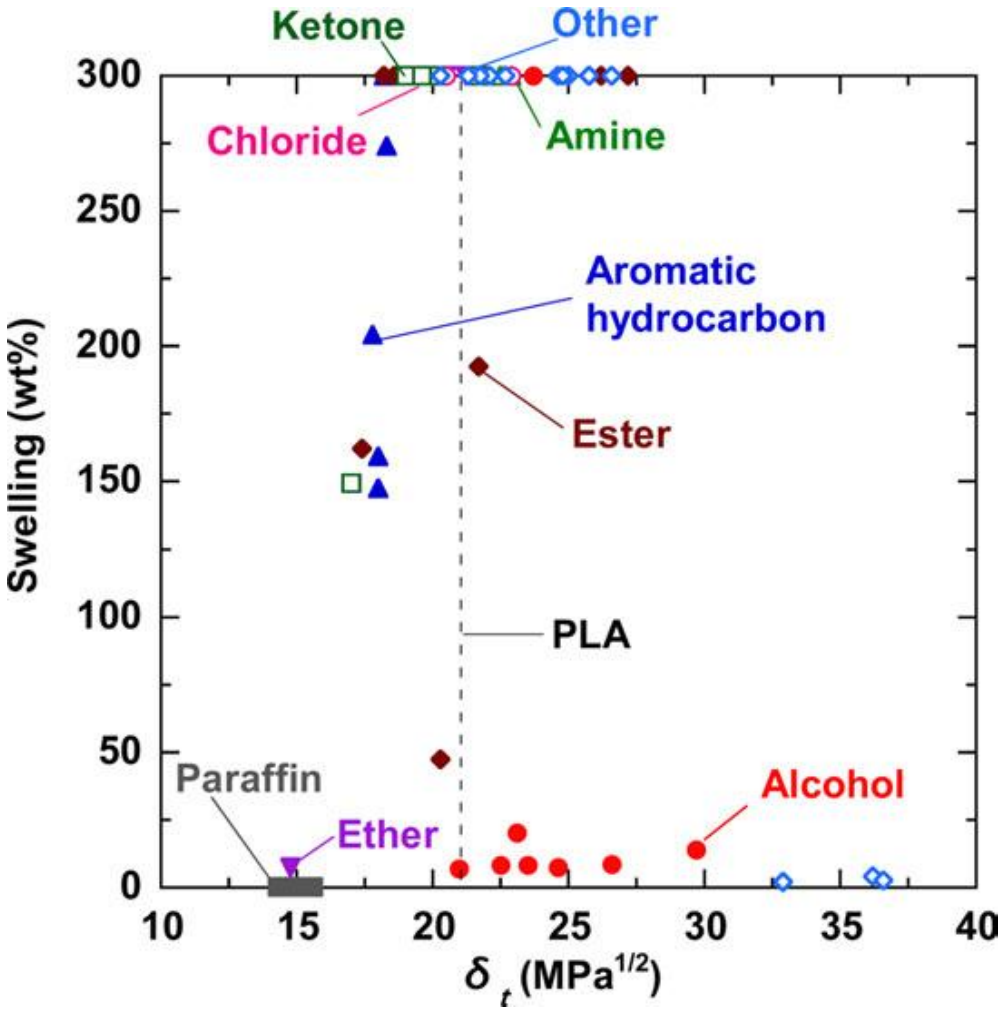

Figure 1.2 Relationship between swelling and total Hansen solubility parameter δ_t. Organic solvent: alcohol (●), paraffin (■), aromatic hydrocarbon (▲), ester (◆), ether (▼), chloride (◯), ketone (□), amine (△), and others (◇) [46].

The relationship between swelling and δ_t is shown in Figure 1.2 [46]. The solvents for which the solubility parameter is near 21.2 $MPa^{1/2}$ exhibited greater swelling. Swelling at and above 300 wt% means the solvents could dissolve or strongly swell PLA. Among the three Hansen solubility parameters, the hydrogen bonding solubility parameter more effectively reflects the solubility of PLA, that explains why the swelling of alcohols is very low even if its δ_t is close to 21.2 $MPa^{1/2}$.

1.2 Electrically conductive thermoplastic nanocomposites

1.2.1 Fundamentals of electrically conductive nanocomposites

Electrical conductivity may be one of the most important non-structural functions for the nanocomposite, but the most widely used polymer matrix materials such as PLA are typically poor conductors because of their very low concentration of free charge carriers. Various conductive composites were developed by adding high aspect ratio electrically conductive nanofillers such as single-walled carbon nanotubes (SWCNTs) [26, 47, 48], multi-walled carbon nanotubes (MWCNTs) [49-51], graphene [52-54], and metallic nanowires [4, 55, 56] into polymer matrices. The increase of the conductivity can be attributed to the formation of conductive pathways when the filler content exceeds a critical fraction. This critical concentration of the conductive additive is named the percolation threshold [1].

At the percolation threshold (φ_c), the 3D conductive network has not been formed, and thus the composite conductivity is due to tunneling in addition to direct contact between the particles. Tunneling conduction occur when the distance between the filler particles are close enough, roughly less than 10 nm. Above the percolation threshold, the filler forms a continuous network inside the polymer matrix, and the further increase in the filler loading usually has no significant effect on the composite electrical conductivity [57].

The conductivity and electrical percolation threshold of a composite depend on many factors including nanofiller aspect ratio, dispersion, distribution, and conductivity in addition to the polymer matrix crystallinity and surface tension. Table 1.2 lists a collection of the experimental parameters of electrically conductive thermoplastic nanocomposites. In the table, the polymer matrices are alphabetically arranged. In addition to nanofiller type and manufacturer, dispersion method and solvent in the case of solution processing are specified. Besides, the aspect ratio of nanofiller, density of the matrix (ρ_m) and the filler (ρ_f) are important parameters during processing. Furthermore, the electrical characteristics like φ_c, and the maximum observed conductivity (σ_{max}) at the experimental filler concentration (C) are also listed. All percolation thresholds and filler concentrations are given in weight% (wt%). Wherever the original data were given in vol%, it was converted to wt% using the relation as follows:

Table 1.2 Summary of experimental parameters and properties of different polymer composites.

Matrix[A]	Filler	Solution	Dispersion[B]	Aspect ratio	ρ_m (g cm^{-3})	ρ_f (g cm^{-3})	φ_c (wt%)	σ_{max}(S/m)@ C(wt %)	Ref.
HDPE	Nano Ag	-	MM-TSE		0.95	10.49	70	3E-1@ 75.7	[58]
HDPE	MWCNT	-	MM-TSE	1000	0.92	1.75	1	1E0@ 7	[59]
LDPE	MWCNT	-	MM-TSE	1000	0.92	1.75	2.5	1E-1@ 7	[59]
MXD6	Nano Ag	-	MM-TSE		1.22	10.49	65	2E-1@ 68.2	[58]
PA12	MWCNT,Nanocyl	-	MM-TSE	100	1.01	1.75	1.75	1.4E1 @5	[60]
PAN	MWCNT(Iljin Nanotech)	DMF	SP/SC/MS	-	1.18	1.95	10	1.24E0 @15	[61]
PBT	Nano Ag	-	MM-TSE		1.31	10.49	56	1E-1@ 69.3	[58]
PCL	MWCNT (Baytubes®)	$CHCl_3$	SP/MS/CS	500	1.1	-	5	3.3E+1 @10	[62]
PCL	SWCNT(Elicarb)	$CHCl_3$	SP/US/MS		1.1	1.3	1	10E-5 @1	[63]
PCL/PLA	MWCNT		MM-R/CM	1000	-	1.75	0.98	1E-2@ 4	[64]
PEEK	SWCNT		MM-TSE	-	1.3	1.3	0.5	1E-2@ 1.0	[26]
PEEK	MWCNT		MM-TSE	150	1.3	1.75	1.5	1E2@ 17	[65]
PHBV	MWCNT (Baytubes®)	$CHCl_3$	SP/MS/CS	500	1.25	-	5	1.5E+1 @10	[62]
PLA	MWCNT,Nanocyl		MM-TSE	150	1.25	1.75	0.5	1E1@ 2	[66]
PLA	MWCNT	DMF	SP/MS		1.25	1.75	14	1E-1@ 20	[67]
PLA	MWCNT	Dioxane	SP/MS/US	100	1.25	1.75	0.5	3E-4@ 5	[68]
PLA	MWCNT	-	MM	1000	1.25	1.75	0.5	7.9E+1 @5	[69]
PMMA	MWCNT	$CHCl_3$	SP/US/CS	1000	1.18	1.75	0.74	2.7E+2 @14.1	[70]
PMMA	SWCNT	$CHCl_3$	SP	-	1.2	1.3	0.17	1E4@ 10	[71]
PP	MWCNT (Hyperion)	-	MM-TSE	1000	0.90	1.75	2	1E-1@ 5	[72]
PP	MWCNT	-	MM-R	500	0.9	1.75	1.5	1E0@ 5	[73]
PP	CB(Akzo Nobel)	-	MM-TSE	-	0.9	1.8	2.8	1E2@ 15	[74]
PP	SG(Asbury)	-	MM-TSE	1.7	0.9	2.24	27.1	1.1E3 @80	[74]
PP	MWCNT	-	MM-TSE	1000	0.9	2.0	4.5	2.5E2	[74]

PP	Ag/MWCNT	-	MB/CM	-	0.9	10.49/	1.5	2E-2@2	[75]
PS	MWCNT	Toluene	SP/US/CS	1000	1.05	1.75	0.8	0.9E+2@15.6	[70]
PS	MWCNT (Kentucky U)	DMF/ THF	SP/US/MS/CM	100	1.04	0.6	0.01	1E0@0.07	[76]
PS	MWCNT		MM-TSE/CM	500	0.95	1.75	-	1E-7@5	[7]
PS	CuNW	CH_2Cl_2/ CH_3OH	SP/SC/CM	-	1.04	8.96	2.1	1E4@19.8	[4]
PS	CuNW	CH_2Cl_2	SP/US/CM	71	1.04	8.96	4.1	1E-3@21	[66]
PS	CuNW	-	MM-TSE	51	1.04	8.96	11.6	1E-6@15	[77]
PS	AgNW	Toluene	SP/MS/CM	31	1.04	10.49	0.19	1E-1@4.8	[78]
PS	Sn-Pb alloy	-	BM/CM	-	1.04	8.57	71.1	1E0@81.6	[79]
PS	Ni particle, Bi/Sn alloy	-	MM-SSE	-	1.04	-	78.2	1E4@89.3	[80]
PU	MWCNT,Nanocyl	-	MM-TSE/CM	150	1.29	1.75	0.13	1E0@1	[81]
PU	MWCNT	THF	SP/MS/CS		1.29	1.75	1.0	2E3@15	[82]
P(VDF-TrFE)	NiNW	Acetone	SP/SC/MS/CM	250	1.8	8.91	3.6	1E2@28.6	[83]

A Matrix: HDPE: High density polyethylene, MXD6: Poly(m-xylene adipamide), PA12: Polyamide 12, PAN: Polyacrylonitrile, PBT: Polybutylene terephthalate, PCL: Polycaprolactones, PDMS: Polydimethylsiloxane, PEEK: Poly(ether ether ketone), PHBV: Polyhydroxybutyrate, PMMA: Polymethyl methacrylate, PP: Polypropylene, PS: Polystyrene, P(VDF-TrFE): Poly(vinylidene difluoride)-trifluoroethylene, PU: Polyurethane.

B Dispersion: MM-TSE: Melt mixing with twin screw extruder, SP: solution processing, SC: sonication, MS: mechanical stirring, CS; Casting, US: ultrasonication, MM-R: melt mixing in rheometer, MB: mixed in Brabender, CM: compression molding; BM: mixing in ball mill, MM-SSE: melt mixing with single screw extruder

$$\text{wt\%} = \frac{vol\% \times \rho_f}{vol\% \times \rho_f + \rho_m \times (1 - vol\%)} \tag{1.4}$$

Maximum conductivities of 10,000 S m^{-1} have been reported for PMMA containing 10 wt% $SOCl_2$ treated SWCNT [71], of 2000 S m^{-1} for PU with 15 wt% MWCNT [82] and of 10,000 S

m^{-1} for PS with 19.8 wt% CuNW [4]. The percolation thresholds found for the above mentioned systems were 0.17 wt%, 1 wt% and 2.1 wt% respectively (see Table 1.2).

A power law fit [84], as given in Eq. (1.5), derived from the percolation theory is often used to fit the conductivity (σ) of a polymer filled with conductive particles to the volume fraction (φ) of the particles above the percolation threshold:

$$\sigma = \sigma_0(\varphi - \varphi_c)^t \tag{1.5}$$

where σ_0 is a constant usually assigned to the plateau conductivity of the fully loaded composite and the exponent (t) fits the data and is used to interpret the mechanism of network formation. Generally, t is about 1.1-1.3 for a 2D network system, while a higher value, in the range from 1.6 to 2.0, is obtained when the fillers form a 3D network [85].

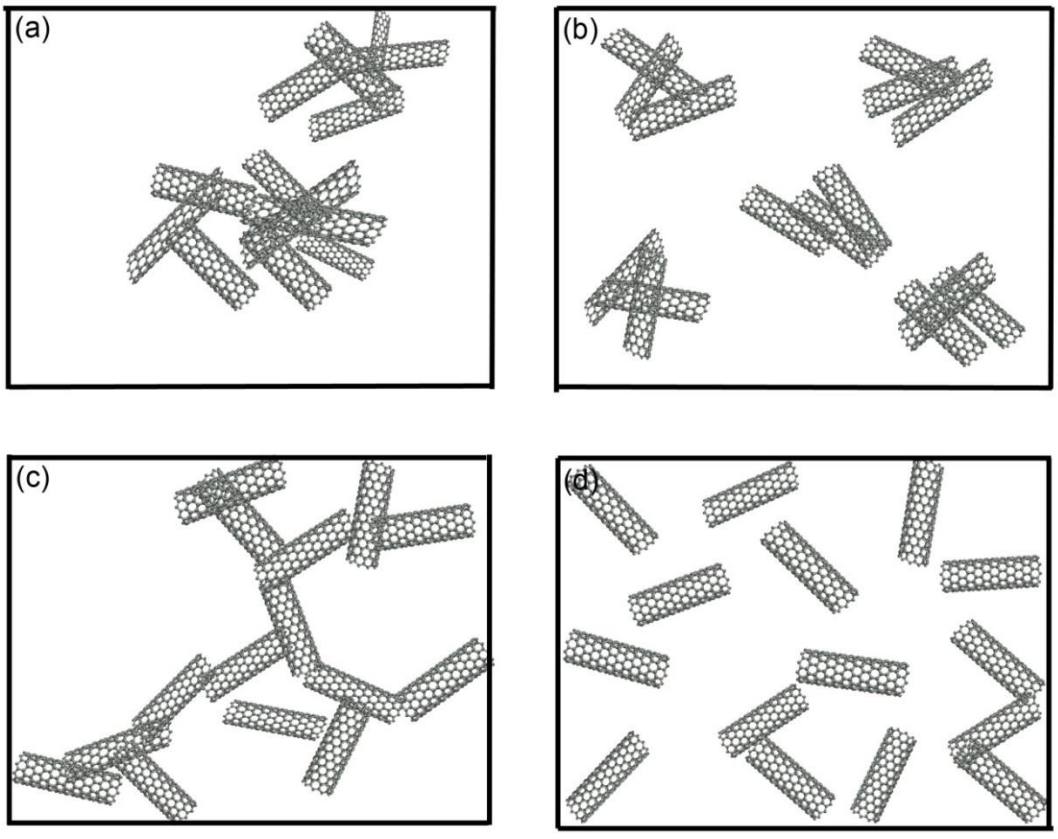

Figure 1.3 Schematic sketches showing the effect of a 1D filler on the conductivity of polymer composite. (a) No conductivity. Bad distribution and dispersion, (b) No conductivity. Good distribution; Bad dispersion, (c) Conductivity. Bad distribution; Good dispersion, (d) No conductivity. Good distribution and dispersion [57].

For the electrically conductive nanocomposite, it is important to reduce the percolation threshold to make those composites economically feasible since the nanofillers are much more expensive than the polymer matrix. Building a conductive network within an insulative matrix at low concentration does not necessarily require a well distributed filler, but a well dispersed filler [57]. Figure 1.3 shows the ability of 1D fibers in percolating a 2D plane based on different dispersion and distribution scenarios. Figure 1.3 (a) and (b) show that the poor dispersion of the fibers prohibits network formation, while Figure 1.3 (d) shows that the perfect distribution of well dispersed fibers increases the gap between the fibers. Only the preferential distribution, Figure 1.3 (c), of well dispersed fibers forms a conductive 2D network.

1.2.2 Effect of filler type

1.2.2.1 Properties of graphene

Pristine graphene is a 2D honeycomb carbon lattice, where the sp^2 hybridized carbon atoms are arranged in a hexagonal fashion in mono-layer. Graphene can be produced in many ways such as mechanical exfoliation [86] and chemical vapor deposition (CVD) [87], and exfoliation of graphite intercalation compounds [88]. Mechanical exfoliation approaches are suitable to maintain the graphene structure, while they are limited by their low production rate. The CVD processes are suitable for large-scale production of mono- or few-layer graphene films. However, the chemical treatment inevitably generates structural defects [79] which disrupt the electronic structure of graphene and change it to be semiconductive [89]. Besides, there are important chemical derivatives of graphene: graphene oxide (GO) and reduced graphene oxide (RGO), which can be synthesized in large quantities through chemical oxidation and exfoliation of graphite and subsequent reduction to graphene [27].

Pure graphene has many excellent properties such as high charge (*i.e.* electrons and holes) mobility (230,000 $cm^2\ Vs^{-1}$) with 2.3% absorption of visible light, high thermal conductivity (3000 W mK^{-1}), high strength (130 GPa), and high theoretical specific surface area (~ 2600 $m^2\ g^{-1}$). The theoretical electrical conductivity is 5×10^7 S m^{-1}. However, due to the presence of oxidized functional group, as-fabricated GO is found to be insulating and the conductivity of RGO can vary from 5 to 50,000 S m^{-1} depending on the degree of reduction [61].

1.2.2.2 Properties of CNTs

CNTs, which were discovered by Iijima around twenty years ago [4], are hexagonal networks of carbon atoms in the shape of seamless cylinder like rolled graphene layers with each end capped with a hemisphere of the buckyball structure. The two main kinds of nanotubes are single-walled (SW) and multi-walled (MW) carbon nanotubes and they are shown in Figure 1.4. SWCNTs are individual cylinders of 1-2 nm in diameter [90]. MWCNTs can be regarded as a coaxial assembly of graphene cylinders, where weak van de Waals forces link the tubes together [91].

Similar to graphene, the strength of the sp^2 carbon-carbon bonds gives CNTs amazing mechanical properties. Their tensile strength, approximately 100-600 GPa, is about ten times higher than that of current high-strength carbon fibers (30-33 GPa) [75], and their density is around 1.3 g cm^{-3}, lower than the density of commercial carbon fibers (1.8-1.0 g cm^{-3}) [59]. The electrical conductivity of CNTs along the tube is unique, ranging from high-conductivity metallic behavior to semiconducting with a large band gap [80], which is determined by its size and chirality. The contact resistance of different nanotubes sensitively varies with the nanotube chirality, the atomic structure in contact regions and externally applied pressure [92].

1.2.2.3 Properties of metallic nanowires

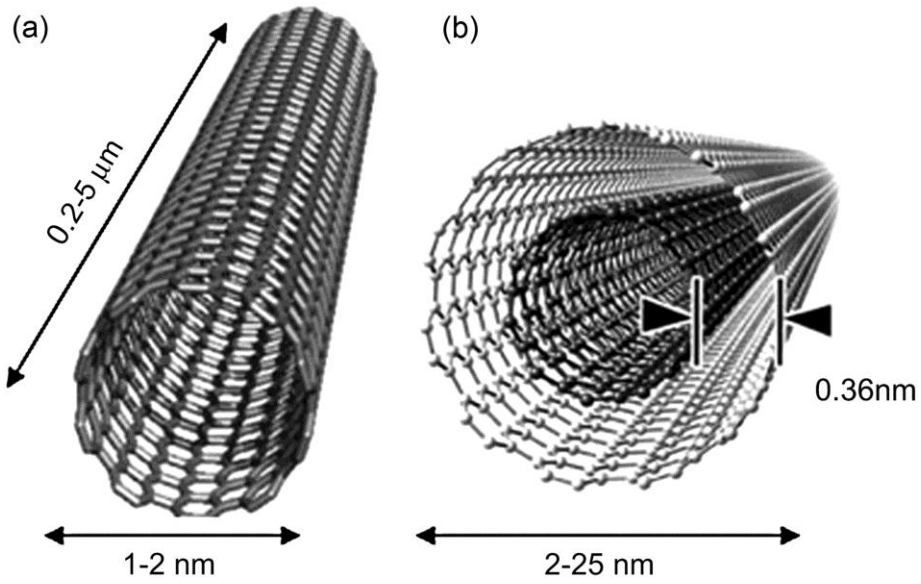

Figure 1.4 Conceptual diagram of SWCNT (a) and MWCNT (b) [77].

Metallic nanowires are another type of promising nanofillers for electrically conductive polymer nanocomposites. Metals featuring high electrical conductivity (10^7 S m^{-1}) such as copper, silver and nickel can also be produced as nanowires. Besides, their aspect ratios, structure, composition, and surface properties can be controlled by the conditions of their synthesis [49]. An important technique to fabricate metallic nanowires is the electrochemical method based on various templates, which include positive, negative, and soft templates [93].

Most of the metallic nanowires, fabricated with the template methods, exhibit the classical Ohm's law behavior and are regarded as classical wires. However, they do possess unique physical properties such as small dimensions, high surface-to-volume ratio, and novel optical and magnetic properties. When the metal nanowires are shorter than a few tens of nm and thinner than a few nm, the conductance is quantized and the wire is referred to as a quantum wire [93].

1.2.2.4 Comparison of the nanofillers

Table 1.3 shows different fillers and their typical properties. MWCNTs feature the lower price and similar properties to SWCNTs, so that MWCNTs are most widely used in different polymer matrices as listed in Table 1.2 The main advantage of the metallic nanowires is the fact that they are able to support high voltage and current intensity in current limiting devices [58]. However, the nanocomposites with CNTs and metallic nanowires exhibit similar φ_c values.

Table 1.3 Typical properties of 1D conductive nanofillers

Property	SWCNT [57]	MWCNT [57]	AgNW [94]	CuNW [49]
Diameter (nm)	0.6-1.8	5-50	100-200	25-200
Aspect ratio	100-10,000	100-10,000	50-200	50-200
Density (g cm^{-3})	~1.3	~1.75	10.49	8.94
Thermal conductivity (W mK^{-1})	3000-6000	3000-6000	429	401
Electrical conductivity (S m^{-1})	10^5-10^6	10^5-10^6	6.30×10^7	5.96×10^7
Tensile strength (GPa)	50-500	10-60	--	--
Tensile modulus (GPa)	1500	1000	83	110-128

From Table 1.2, it is found that different filler types (SWCNT or MWCNT) in the same polymer matrix have no clear impact on the maximum conductivity. Chatterjee et al. found that the values of conductivity in graphene nanoplatelets composite were considerably lower comparing with CNT reinforced composites [60], most probably because commercial graphene nanoplatelets may contain some unreduced graphite oxide, which is non-conducting.

1.2.3 Effect of polymer type

The type of polymers has an obvious effect on the electrical conductivity of composites. A few polymers are intrinsically conductive such as polyaniline [95], polypyrrole [96], and poly(3,4-ethylenedioxythiophene) (PEDOT) [97], but generally they are not. In composite materials, the percolation threshold is affected by polymer surface tension, polarity and crystallinity. Higher polymer surface tension leads to lower filler-polymer interfacial tension. In this situation, the polymer matrix can easily wet the filler particles and thereby distribute them well [57], which increases the percolation threshold. Similarly, higher polymer polarity could lead to better interactions with the nanofillers, which means better distribution of the fillers and a higher percolation threshold.

Compared to amorphous polymer nanocomposite [76, 98, 99], semi-crystalline polymer systems can reach better conductivity and lower percolation thresholds [100-102]. This is a consequence of filler particles being ejected from the crystalline region during crystallization and concentrating in the amorphous region. This phenomenon is called the “double-percolation threshold”. For example, semi-crystalline polystyrene (PS) exhibited a four times large conductivity threshold compared to their amorphous counterparts [102].

1.2.4 Effect of processing method

Processing methods and conditions affect the filler distribution, dispersion, orientation and aspect ratio. The aim of optimum processing conditions is to achieve low percolation threshold and enhance composites properties, including electrical conductivity, which means that the nanofillers should be well dispersed without a reduction of their aspect ratio. Good distribution may not be required to form a conductive network at low filler loading (Figure 1.3) [57]. However, to achieve high mechanical properties, uniform filler distribution is necessary. The most popular methods to prepare thermoplastic nanocomposites are melt mixing and solution

processing as observed in Table 1.2.

1.2.4.1 Melt mixing

Melt mixing is a favorable method for composites preparation because of its simplicity and the wide availability of processing equipment in the polymer industry, which can lead to commercialized products using existing infrastructure. Moreover, the absence of solvent makes it an economically and environmentally sound method. The most common processing techniques are extrusion, internal mixing, injection molding and blow molding [103]. However, in order to obtain the desired dispersion, a high-shear mixing condition is required, which often lead to a decrease in the nanofillers aspect ratio, and degradation of various properties [103]. One of the strategies used to facilitate nanofiller dispersion in a polymer matrix without resorting to destructive shear mixing conditions is grafting the nanofiller before melt compounding. For example, CNTs dispersion in a PMMA matrix was enhanced by first coating CNTs with poly(vinylidene fluoride) (PVDF) before melt mixing [104].

Traditional melt mixing methods can require large quantities of materials (on the order of kg). This is not economical for preparing nanocomposite at the laboratory scale. Thus a miniature twin-screw extruder (or micro-compounder) has been successfully developed to prepare

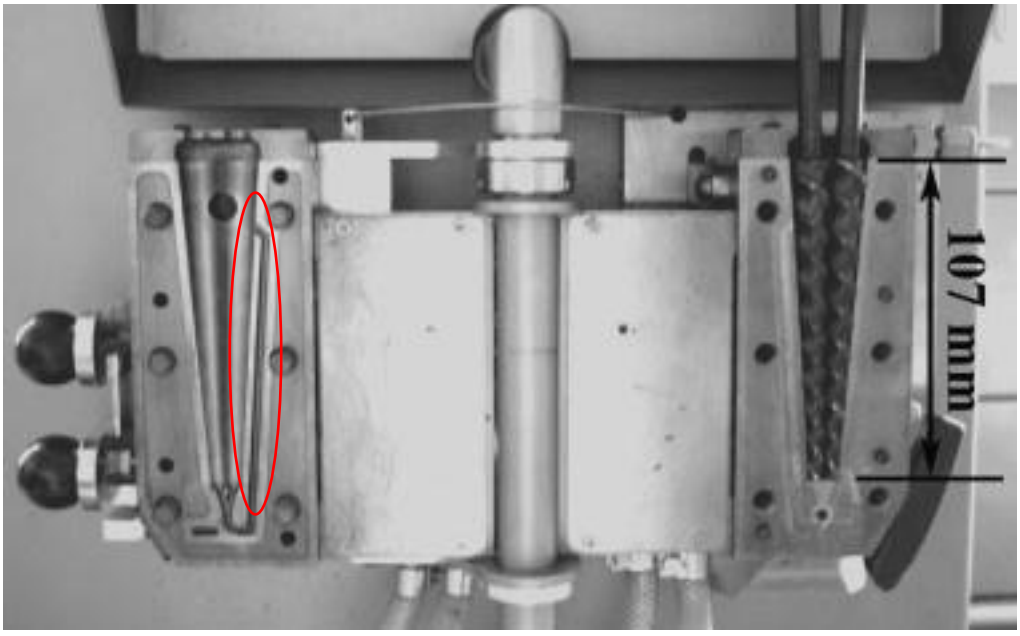

Figure 1.5 Photograph of DSM 5 mL micro-compounder.

thermoplastic nanocomposites from small quantities [77, 105]. There are several companies that provide the micro-compounder including DSM (Heerlen, Netherlands), DACA Instruments (Goleta, CA, USA) and Haake Instruments Inc. (Paramus, NJ, USA). The micro-compounders from different companies all comprise a conical twin-screw extruder with a bypass as shown in the ellipse of Figure 1.5, which allows the melt composite to recirculate so that the material can be mixed for a certain period of time.

The re-circulating channel of micro compounders is helpful to increase the dispersion [59]. Lin et al. prepared PS/copper nanowire composite melt mixed in two DSM micro-compounders, with capacities of 5 and 15 mL (DSM5 and DSM15) [77]. They found that the electrical percolation threshold for the nanocomposite prepared from DSM5 was lower than that from DSM15, but was similar to that of nanocomposites prepared in solution. Villmow et al. investigated the effect of twin-screw extrusion conditions on the dispersion of MWCNTs in a PLA matrix and found that the high rotation speed combined with a screw profile containing mainly mixing elements were highly efficient to disperse the MWCNT [66].

1.2.4.2 Solution processing

Due to the high viscosity and the possible thermal and mechanical degradation of the polymer while using the melt mixing method, solution processing has been also widely used to prepare polymer composites on a laboratory scale. However, this method may be not desirable at the industrial scale because of the necessity to handle large amounts of solvents. Generally, the solution processing includes three steps, (1) dispersing the nanofillers in an appropriate solvent, (2) mixing the nanofillers suspension with a polymer in the same solvent or in a mixed solvent, and (3) evaporating the composite solution [18, 61, 66]. Depending on the evaporating procedure, the composite can be recovered as a thin film, a fiber or a powdery material. In order to achieve excellent dispersion of nanofillers, the selection of the right solvent to dissolve the polymer and to disperse the nanofiller is critical. Besides, some processing aids have been utilized to enhance the dispersion and/or alignment of nanofillers such as sonication [61], ultrasonication [18], magnetic fields [28], and surfactants [106], functionalization and grafting of nanofillers [66, 107].

The interaction between functionalized CNT and solvent allows for a better dispersion. Rizvi et al. prepared a carboxylated MWCNT/PLA composite by the solution casting method using two different solvents, chloroform and 1,4-dioxane [68]. The electrical percolation

threshold of the nanocomposite prepared in 1,4-dioxane was found to be lower than that prepared in chloroform, which was due to the chemical interactions between the carboxylated MWCNT and 1,4-dioxane. Moreover, a homogeneous dispersion of carboxylated MWCNT was successfully achieved in polyurethane (PU) matrix due to hydrogen bonds between C=O group of the PU chain and COOH groups of the MWCNT [108].

1.3 Fabrication of 3D nanocomposite microstructures

1.3.1 Microfabrication techniques

Multifunctional 3D micro-devices have been extensively explored for applications in electronic devices, chemical and biological sensors [109], catalysis and electrocatalysis, energy devices [110], microwave absorption and EMI shielding [7], electrorheological fluids and biomedicine [111]. In order to fabricate two- and three-dimensional microstructures for those applications, several fabrication techniques have been developed such as electrospinning [60], stereolithography [112] and ink direct-write technique [113].

Electrospinning has been actively exploited as a valuable and versatile method for generating long polymer fiber with a diameter ranging from tens of nanometers to several micrometers [114]. By allowing the process for some time, a porous scaffold is formed on the collector. To achieve a fibrous scaffold with oriented fibers, a rotating drum, disk, or parallel electrodes may be used [28]. PLA has been electro-spun into different forms of ultrafine fibers and used as carriers for bioactive agents [115]. PLA nanocomposite fibers containing nanofillers such as silver nanoparticles have also been successfully produced using the electrospinning technique [60].

Stereolithography is a solid freeform technique that was introduced in the late 1980s [112]. Commercially available stereolithography setups can build objects at an accuracy of $\sim$ 20 μm, and micro-sized structures with sub-micron resolution had been fabricated in laboratory [116]. Its working principle is based on spatially controlled solidification of a liquid photo-polymerisable resin. Using a computer-controlled laser beam or a digital light projector with a computer-driven building stage, a solid, 3D object can be constructed in a layer-by-layer fashion [117]. Poly-*DL*-lactide (DLLA) networks can be formed by photo-initiated radical polymerization of PLA oligomers end-functionalized with an unsaturated moiety such as a methacrylate-, acrylate-

or fumarate- groups. One of these PLA type has been developed and used to fabricate 3D porous scaffolds using stereolithography, which has excellent mechanical properties and very good biocompatibility with cells [117].

1.3.2 Direct-write technique

The direct-write technique is a method for precisely assembling periodic arrays. This technique employs a computer-controlled translation stage, which moves a pattern-generating device, that is an ink-deposition nozzle, to create materials with controlled architecture and composition [113]. As shown in Figure 1.6, the fugitive ink is contained in a syringe and is

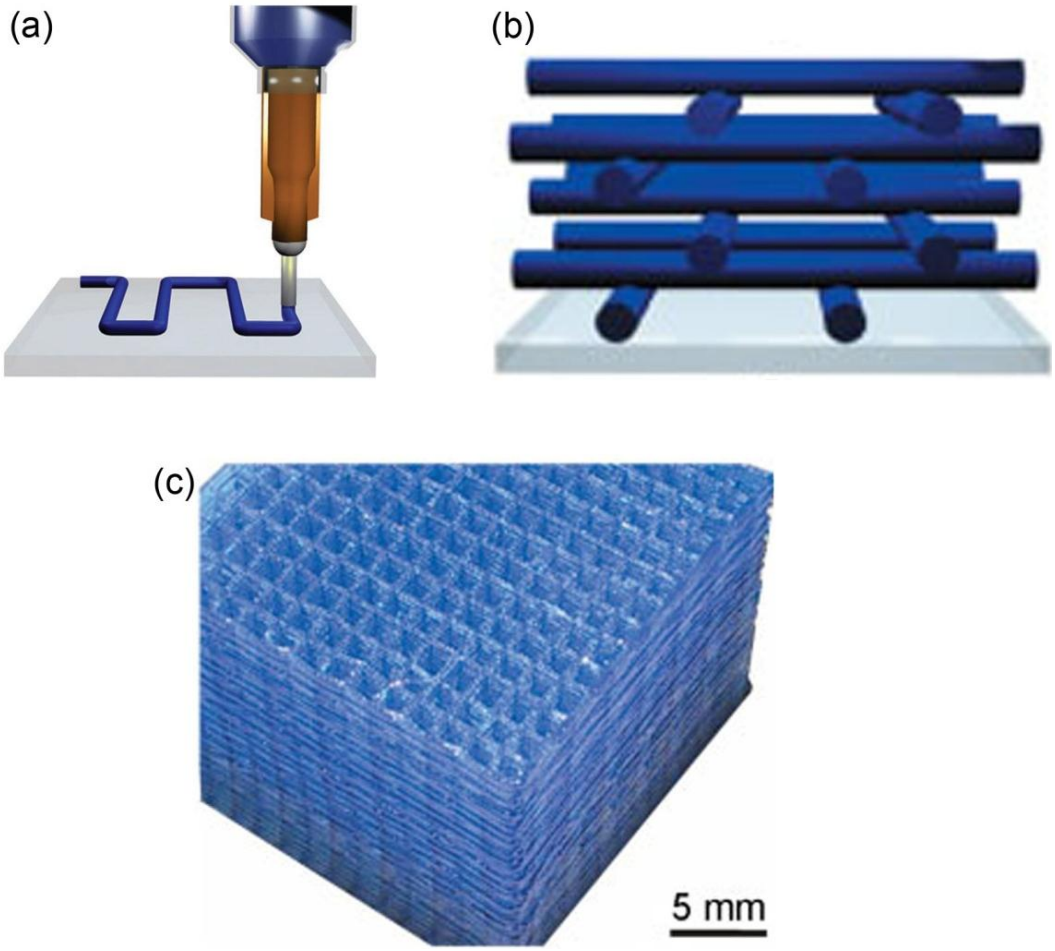

Figure 1.6 Schematic illustration of the fabrication of a 3D scaffold by the direct-write method: (a) deposition of fugitive ink; (b) ink layers after deposition; (c) optical image of a 104-layer scaffold assembled from the binary organic ink deposited through a 200 μm nozzle [10].

extruded through a micronozzle by applying pressure. In this example, a 3D scaffold consisting of a 104-layer structure of parallel cylindrical rods with an inter-rod separation distance of 1.25 mm has been fabricated, as shown in Figure 1.6c [10]. The technique can be applied to a wide range of materials that can be processed as inks, including concentrated colloidal [118], fugitive organic [119], and polyelectrolyte inks [120]. 3D periodic architectures with filamentary features ranging from hundreds of micrometers to sub-micrometer in size have been fabricated using these inks, and have various applications such as functional composites [118], microfluidic networks [119], and tissue engineering scaffolds [121].

Thermoplastic polymers can also be used as the ink to fabricate 3D structures when it is molten [19]. Bouchaar et al. designed an ink-fused direct-write system for thermoplastic

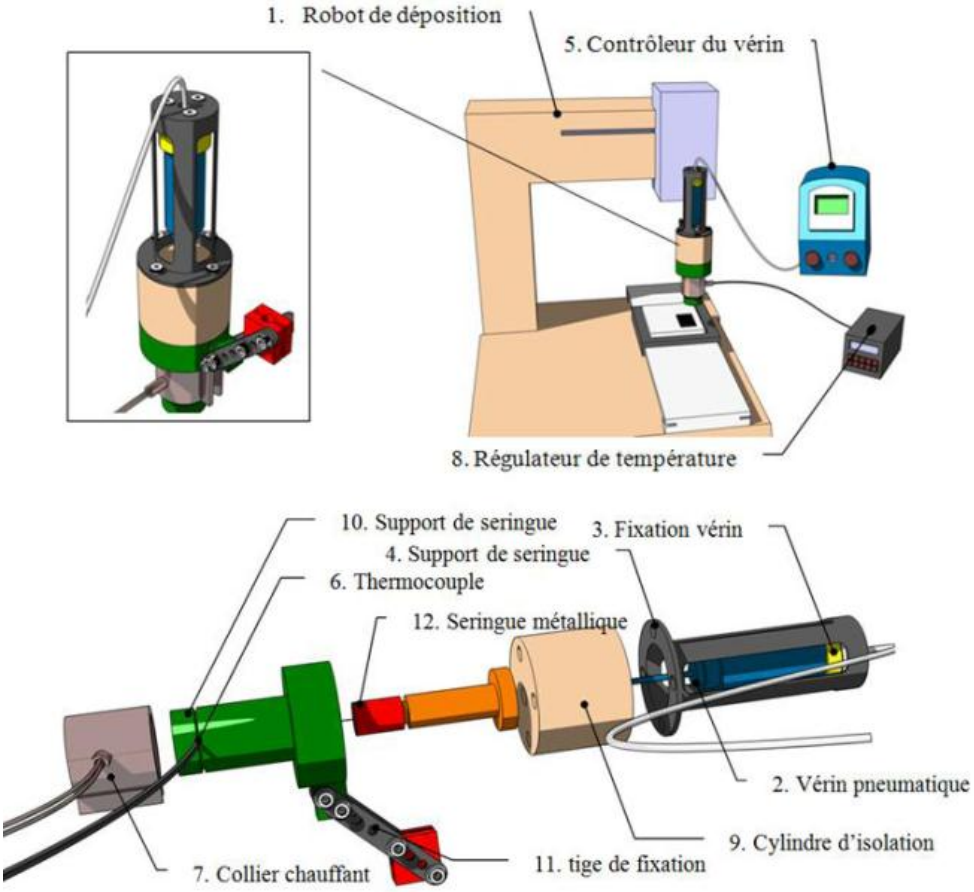

Figure 1.7 Schematic illustration of a direct-write assembly module for thermoplastic polymers [122].

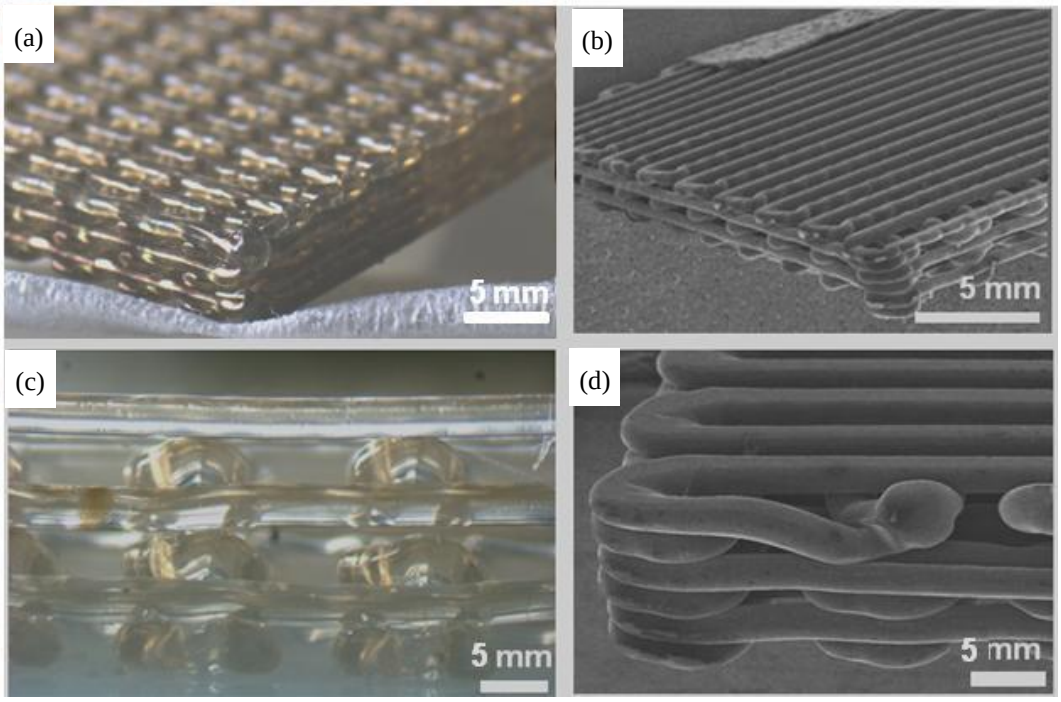

Figure 1.8 Perspective views of 3D scaffolds made by the ink-fused direct-write technique: (a) and (c) are optical microscopy images, (b) and (d) are SEM images [122].

materials as shown in Figure 1.7 [122]. During this approach, a PLA/nanoclay nanocomposite has been fed into the metallic syringe and fused at high temperature. Then the molten nanocomposite is deposited on the substrate and quickly become a solid filament at room temperature. The resolution of this system is limited by the high viscosity of the melt polymer. The diameter of the smallest filament fabricated with the PLA nanocomposite was 250 μm. The ink-fused direct-write system is a powerful technique to fabricate complex structures like microfilaments, microfilms, and micro-scaffolds from thermoplastic polymers (Figure 1.8). However, the high temperature may lead to thermal degradation of the polymer and affect the mechanical properties. In addition, the system presented in Figure 1.7 needs to be upgraded to a design with better sealing capacity, easier handling and cleaning.

1.4 CNT-based nanocomposites for sensing applications

There has been an explosion of interest in the development of a new species of intelligent materials termed “conductive polymer nanocomposites (CPCs)” [1-3], which can benefit

multifunctional properties such as high mechanical strength and stiffness, thermal and electrical conductivity at relatively low CNT loading. CPCs have been extensively used for various sensors based on the polymer reaction to environmental changes which affects the electrically conductive particle network [45, 92, 123]. External stimuli such as temperature shift [124], mechanical deformation [125], and the presence of gases and vapors [126] or solvents [127] can lead to measurable resistance changes of the CPCs.

As shown in Figure 1.9a-c, various designs of CPCs sensors containing CNT have been reported, including partially embedded CNTs in a polymer matrix [129], CNT arranged coating on polymer surfaces or fibers [130], and fully dispersed CNTs in a polymer matrix [127, 131, 132]. Due to its cost efficiency and tailored processing, the sensory CPCs with fully embedded CNTs are preferred. Various shapes and sizes (Figure 1.9d) were fabricated using different techniques. Thermosetting CPCs sensors are fabricated by either spin coating on substrates or slip casting [133], while thermoplastic based sensors are mostly processed using melt processing

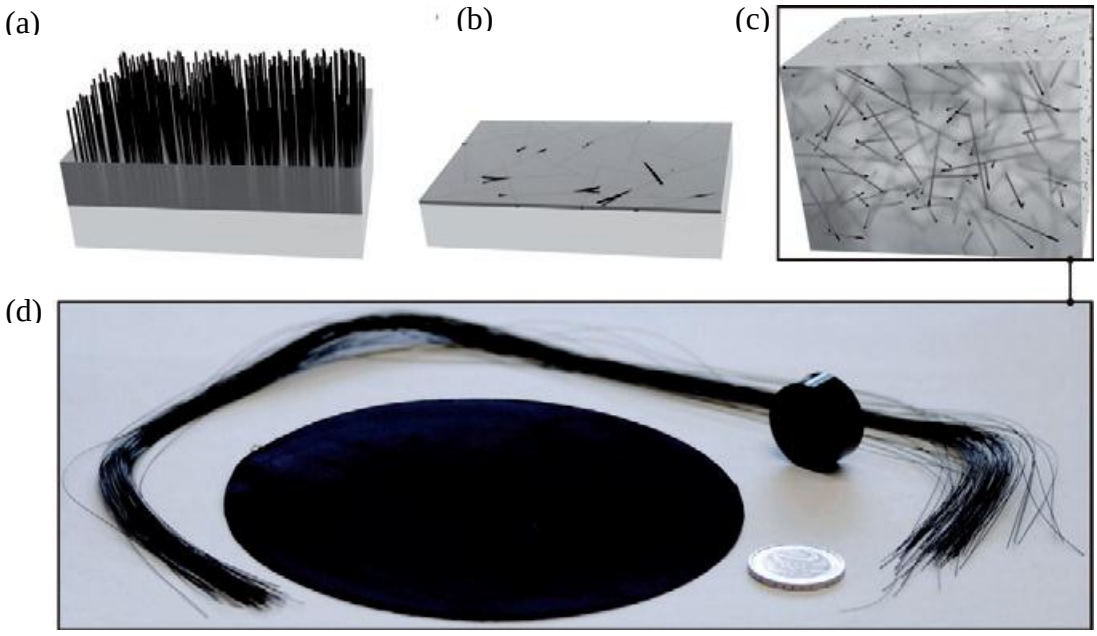

Figure 1.9 Different sensory CPC designs and CNT arrangements. (a) Partially embedded CNTs in polymer, (b) a polymer substrate covered with CNTs, and (c) full embedded CNTs in polymer. (d) Possible sensory CPC shapes (fibers, compression-molded plate, cylinder, and £2 coin for size comparison) [128].

technique, such as injection or compression molding [134, 135], and fiber spinning [136].

In the case of liquid sensing, the mechanism of CPCs is based on the ability of polymeric material to swell when being in contact with a solvent, which result in a disruption of contacts or increase in the distances between neighbored CNTs above the tunneling or hopping distances. Therefore, the resistivity of the CNTs network increases as the swelling proceeds [134]. Imaging the case of a dry CPC sensor immersed into a solvent, the swelling process will start at the surface and the resistivity will be inhomogeneous over the cross-sectional area. As shown in Figure 1.10, a partially swollen CPC sample consists of a swollen skin and an originally dry core [128]. The total sample conductivity is the result of contributions from both the core and skin regions. Hence, the resistance of the sensor is affected by its geometry, the penetration depth of the solvent, and the direction of the electric current.

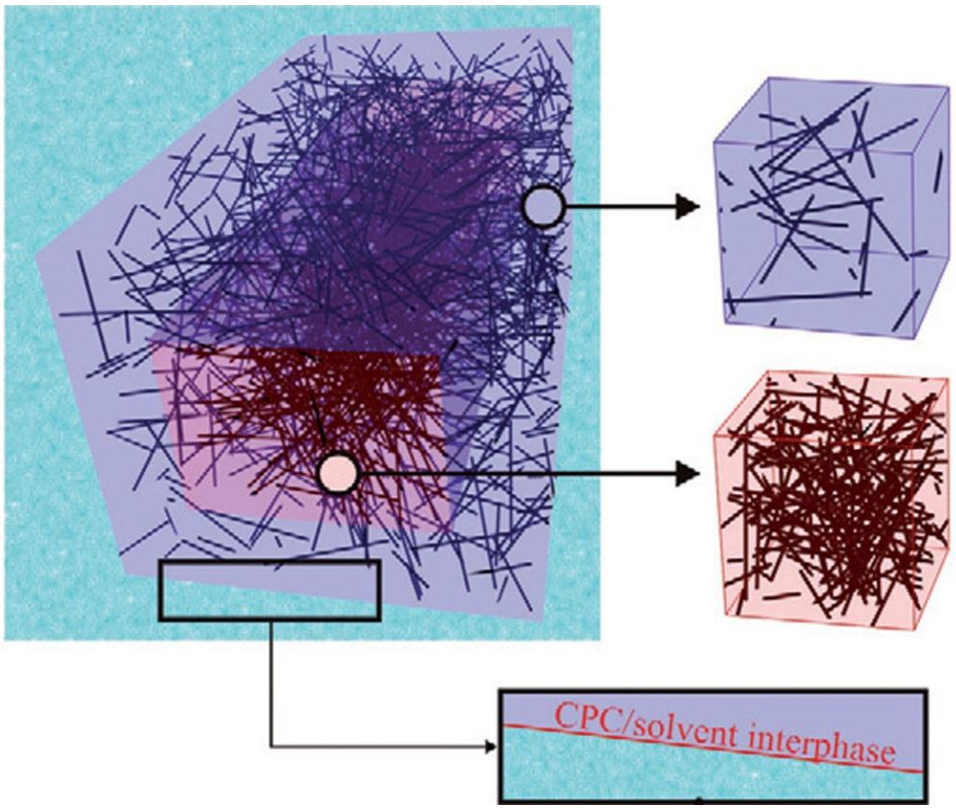

Figure 1.10 Development of the skin-core morphology of a liquid sensor contacting with “good” solvents, showing (blue) the swollen skin and (brown) the dry core, with altered and original composite properties, respectively [128].

The internal sensitivity of a sensor is defined as the ratio of the sensor output signal to a change in a property of the sensor, which can be thought as a slope defining the ability of the sensor to transduce an output signal [137]. Since the swelling is part of the dissolving process, the sensitivity of a CPCs sensor is determined by the solvent diffusion kinetic, which is influenced by the polymer and solvent solubility parameters, solvent molecule size and the temperature. Figure 1.11 represents the location of a specific polycarbonate (PC) and 59 different organic solvents in the corresponding Hansen space [132]. Generally, there is a solubility sphere with the partial solubility parameters of PC as the center point in this figure. Solvents located within this sphere will result in a polymer swelling and high sensory sensitivity. Solvents exceeding the sphere will predominantly not dissolve the matrix and will therefore not result in relative resistance change of CPCs. Furthermore, when CPCs contact with good solvents located within the sphere, smaller molecule sizes of the solvents will lead to faster diffusion kinetics [132]. Moreover, the radius of

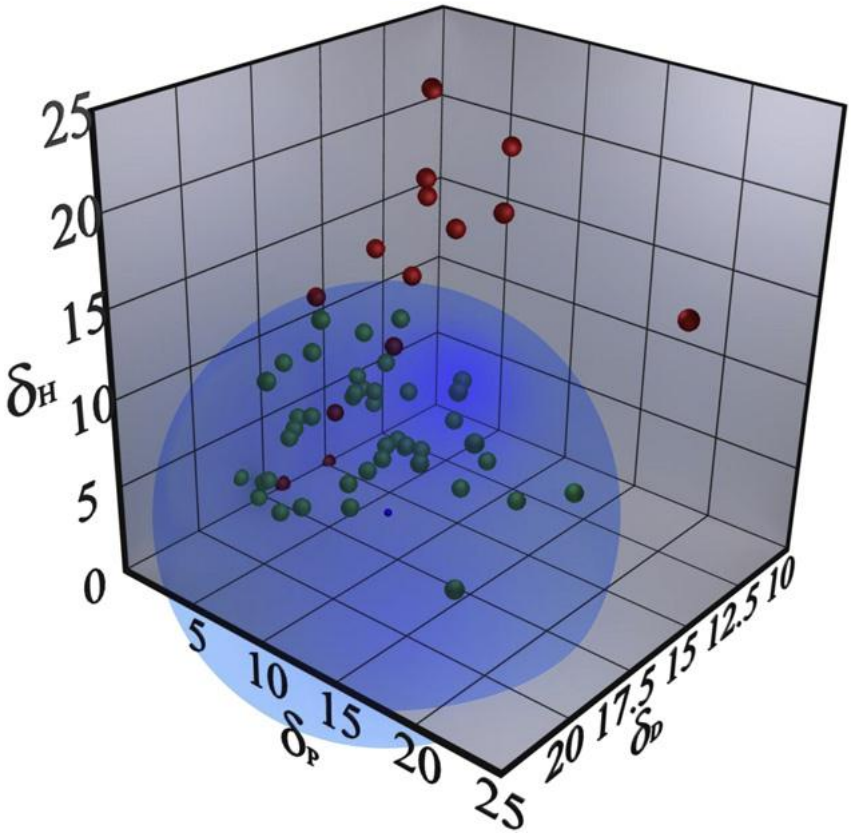

Figure 1.11 The CPC's solubility sphere with 44 "good" solvents (green dots), 15 "bad" solvents (red dots) and the sphere's center point representing the CPC (small blue dot) [132].

the solubility sphere may increase with increasing the temperature [132].

Besides being able to produce an output signal indicative of the presence of analyte, a sensor must also be able to distinguish between the analyte and any other materials, which is called selectivity [137]. Here, different sensor sensitivities for various solvents mean the selectivity of a liquid sensor. Figure 1.12 presents a solvent map of the solvent selectivity of a CPC based on PC and 1.5 wt% CNTs [132]. Green data points represent solvents that lead to significant and fast resistance increases of the CPC. On the other hand, the solvents marked with red dots do not lead to relative resistance changes of the CPCs. This solvent mapping allows the definition of the selectivity of the specific CPC by distinguishing the solvents into good or bad.

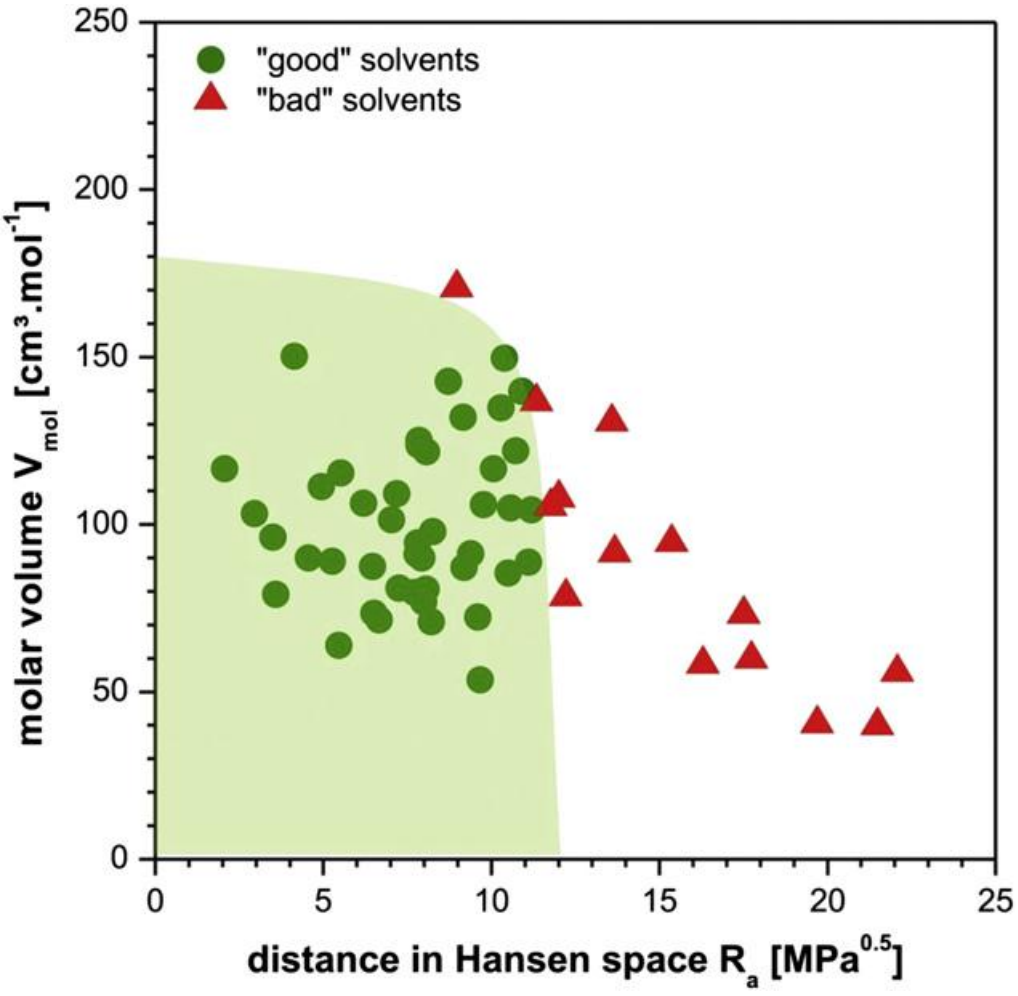

Figure 1.12 Selectivity of the CPC enabling the mapping of “good” and “bad” solvents depending on their molar volume and distance in Hansen solubility space [132].

1.5 Summary of literature review

As reviewed, polylactide (PLA) is a degradable thermoplastic polymer derived from renewable sources, and promising to replace petroleum-based plastics in commodity applications. However, in the case of multifunctional systems, PLA suffers from some shortcomings such as low thermal stability, poor electrical conductivity (as most thermoplastics) and weak mechanical properties at moderate temperatures due to its low T_g. Therefore, adding electrically conductive nanofillers represents an interesting way to extend and improve the properties of PLA.

However, there is no considerable research on the electrical conductivity of PLA nanocomposites. To optimize PLA nanocomposites, the nanofiller should be well dispersed in the matrix using various approaches including melt mixing and solution-based processes. Meanwhile, the aspect ratio of the nanofillers should be maintained as high as possible during the process. Moreover, the correlation between processing parameters and the nanocomposite properties should be thoroughly investigated.

The microfabrication techniques of thermoplastic polymers such as electrospinning, and stereolithography have been confined to 2D and limited 3D geometries with tedious process and limited materials. As a 3D printing technique, the direct-write assembly is an attractive method for creating complex 3D microdevices. Thermoplastic polymers have been developed as 3D printing inks using the molten deposition method. However, the high viscosity, melting temperature and thermal degradation of the polymer during the process limit its applications.

Multifunctional CPCs have been extensively used for various sensors based on the polymer reaction to environmental changes which affects the electrically conductive particle network. Thermoplastic based liquid sensors are mostly processed using melt processing techniques, and the shapes of the sensors are limited to fibers, compression-molded plates and cylinders.

CHAPTER 2: Research Objectives and Coherence of Articles

2.1 Research objectives

According to the literature review presented in Chapter 1, 3D nanocomposite structures are highly promising for their utilization in MEMS applications. However, current fabrication techniques feature important limitation for the manufacturing complex 3D geometries, especially with materials featuring multifunctional properties. Thus, the principal aim of this work:

"is to develop a novel microfabrication technique to manufacture 3D multifunctional microsystems using thermoplastic polymers and their nanocomposites"

The specific objectives of the current work are:

1) To develop a versatile and flexible method to fabricate 3D freeform microstructures inspired by the direct-write assembly of polylactide.
2) To establish a comprehensive understanding of the proposed method and investigate the effects of process-related parameters (i.e., applied pressure, nozzle diameter, robot velocity) and material-related parameters (i.e., polymer concentration, nanofiller content, rheological properties, solvent evaporation) on the processability and properties of the fabricated structures.
3) To prepare a PLA/electrically conductive nanocomposite using a combination of melt mixing and solution processes, that is compatible with the fabrication method.
4) To demonstrate the feasibility of 3D multifunctional microstructures used in micro electromechanical systems (MEMS) with the creation and testing of a liquid sensor.

2.2 Presentation of articles and coherence with research objectives

Chapters 3, 4 and 5 present the main scientific findings of this work and represent the core of the thesis, which is presented in the form of three peer-reviewed journal papers, which cover the objective of developing a novel microfabrication technique to manufacture 3D multifunctional microsystems using thermoplastic polymers and their nanocomposites as detailed in the following section.

Chapter 3 presents the results of the first paper "*Solvent-cast three-dimensional printing of multifunctional microsystems*" that has been published in *Small* (Vol. 9, 2013, 4118-4122) (impact factor = 7.823). This journal was chosen because it is among the top multidisciplinary journals covering a broad spectrum of topics at the nano- and microscale experimental and theoretical studies. This paper was submitted on March 27, 2013 and published on December 12, 2013. In this work, a solvent-cast 3D printing technique using PLA solutions as inks was developed to fabricate various microstructures including straight filaments, layer-by-layer scaffolds and freeform helical spirals (specific objective 1). The extruded filament rapidly underwent fluid-like to solid-like transition due to fast solvent evaporation, which allowed maintaining their filamentary shape and buildup of complex structures. The fabrication capabilities of this powerful and flexible process were demonstrated by the printing of three microsystems featuring mechanical, microfluidic and electrical functionalities such as high-toughness microstructured fiber, 3D microfluidic channel and Ka band micro antenna.

Chapter 4 presents the second article "*Properties of polylactide inks for solvent-cast printing of three-dimensional freeform microstructures*" that has been accepted and published online in *Langmuir* (DOI: 10.1021/la4036425, 2014) (impact factor = 4.187). This journal was chosen because it constitutes an important platform for publications on polymer physics and chemistry. This paper was submitted on September 24, 2013 and published online on January 10, 2014. In this work, a comprehensive characterization of the solvent-cast printing process using PLA solutions was performed by analyzing the flow behavior of the solutions, the solvent evaporation kinetics and the effect of process-related parameters on the crystallization of the extruded filaments (specific objective 2). A processing map was given to show the proper ranges of process-related parameters for the fabrication of different geometries. This work offered a new perspective for manufacturing complex structures from polymer solutions and provided guidelines to optimize the various parameters for 3D geometry fabrication. This knowledge was critical for the successful design of nanocomposite inks and their 3D printing.

Chapter 5 contains the third paper "*3D Printing of Multifunctional Nanocomposite Helical Liquid Sensor*" that has been submitted to *Advanced Materials* (impact factor = 14.829) on May 12, 2014. This journal was chosen because it is one of the most prestigious platforms for publications on the latest progress in materials science with interdisciplinary scopes. In this paper, a masterbatch of PLA/MWCNT nanocomposite was prepared by melt mixing using a micro

twin-screw extruder. Different geometries were subsequently fabricated by the solvent-cast 3D printing method using PLA-based nanocomposite solutions as inks (specific objective 3). The effects of the MWCNT loading on the process-related apparent viscosity of the inks and the electrical conductivity of the fabricated structures were reported. Two nanocomposite structures including a straight line and a 3D helix were investigated as liquid sensors (specific objective 4). The 3D helical sensor not only possessed relative high electrical conductivity, but also a structure capability of liquid trapping, which prompted itself with excellent sensitivity and selectivity even for a short immersion in the solvents. The present manufacturing method offers new prospective to fabricate freeform microstructured MEMS sensors with a 3D designed pattern.

CHAPTER 3: Article 1: Solvent-Cast Three-Dimensional Printing of Multifunctional Microsystems

Shuangzhuang Guo, Frédérick Gosselin, Nicolas Guerin, Anne-Marie Lanouette, Marie-Claude Heuzey and Daniel Therriault, published in *Small*, Vol. 9, December 12, 2013, 4118-4122.

3.1 Abstract

Three-dimensional structures fabricated from polymers and their nanocomposites may find widespread technological applications as sensors, microvascular networks, self-healing materials, and tissue engineering scaffolds. Here we present the development of the solvent-cast direct-write fabrication method used to fabricate 3D geometries at room temperature in a freeform fashion with dissolvable thermoplastic polymers. The thermoplastic ink solution and process parameters such as polymer concentration and solution viscosity, solvent evaporation rate and nozzle diameter are discussed. We believe that this process and its compatibility with thermoplastic-based nanocomposites materials will create new prospects for the micromanufacturing of complex 3D functional structures.

3.2 Main text

Three-dimensional (3-D) structures fabricated from polymers and their nanocomposites may find widespread technological applications as sensors,[1-3] microvascular networks,[4, 5] self-healing materials,[6-9] and tissue engineering scaffolds.[10-12] Theses applications either require, or could benefit from, the ability to pattern micro-sized features in complex 3-D architectures. Several strategies and technologies have recently emerged to rapidly and cost-effectively fabricate thermoplastic polymer-based 3-D microdevices. For example, fused deposition modeling (FDM) stands out as the most popular procedure to manufacture 3-D products with a spatial resolution down to 45 μm.[13] However, the thermal degradation caused by high processing temperatures and the high viscosity of most polymer melts may prevent the application of this technique to be compatible with nanocomposite devices, since nanoparticles can significantly increase material viscosity. Also, electrospinning has been used to produce fiber-based polymer structures with fiber diameters ranging from ~100 nm to ~300 μm[14-16]

but is limited in terms of 3-D structure complexity.[14]

Direct-write (DW) assembly is a 3-D printing technique that employs a computer-controlled translation stage, which moves an ink-deposition nozzle, to create materials with controlled architecture and composition.[17] This technique requires specific ink rheological and viscoelastic properties. First, the ink viscosity should be low to moderate to facilitate its extrusion through a capillary micronozzle under applied pressure. Second, the rigidity of the filament after extrusion must quickly increase for shape retention. Many ink materials have been employed such as organic fugitive ink,[18] concentrated polyelectrolyte complexes,[19] colloidal suspensions,[20-22] hydrogels[23, 24] and thermoset polymers.[25] These inks solidify through different mechanisms such as viscoelastic recoil,[18] coagulation in reservoir,[19] suppression of repulsive forces,[20] and UV polymerization.[23-25] Thermoplastic polymers have also been used in the direct write technique (fused deposition) due to their rigidity increase after the temperature-triggered phase transition from melt to solid,[13] however this method exhibited limited control of the 3-D printed feature geometries.

The solvent-cast direct-write (SC-DW) fabrication method presented in this study was developed to fabricate 3-D geometries at room temperature in a freeform fashion with dissolvable thermoplastic polymers (see Figure 3.1). The method consists of the robotically controlled micro-extrusion of a concentrated polymer solution ink filament, combined with rapid solvent evaporation after the filament exits the micronozzle. Under applied pressure, the polymer

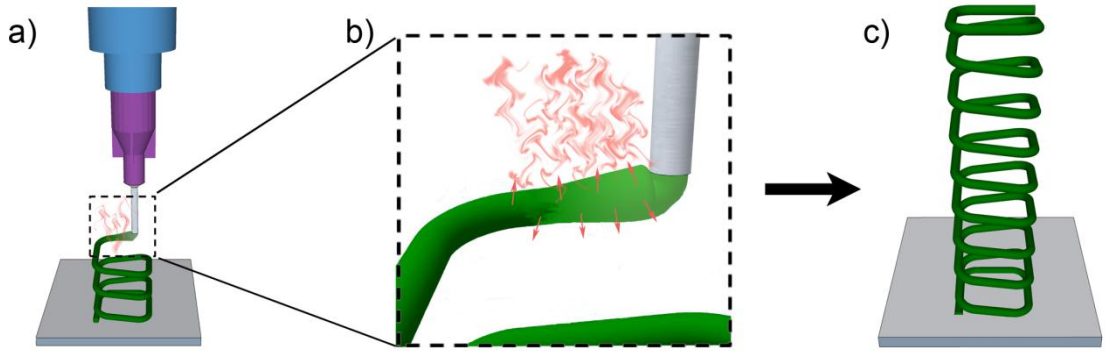

Figure 3.1 Schematic representation of the SC-DW process with a thermoplastic solution. a) Deposition of the polymer solution through a micronozzle. b) Rapid solvent evaporation post extrusion. c) Example of a 3-D square spiral fabricated by the SC-DW assembly.

solution, which undergoes capillary shear flow inside the micronozzle, relaxes its stresses upon exiting the nozzle. As the solvent evaporates post extrusion, the diameter of the filament decreases and its rigidity gradually increases with time due to a locally higher polymer concentration. This rigidity gradient enables the creation of self-supporting curved shape by changing the moving path of the extrusion nozzle, in which the filament bending occurs in the low rigidity zone of the newly extruded material. After most of the solvent evaporation, the rigidity of the extruded filament changes from fluid-like to solid-like, which facilitates the shape retention of the deposited self-supporting features. This 3-D printing process enables the creation of different multifunctional microsystems featuring complex geometries.

For successful solvent-cast direct writing of 3-D freeform structures, the selected solvent and the polymer concentration in the solution have to be set to ensure proper ink rheological behavior while providing a fast solvent evaporation. Then, the velocity of the extrusion nozzle and the applied pressure on the polymer solution must be tailored to achieve the desired material linear flow rate. In this initial demonstration, the thermoplastic used was polylactide (PLA), a polymer derived from renewable resources, and the solvent was dichloromethane (DCM, boiling point = 39.6 ℃) due to of its fast evaporation and good PLA dissolvability.

The viscoelastic properties of the polymer solution, which were tailored by varying the polymer concentration, determined its flowing behavior inside the nozzle and the initial rigidity of the extruded filament. A polymer solution with high viscosity required a high applied pressure during the extrusion step. On the other hand, a lower viscosity solution flowed from the nozzle more easily; however the resulting filament needed more time to dry since it contained more solvent. Because of the solubility limitation of PLA in DCM at room temperature, the maximum PLA concentration studied in this project was 30 wt%; solutions of 20 and 25 wt% PLA were also investigated. The process-related apparent viscosity of the three PLA solutions was determined by capillary flow analysis in the nozzle, and the results are presented in Figure 3.2a. For all of the PLA solutions, a rheological shear-thinning behavior was observed, since the process-related apparent viscosity decreased with increasing process-related apparent shear rate. This property enhances the material processability during extrusion through the capillary nozzle under high shear rates due to a decrease in viscosity. Figure 3.2a also shows that the process-related apparent viscosity increased significantly with polymer content. The 30 wt% PLA solution was successfully used to fabricate 3-D freeform structures because of its relatively high

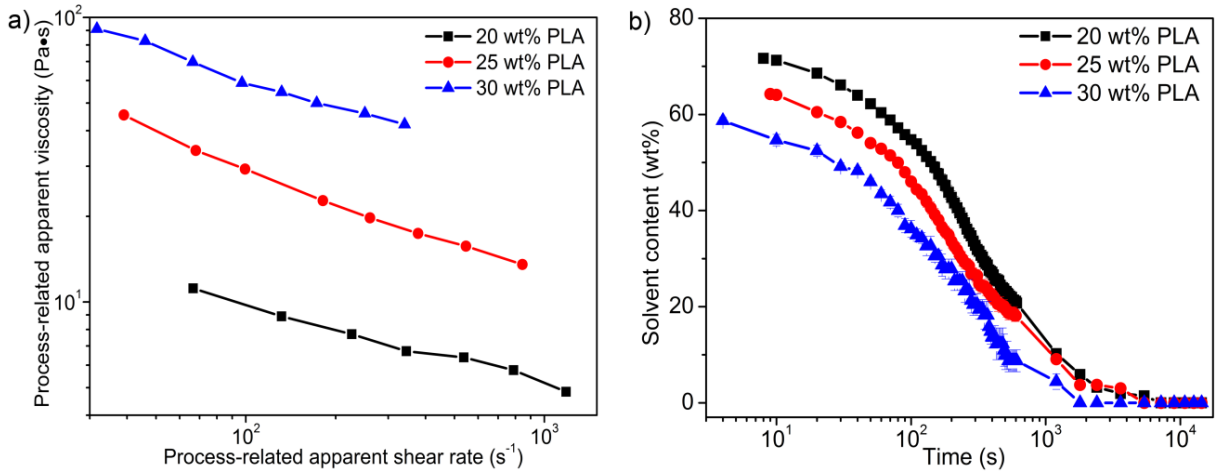

Figure 3.2 SC-DW ink characterization. a) Process-related apparent viscosity. b) Solvent content as a function of time for different polymer concentrations.

viscosity, while the 25 wt% PLA solution was more suitable for 2D conformal printing. As for the 20 wt% PLA solution, it was difficult to form continuous smooth filaments for all the nozzles used (inner diameter ranging from 510 to 100 μm).

After filament extrusion of self-supporting features, the solvent evaporation plays a crucial role in the geometric retention. Upon rapid evaporation, the rigidity of the material significantly increases and provides the required structural support for the deposition in a continuous manner and along different directions, therefore allowing freeform writing in open air. The solvent evaporation rate was investigated by monitoring the weight reduction of the deposited filament as a function of time using a high-precision balance. Figure 3.2b shows the solvent content evolution with time of a short filament (length of ~5 mm) deposited using a 510 μm inner diameter nozzle. The initial solvent fraction measured by our gravimetric method was smaller than the nominal content in the polymer solution. This lower value was attributed to the flash evaporation caused by rapid pressure reduction that occurred near the extrusion point.[26] Our results reveal that approximately 50% of the solvent evaporated within the first 3 minutes of the gravimetry test, and the filament deposited from the 30 wt% PLA solution exhibited the shortest drying period. Actually the utilization of a nozzle with an inner diameter of 100 μm was required to build 3-D freeform structures using the 30 wt% PLA solution. The solvent present inside a

smaller diameter filament takes less time to diffuse to its surface and the rigidity of the filament increases more quickly, which is of great benefit to the 3-D geometric retention. During our process mapping, we observed poor 3-D freeform geometric retention when using the 30 wt% PLA solution and larger nozzles (≥ 200 μm), or using lower PLA content solutions (25 or 20 wt%) for all nozzles investigated.

Different kinds of 3-D microstructures were fabricated by the SC-DW assembly including a square spiral, circular spiral, micro-cup and 9-layer scaffold showed in Figure 3.3b-f. This flexible method enables the fabrication of unique structures that are generally difficult to produce by conventional single-stage processing methods, including floating (Figure 3.3b and c),

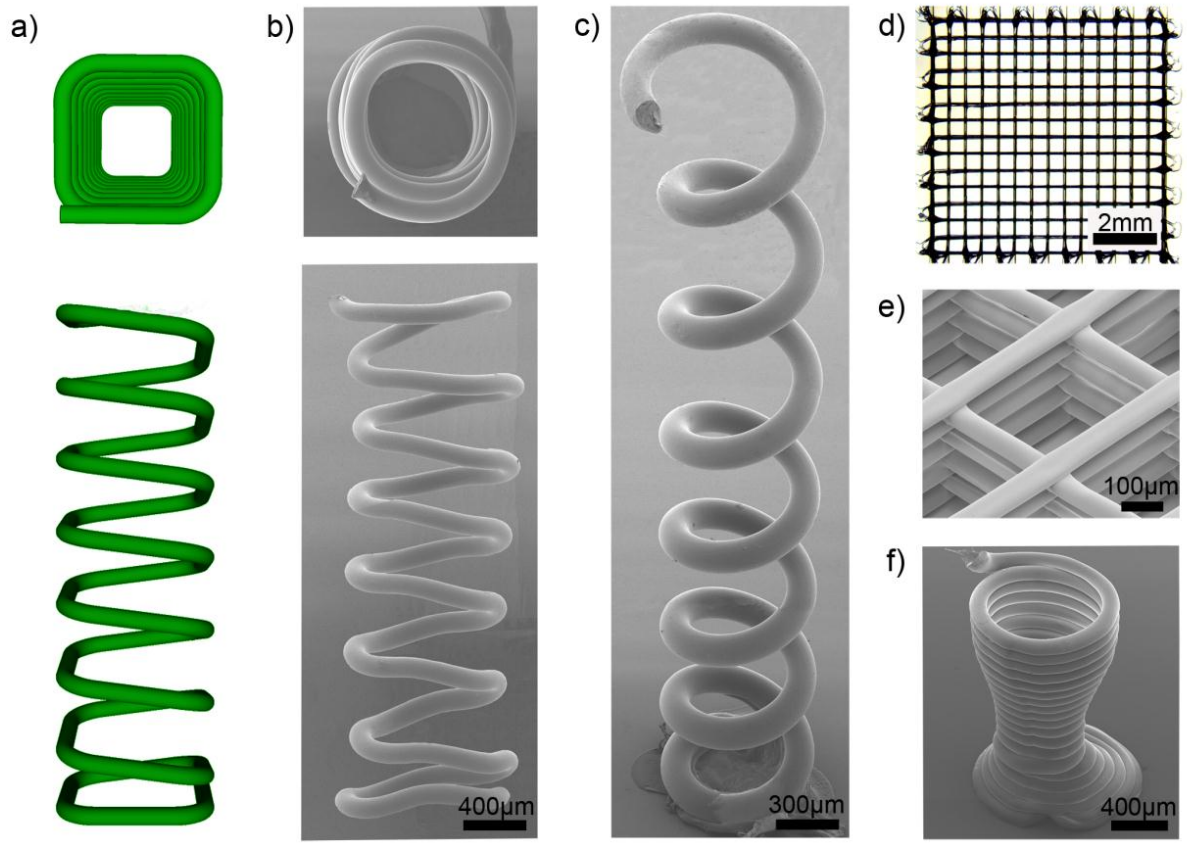

Figure 3.3 Microstructures manufactured by SC-DW. (a) Top and side view virtual images of the programmed SC-DW fabrication of the square spiral. (b) Top and side view SEM images of an actual PLA square spiral. (c) Inclined top view SEM image of a PLA circular spiral. (d) Representative optical image of a PLA scaffold composed of nine layers. (e) Inclined top view SEM image of PLA 9-layer scaffold. (f) SEM image of a PLA cup.

spanning (Figure 3.3d and e) and scalable (Figure 3.3f) structures. Figure 3.3a shows top and isometric side views from a computer-aided design (CAD) image of the programmed deposition path of the SC-DW apparatus to manufacture a square spiral using eight 1.0 mm side length loops and a pitch of 0.7 mm. Figure 3.3b shows scanning electron microscopy (SEM) top and side view images of the actual square spiral deposited. The average side length of the actual square spiral was 1102 $\pm$ 15 μm and the average pitch was 707 $\pm$ 22 μm. For the circular spiral of Figure 3.3c, the average spring diameter was 966 $\pm$ 6 μm and the average pitch was 530 $\pm$ 25 μm. Both values were very close to the programmed deposition path (*i.e.*, spring diameter of 1.0 mm, pitch of 500 μm). The layer-by-layer scaffold (Figure 3.3d, e) and the micro-cup (Figure 3.3f) were almost identical to their respective programmed deposition paths because the printing layer was supported by the underlying layer. Consequently, the SC-DW method was demonstrated to be a flexible and high fidelity micromanufacturing process. The main limitation remains the freeform deposition of sharp turns which lead to some geometric discrepancies. For example, the measured average radius of the square spiral turn was 345 $\pm$ 7 μm, which was almost twice the programmed value (167 μm).

Three different microsystems were fabricated in order to demonstrate the fabrication capabilities of SC-DW. First, a high-toughness microstructured fiber was developed by harnessing a flow instability during the fabrication process. This application was inspired by the molecular structure of spider silk proteins.[27] The sacrificial bonds in the microstructured fiber play an analogous role to that of the hydrogen bonds present in the molecular structure of the silk protein which give its toughness to spider silk.[27] Figure 3.4a shows a regular straight fiber and its neatly circular cross-section. Figure 3.4b displays a microstructured fiber fabricated by extruding the polymer solution towards a substrate moving perpendicularly at a slower velocity than the filament linear flow rate (see Supporting Information, Figure 3.5). The filament repetitively buckled giving rise to periodic meanders and stitch patterns. Uniaxial tension tests performed on the fibers reveals that the microstructured fiber exhibited a much higher breaking strain (straight fiber 116% vs. microstructured fiber 766%, Figure 3.4d) due to the sacrificial bonds created when the viscous filament looped over itself and fuse. In order to stretch the fiber under uniaxial tension, the sacrificial bonds must be broken (see the stretched microstructured fiber in Figure 3.4c), hence adding to the total energy required for breaking the fiber.

Second, the SC-DW approach can also be used to fabricate complex microfluidic devices by using the printed thermoplastic features as a sacrificial material. As an example, we developed a 3-D microchannel that can be used for fluidic mixing[4] or particle separation.[28] Figure 3.4e

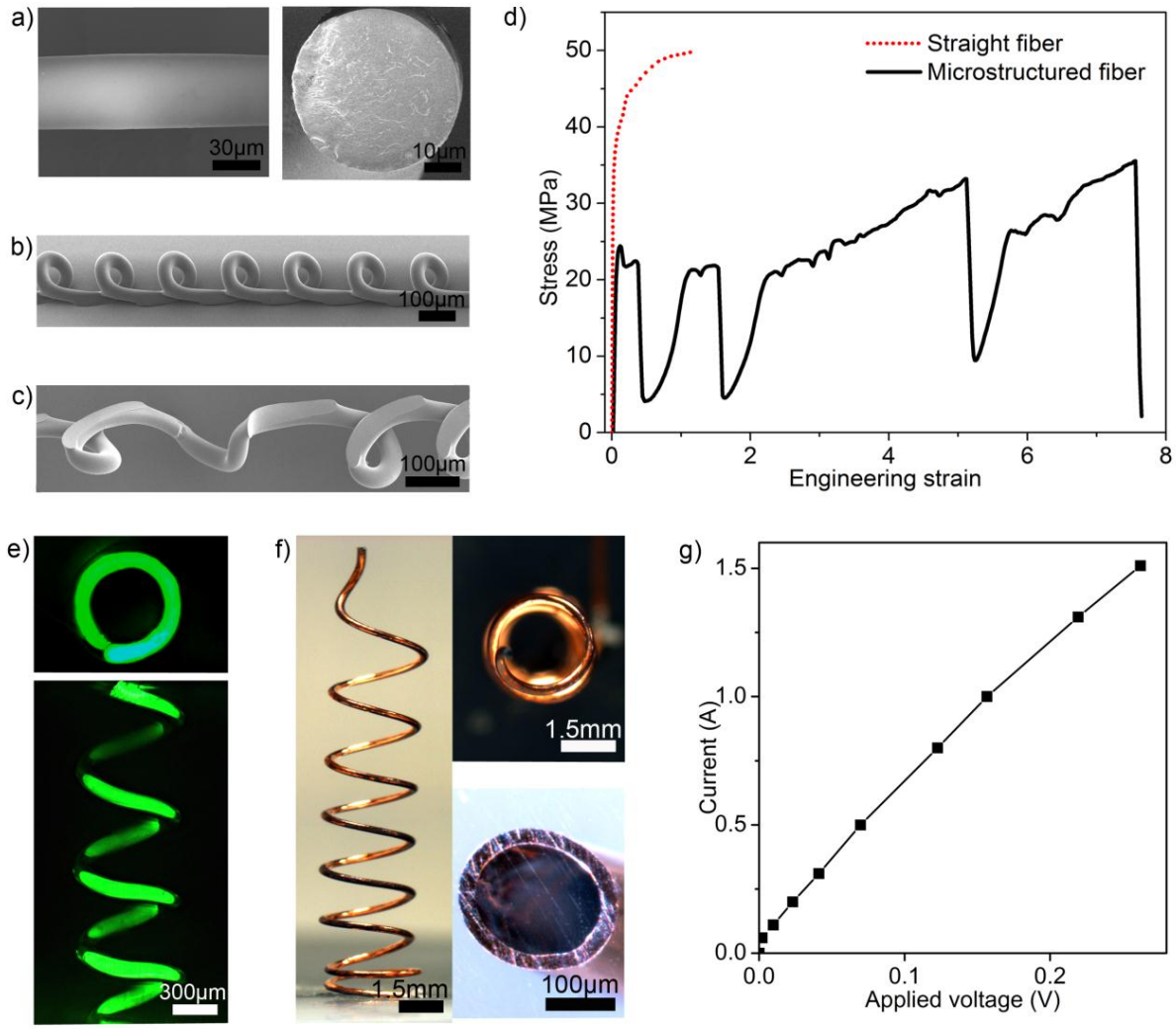

Figure 3.4 Representative SEM images of a) straight PLA fiber and its circular cross section, b) microstructured PLA fiber with sacrificial bonds, and c) stretched microstructured fiber. d) Tensile properties comparison for a straight fiber (dash line) and a microstructured fiber (solid line). e) Fluorescent microscopy top and side view images of a fluid-filled spiral microchannel embedded inside an epoxy matrix. f) Optical side, top and cross-sectional view images of the copper coated 3-D variable pitch spiral antenna. g) Measured current upon voltage application between two ends of the 3-D spiral antenna.

shows fluorescent microscope top and side view images of the fluid-filled microchannel. This microfluidic channel was achieved by first depositing by SC-DW technique a freeform PLA spiral containing a catalyst.[29] After its encapsulation in epoxy and complete curing, the sample was heated in a vacuum oven in order to depolymerize the PLA and create a smooth microfluidic channel (see Supporting Information, Figure 3.6). Further optimization of the channel size and topological structures is ongoing for its incorporation into a highly efficient micro-particles separator.

Finally, the SC-DW method also offers a new possibility to build electrically conductive structures such as high frequency devices. For instance, a small spiral Ka band antenna (20-30 GHz) was fabricated by depositing a PLA spiral featuring variable pitch distances followed by the sputtering of a $\sim$50 μm copper layer coating. Figure 3.4f shows optical microscopy images of the metallic coated and PLA core small antenna. The measured current with respect to the applied voltage curve showed a nearly linear response within the voltage range investigated, and the calculated electrical resistance of the antenna was $\sim$0.174 Ω (Figure 3.4g). More work is ongoing to characterize the spiral antenna and improve its telecommunication performance.

In summary, the SC-DW technique developed in this work offers a low-cost, highly flexible and powerful fabrication route for microsystems featuring mechanical, microfluidic and/or electrical functionalities. This technique represents an important step toward sustainable development for the microfabrication community due to its compatibility with recyclable and biodegradable materials (*e.g.*, PLA) and the very small production of waste materials even during the creation of complex 3-D freeform shapes. The extension of the fabrication capabilities of the technique could be achieved through the utilization of other inks (*e.g.*, bio-based and synthetic thermoplastics, electrically-conductive and mechanically-adaptive nanocomposites) and the printing of features at the submicron and potentially nanoscale. On a longer term, we envision that the SC-DW approach could be used in medicine (*e.g.*, printing of biocompatible and/or biodegradable 3-D micro-prosthetics, tissue engineering scaffolds or cylindrical mesh for stents), in microelectronics (*e.g.*, inductance components, flexible electrical connections) and in structural composites (*e.g.*, microstructured fibers).

3.3 Experimental section

Ink preparation: Neat polylactide (PLA 4032D, Natureworks LLC) was dissolved in dichloromethane (DCM, Sigma-Aldrich) to prepare polymer solutions with different PLA concentrations (20, 25 and 30 wt%). After resting for 12 h, the solutions were stirred and sonicated in an ultrasonic bath (Ultrasonic cleaner 8891, Cole-Parmer) for 1 h. The solutions were stored in sealed bottles until processing.

Capillary flow analysis: The process apparent viscosities of the three PLA solutions (20, 25 and 30 wt% PLA) were calculated from constant-pressure capillary flow data as described by Bruneaux *et al*.[30] The polymer solution was extruded through a micronozzle with an inner diameter of 200 μm (5127-0.25-B, EFD). After reaching the extrusion steady state, lines of ink were deposited onto a substrate for 60 s under eight applied pressures ranging from 0.2 to 3.5 MPa at a robot velocity of 1 mm s^{-1}. The extruded fibers were dried in an oven (G05053-10, Cole-Parmer Instrument Company) at 50 ℃ for 12 h and then weighed using a high-precision balance (GH-202, A&D Engineering Inc.). The mass of the fibers served to determine the mass flow rate, which was converted to the volumetric flow rate using the respective fluid density. The capillary data reported in this work include the Rabinowitch correction. The Bagley correction for end effects was neglected because the ratio of the extrusion nozzle length to its diameter was larger than 50.

Determination of solvent evaporation rate: The solvent evaporation behavior of the polymer ink was evaluated by directly depositing a filament on a glass substrate resting on a high-precision balance. The computer controlled robot (I&J2200-4, I&J Fisnar) was used to deposit the polymer solutions on the substrate for 5 seconds through a nozzle with 510 μm (5121-0.25-B, EFD) inner diameter, under an applied pressure of 420 kPa. The sample weight change was recorded for 6 h. Following this recording period, the sample was completely dried in an oven at 50 ℃ for 12 h and weighted again. The mass of the dried PLA was then used to calculate the solvent percentage in the deposited filament.

SC-DW assembly of 3-D structures: The deposition system consisted of a computer controlled robot (I&J2200-4, I&J Fisnar) moving a dispensing apparatus (HP-7X, EFD) along the *x*, *y* and *z* directions. The square spiral, circular spiral and micro-cup were fabricated with the 30 wt% PLA solution using a micronozzle with a 100 μm inner diameter (5132-0.25-B, EFD) under

an applied pressure of 1.75 MPa and 0.1 mm s^{-1} robot velocity. The pitch of the square spiral was 0.7 mm and the side length of the coil was 1.0 mm. The pitch of the circular spiral was 0.5 mm and the radius of the coil was 0.5 mm. The 9-layer scaffold was fabricated with the 25 wt% PLA solution using the 100 μm inner diameter nozzle under an applied pressure of 1.4 MPa and 1.0 mm s^{-1} robot velocity. The filament diameter in the scaffold was about 80 μm and the inter-distance between two adjacent filaments was 500 μm.

Fabrication and characterization of high-toughness fiber: The microstructured fiber was fabricated by extruding the 26 wt% PLA solution through a 30 μm inner diameter nozzle under an applied pressure of 0.7 MPa and 2.0 mm s^{-1} robot velocity. The tensile tests were performed using a dynamic mechanical analyzer (DMA Q800, TA Instruments). The load was increased at a rate of 0.5 N min^{-1} until the fiber was broken.

Fabrication of spiral microchannel: The channel was fabricated by first depositing the 30 wt% PLA solution with catalyst Tin(II) Oxalate (1.5 wt%, Sigma-Aldrich) into a circular spiral on a glass substrate. The deposited pattern was then encapsulated by pouring uncured epoxy (Epon 862/ Epikure 3274, Momentive) followed by its complete curing. The cured epoxy block was released from the glass substrate and cut in order to open the two ends of the microchannel. The sample was then heated in a vacuum oven at a temperature of 200 ℃ and an absolute pressure of 2.5 mm Hg for 48 h. This heat and pressure cycle depolymerized the PLA and left an empty microchannel in the epoxy.

Fabrication and characterization of antenna: A freeform circular spiral was created using a ～30 wt% PLA solution extruded through a 200 μm micronozzle diameter and a robot velocity of 0.1 mm s^{-1}. The 3-D antenna was completed by sputtering the PLA spiral with a ～50 μm copper layer coating using an electrolytic bath. The designed antenna featured eight coils for a total height of 23.2 mm and an internal diameter of 3.4 mm. The electrical conductivity of the antenna was measured with a laboratory DC power supply (GPS-3303, Instek) and a shielded I/O connector block (SCB-68, NI).

Morphological characterization: The microstructures were sputtered with gold for 15 s and observed on a Scanning Electron Microscope (SEM) (JSM-7600F, JEOL. Ltd.). The optical and fluorescent images were acquired with an optical microscope (BX-61, Olympus) and analyzed with image processing software (Image-Pro Plus 6.0, Media Cybernetics).

Supporting Information is available on the WWW under http://www.small-journal.com or from the author.

Acknowledgements

The authors acknowledge the financial support from NSERC (Natural Sciences and Engineering Research Council of Canada). A scholarship for Mr. Guo was also provided by the China Scholarship Council (CSC).

Received: March 27, 2013
Revised: April 14, 2013
Published online: July 12, 2013

[1] R. D. Farahani, H. Dalir, V. L. Borgne, L. A. Gautier, M. A. E. Khakani, M. Lévesque, D. Therriault, *Nanotechnology* **2012**, *23*, 085502.

[2] X. Xiao, L. Yuan, J. Zhong, T. Ding, Y. Liu, Z. Cai, Y. Rong, H. Han, J. Zhou, Z. L. Wang, *Adv. Mater.* **2011**, *23*, 5440.

[3] J. Yeom, M. A. Shannon, *Adv. Funct. Mater.* **2010**, *20*, 289.

[4] D. Therriault, S. R. White, J. A. Lewis, *Nat. Mater.* **2003**, *2*, 265.

[5] L. Y. Yeo, H.-C. Chang, P. P. Y. Chan, J. R. Friend, *Small* **2011**, *7*, 12.

[6] A. R. Hamilton, N. R. Sottos, S. R. White, *Adv. Mater.* **2010**, *22*, 5159.

[7] B. J. Blaiszik, S. L. B. Kramer, M. E. Grady, D. A. McIlroy, J. S. Moore, N. R. Sottos, S. R. White, *Adv. Mater.* **2012**, *24*, 398.

[8] A. P. Esser-Kahn, N. R. Sottos, S. R. White, J. S. Moore, *J. Am. Chem. Soc.* **2010**, *132*, 10266.

[9] K. S. Toohey, N. R. Sottos, J. A. Lewis, J. S. Moore, S. R. White, *Nat. Mater.* **2007**, *6*, 581.

[10] F. Klein, B. Richter, T. Striebel, C. M. Franz, G. v. Freymann, M. Wegener, M. Bastmeyer, *Adv. Mater.* **2011**, *23*, 1341.

[11] S. M. Berry, S. P. Warren, D. A. Hilgart, A. T. Schworer, S. Pabba, A. S. Gobin, R. W. Cohn, R. S. Keynton, *Biomaterials* **2011**, *32*, 1872.

[12] T. G. Leong, A. M. Zarafshar, D. H. Gracias, *Small* **2010**, *6*, 792.

[13] A. Yamada, F. Niikura, K. Ikuta, *J. Micromech. Microeng.* **2008**, *18*, 025035.

[14] T. D. Brown, P. D. Dalton, D. W. Hutmacher, *Adv. Mater.* **2011**, *23*, 5651.

[15] T. Yang, D. Wu, L. Lu, W. Zhou, M. Zhang, *Polym. Compos.* **2011**, *32*, 1280.

[16] C. A. Bonino, K. Efimenko, S. I. Jeong, M. D. Krebs, E. Alsberg, S. A. Khan, *Small* **2012**, *8*, 1928.

[17] J. A. Lewis, G. M. Gratson, *Mater. Today* **2004**, *7*, 32.

[18] D. Therriault, R. F. Shepherd, S. R. White, J. A. Lewis, *Adv. Mater.* **2005**, *17*, 395.

[19] G. M. Gratson, M. Xu, J. A. Lewis, *Nature* **2004**, *428*, 386.

[20] J. E. Smay, G. M. Gratson, R. F. Shepherd, J. Cesarano, J. A. Lewis, *Adv. Mater.* **2002**, *14*, 1279.

[21]B. Y. Ahn, D. Shoji, C. J. Hansen, E. Hong, D. C. Dunand, J. A. Lewis, *Adv. Mater.* **2010**, *22*, 2251.

[22] J. J. Adams, E. B. Duoss, T. F. Malkowski, M. J. Motala, B. Y. Ahn, R. G. Nuzzo, J. T. Bernhard, J. A. Lewis, *Adv. Mater.* **2011**, *23*, 1335.

[23] J. N. Hanson Shepherd, S. T. Parker, R. F. Shepherd, M. U. Gillette, J. A. Lewis, R. G. Nuzzo, *Adv. Funct. Mater.* **2011**, *21*, 47.

[24] R. A. Barry, R. F. Shepherd, J. N. Hanson, R. G. Nuzzo, P. Wiltzius, J. A. Lewis, *Adv. Mater.* **2009**, *21*, 2407.

[25] L. L. Lebel, B. Aissa, M. A. El Khakani, D. Therriault, *Adv. Mater.* **2010**, *22*, 592.

[26] Z. Gou, A. J. McHugh, *J. Non-Newtonian Fluid Mech.* **2004**, *118*, 121.

[27] N. Becker, E. Oroudjev, S. Mutz, J. P. Cleveland, P. K. Hansma, C. Y. Hayashi, D. E. Makarov, H. G. Hansma, *Nat. Mater.* **2003**, *2*, 278.

[28] J. Zhu, X. Xuan, *Biomicrofluidics* **2011**, *5*, 024111.

[29] H. Dong, A. P. Esser-Kahn, P. R. Thakre, J. F. Patrick, N. R. Sottos, S. R. White, J. S. Moore, *ACS Appl. Mater. Interfaces* **2012**, *4*, 503.

[30] J. Bruneaux, D. Therriault, M. C. Heuzey, *J. Micromech. Microeng.* **2008**, *18*, 115020.

3.4 Supporting information:

The videos of the fabrication of the microstructures are available online and the links are as follows:

Square spiral: https://www.youtube.com/watch?v=hgIjy3QeGbY

Circular spiral: https://www.youtube.com/watch?v=z036i7xZPcg

Scaffold: https://www.youtube.com/watch?v=FPtFpBneMIE

Micro-cup: https://www.youtube.com/watch?v=IXMCSkj5TlI

Microstructured fiber: https://www.youtube.com/watch?v=FzWDj8tgb18

Tensile coupon: http://www.youtube.com/watch?v=hrmeZQC7M-M

Application I: High-toughness fiber

Whereas an ever more precise control is typically sought after in 3-D printing applications, here we developed high-toughness microstructured fibers inspired by the molecular structure of spider silk proteins. To fabricate microfibers with various mechanical properties, we yield the control of their exact geometry to the liquid rope coiling instability. This instability causes a thread of honey to wiggle as it buckles when hitting a surface. Similarly, we extrude a filament of viscous polymer solution towards a substrate moving perpendicularly at a slower velocity than the filament flows (Figure 3.5 a, b). The filament buckles repetitively giving rise to periodic meanders and stitch patterns. As the solvent evaporates, the filament solidifies into a fiber with a geometry bestowed by the instability (Figure 3.4b).

Uniaxial tension tests performed on fibers show interesting links between the mechanical properties and the instability patterns. By varying the instability parameters, the properties of the fabricated fibers can be tailored. For instance, straight fibers made by matching the extrusion and substrate speeds (Figure 3.4a) are stiffer whereas meandering and coiling patterned fibers possess a higher breaking strain. The coiling patterns give rise to a toughening mechanism due to the sacrificial bonds created when the viscous filament loops over itself and fuse. Work is ongoing to optimise the coiling instability parameters to maximise the breaking energy by making use of the sacrificial bond toughening mechanism (Figure 3.4d).

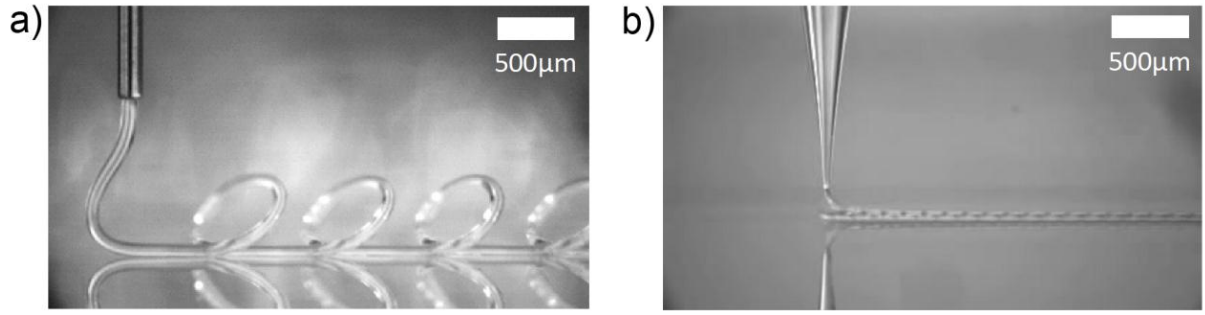

Figure 3.5 Instability assisted microfabrication by solvent-cast direct write with (a) 100 µm diameter needle; (b) 30 µm diameter glass capillary. During the microfabrication process, only the substrate moves in a straight line. The liquid rope coiling instability gives rise to various patterns. As the solvent evaporates, it leaves behind a solidified microstructured fiber.

Application II: Microfluidic channel

Microfluidic channels have a large number of applications in different domains. They are fabricated mostly using conventional microfabrication techniques such as photolithography and etching, soft lithography or micromoulding. These techniques allow for a wide variety of shapes and sizes but do not allow for complex 3-D-shaped channels. Several applications would benefit from 3-D-shaped channels such as mixing of different fluids in microchannels.[4]

Here, solvent-cast PLA printing method allows for the fabrication of 3-D channels through catalytic depolymerization. The depolymerisation happens when heat breaks the polymer chain and dissociate the PLA into monomers or very short-chain polymers which are gaseous at 200 ℃. The relatively low depolymerization temperature allow PLA fibers to be removed from a fully cured epoxy thermoset resin without causing significant thermal damage to the epoxy (Figure 3.6). This microchannel fabrication technique is promising because of the possibility to fabricate channels in a large variety of shapes. The chaotic mixer presented in Therriault et al[4] could be fabricated in a much simpler process using the catalytic depolymerisation of freeform deposited PLA. Microfluidic biomedical devices are also an area where this novel technique could be advantageous.

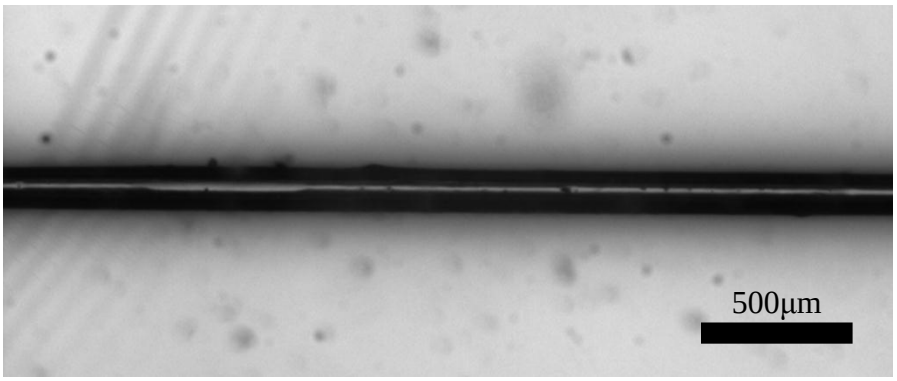

Figure 3.6 Empty channel in epoxy left after the catalytic depolymerization of PLA using Tin(II) Oxalate as a catalyst in an vacuum oven at a temperature of 200 ℃ and an absolute pressure of 0.1 inHg for 48 h.

Application III: 3-D spiral antenna

Another example of self-supporting structure that could be made using the solvent-cast printing method is a small spiral Ka band (20-30 GHz) antenna. The antenna features a variable pitch for double band functionality (uplink frequencies: 30.0 to 31.0 GHz, downlink frequencies: 20.2 to 21.2 GHz) and a right hand circular polarization (RHCP). Futher charaterization and optimization of the structure design are ongoing to improve antenna performance. In addition,we are currently working on the 3-D printing of electrically conductive features without the use of sputtering.

CHAPTER 4: Article 2: Properties of Polylactide Inks for Solvent-Cast Printing of Three-Dimensional Freeform Microstructures

Shuangzhuang Guo, Marie-Claude Heuzey and Daniel Therriault, published in *Langmuir*, DOI: 10.1021/la4036425, January 10, 2014.

4.1 Abstract

Solvent-cast printing is a highly versatile microfabrication technique that can be used to construct various geometries such as filaments, towers, scaffolds, and freeform circular spirals by the robotic deposition of a polymer solution ink onto a moving stage. In this work, we have performed a comprehensive characterization of the solvent-cast printing process using polylactide (PLA) solutions by analyzing the flow behavior of the solutions, the solvent evaporation kinetics, and the effect of process-related parameters on the crystallization of the extruded filaments. Rotational rheometry at low to moderate shear rates showed a nearly Newtonian behavior of the PLA solutions, while capillary flow analysis based on process-related data indicated shear-thinning at high shear rates. Solvent vaporization tests suggested that the internal diffusion of the solvent through the filaments controlled the solvent removal of the extrudates. Different kinds of three-dimensional (3D) structures including a layer-by-layer tower, nine-layer scaffold, and freeform spiral were fabricated, and a processing map was given to show the proper ranges of process-related parameters (*i.e.*, polymer content, applied pressure, nozzle diameter, and robot velocity) for the different geometries. The results of differential scanning calorimetry revealed that slow solvent evaporation could increase the ability of PLA to complete its crystallization process during the filament drying stage. The method developed here offers a new perspective for manufacturing complex structures from polymer solutions and provides guidelines to optimize the various parameters for 3D geometry fabrication.

4.2 Introduction

There is a growing interest toward the fabrication of three-dimensional (3D) micro- or nanoscale devices made from thermoset,[1] or thermoplastic polymers,[2] hydrogels,[3,4] or polyelectrolytes,[5] which may find potential applications in complex microfluidic networks,[6,7]

tissue engineering scaffolds,[8,9] and self-supporting sensors.[10,11] Several strategies have been employed to precisely assemble 3D structures, including photolithographic,[12] colloidal-epitaxy,[13] and direct-write techniques.[14-15] Among these, the direct-write assembly is one of the most promising approaches because it offers flexibility in material selection, low cost, and ability to construct complex 3D structures.[16] Direct-write assembly is a 3D printing technique, which employs a computer-controlled translational stage that moves a pattern-generating device in order to achieve, layer by layer, the desired 3D microstructure.[17] Different materials such as organic fugitive,[7, 15, 18-20] or colloidal inks,[21-23] concentrated polyelectrolytes,[24,25] UV curable thermosets,[1,10] and bioinks (e.g. hydrogels with suspended cells),[26-28] have been employed in this technique to fabricate various microstructures for specific applications.

Polylactide (PLA) is one of the most popular bio-based thermoplastic materials because it is widely available commercially, biodegradable, biocompatible, and has a relative high strength, high modulus, and good processability.[29-31] A few techniques using PLA to fabricate microscale 3D geometries have been developed and described in the literature. For example, a fused deposition modeling (FDM) method can create PLA solid objects with ~250 μm resolution due to the material rigidity increase after the temperature-triggered phase transition from molten to solid state.[32] However this method exhibits limited precision of the printed features, and the high viscosity and/or thermal degradation at high temperature of thermoplastic melts may restrict this approach. In addition, two other methods including surface tension driven direct-write[33] and soft lithographic approaches[34] were reported to fabricate 3D PLA scaffolds for tissue engineering. However, these techniques were unable to build complex or freeform 3D structures.

We recently reported the solvent-cast direct-write printing of 3D geometries in a freeform fashion using concentrated PLA solution inks[35] as illustrated in Figure 4.1. Specifically, the inks are formulated by dissolving PLA in a solvent with low boiling point. The resulting solutions are extruded through micronozzles upon the application of an appropriate pressure. They rapidly undergo fluid-like to solid-like transition postextrusion due to fast solvent evaporation, which allows maintaining their filamentary shape and buildup of complex structures.

In this paper, we present a comprehensive study of the properties of PLA solution inks for the solvent-cast printing method. The information gathered here aims at elucidating the phase behavior and rheological properties of the inks during the solvent-cast printing process and can be used as a guide for the fabrication of different 2D and 3D geometries. The process-related viscosity of PLA solutions is investigated by capillary flow analysis. The solvent evaporation kinetics are characterized by monitoring the weight reduction of short extruded filaments over time. In addition, a map of processing parameters ranges for different microstructure fabrication is proposed. Finally, the crystallization properties of the extrudates are examined using a differential scanning calorimetry (DSC).

4.3 Experimental section

Polymer Solution Preparation

A semicrystalline polylactide (PLA, grade 4032D, Nature works LLC) with a stereoisomer composition of 1.2-1.6% *D*-isomer lactide and a weight-average molecular weight (Mw) of 207K Dalton, was used in this study. Various amounts of neat PLA (20, 25, and 30 wt% solutions) were dissolved in the solvent dichloromethane (DCM, Sigma-Aldrich). After 24 h, the solutions were ultrasonicated (ultrasonic cleaner 8891, Cole-Parmer) at 42 kHz for 1 h. Then the polymer solutions were stored in sealed bottles until processing.

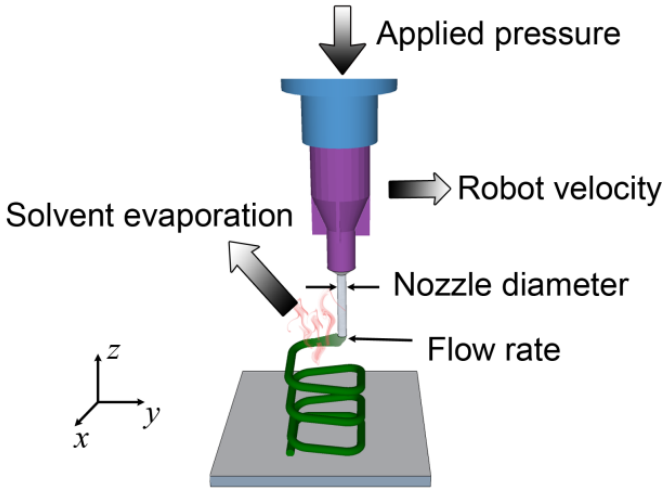

Figure 4.1 Schematic of the solvent-cast printing process and the main process parameters.

3D Printing

The solvent-cast printing was performed using a moving stage along the *x*-axis and a robot head (I&J2200-4, I&J Fisnar) moving in the *y*-*z* plane that were computer-controlled with commercial software (JR Points for Dispensing, Janome Sewing Machine). The PLA solution was poured in a syringe (3 cm^3 barrel, EFD) fixed on the robot and deposited through a micronozzle onto a glass substrate at room temperature. The pressure applied on the polymer solution (0 - 4.2 MPa) was controlled by an air-powered dispensing system (HP-7X, EFD). This experimental setup was also used in the capillary flow analysis, the solvent evaporation tests, and the fabrication of the different geometries.

Rheological Characterization

The process-related viscosities of polymer solutions with various PLA contents (20, 25, and 30 wt%) were evaluated from constant-pressure capillary flow analysis as described in ref20. The different PLA solutions were extruded through a single size micronozzle (inner diameter D = 200 μm, capillary length L = 12.24 mm) and the 25 wt% PLA solution was also extruded through two other nozzles (D = 100 and 330 μm, L = 12.76 and 12.24 mm). The high-capacity pressure dispenser was set between 0.18 and 4.0 MPa to obtain the desired flow rate, depending on the PLA content and nozzle diameter. After reaching the extrusion steady state, the ink was deposited onto a substrate for 120 s under various applied pressures at a robot velocity 0.5 mm s^{-1}. After drying in an oven (G05053-10, Cole-Parmer) at 50 ℃ for 12 h, the extruded fibers were then weighed with a high precision balance (GH-202, A&D Engineering) to determine the mass flow rates, which were converted to volumetric flow rates using the respective fluid densities. Capillary data reported in this work include the Rabinowitch-Mooney correction for non-Newtonian fluids.

The steady-state shear viscosity of the polymer solutions was also characterized at room temperature using a rotational rheometer (MCR-502, Anton Paar) with a pressure flow cell (CC25 concentric cylinder geometry) to prevent solvent evaporation. The shear rate ramp started from 0.1 s^{-1} and increased until flow instabilities were observed at $\sim$ 100 s^{-1}, where the viscosity dramatically decreased. Each polymer solution was tested under ambient pressure and three different applied cell pressures (1.0, 2.0 and 4.0 MPa).

Solvent Evaporation Rate Characterization

The solvent evaporation behavior of the polymer inks was evaluated by directly depositing a 5 mm long filament on a glass substrate resting on a high-precision balance (GH-202, A&D Engineering). Three polymer solutions (PLA contents of 20, 25, and 30 wt%) were deposited on the substrates for 5 s through a micronozzle (D = 510 μm) under an applied pressure of 420 kPa. The 20 wt% PLA solution was also deposited using two other nozzles (D = 200 and 330 μm). The sample weight was recorded for 6 h. Following this recording period, the sample was completely dried in an oven (G05053-10, Cole-Parmer) at 50 ℃ for 12 h and weighed again. The mass of the dried PLA was then used to calculate the real-time solvent percentage in the extruded filament.

Microstructure Fabrication

2D and 3D microstructures were fabricated using the solvent-cast printing technique. A nine-layer scaffold was fabricated with the 25 wt% PLA solution using a 100 μm inner diameter nozzle under an applied pressure of 1.4 MPa and 1.0 mm s^{-1} robot velocity. Square and circular towers were built with the 30 wt% PLA solution using a nozzle with a 200 μm inner diameter under an applied pressure of 1.05 MPa and 0.5 mm s^{-1} robot velocity. A 3D circular spiral was fabricated from the 30 wt% PLA solution using a micronozzle with a 100 μm inner diameter under an applied pressure of 1.75 MPa and 0.1 mm s^{-1} robot velocity. The designed pitch of the circular spiral and the radius of the coil were 0.5 mm.

Morphological Characterization

The morphology of the various microstructures was observed on a JEOL JSM-840 scanning electron microscope (SEM). Samples were sputtered with gold for 15 s prior to the imaging.

Thermal Analysis

Critical transition temperatures and extent of crystallization of the printed PLA filaments were determined using differential scanning calorimetry (DSC Q1000, TA Instruments) in a nitrogen atmosphere. Ten samples were prepared by depositing PLA filaments using different process parameters. Details of the various experiments are provided in Table 4.1 where, for example, the nomenclature of 20%/200 μm/1.05 MPa/0.5 mms^{-1} represents a filament specimen fabricated using the 20 wt% PLA solution, 200 μm inner diameter nozzle, 1.05 MPa applied pressure and 0.5 mm s^{-1} robot velocity. After drying the printed filaments in an oven at 50 ℃ for 12 h, the samples were cut

Table 4.1 DSC results of solvent-cast PLA filament crystallization

sample nomenclature *	ΔH_m (J g^{-1})	ΔH_{cc} (J g^{-1})	$\Delta H_{\alpha\prime\rightarrow\alpha}$ (J g^{-1})	χ_c (%)
20%/200 μm/1.05 MPa/0.5 mms^{-1}	36.8	16.3	0.73	21.1
25%/200 μm/0.56 MPa/0.5 mms^{-1}	32.3	23.8	0.90	8.1
25%/200 μm/1.05 MPa/0.5 mms^{-1}	35.1	15.9	0.59	19.9
25%/200 μm/1.05 MPa/0.2 mms^{-1}	32.1	4.9	0.00	29.0
25%/200 μm/1.05 MPa/1.0 mms^{-1}	34.9	24.8	0.72	10.1
25%/200 μm/1.05 MPa/2.0 mms^{-1}	29.2	21.5	0.83	7.3
25%/200 μm/2.84 MPa/0.5 mms^{-1}	34.0	2.7	0.00	33.4
25%/100 μm/1.05 MPa/0.5 mms^{-1}	31.0	18.9	1.29	11.5
25%/330 μm/1.05 MPa/0.5 mms^{-1}	35.3	2.0	0.00	35.5
30%/200 μm/1.05 MPa/0.5 mms^{-1}	35.3	17.0	0.71	18.8

* Nomenclature: PLA content/nozzle diameter/applied pressure/robot velocity

and placed in sealed aluminum pans. For each sample, the heat flow measurements were performed during a heating from 30 to 210 ℃ at a heating rate of 10 ℃ min^{-1}. The glass transition temperature (T_g), cold crystallization temperature (T_{cc}), melting temperature (T_m), and degree of crystallinity (χ_c) were determined from the measured thermograms.

4.4 Results and discussion

Rheological Properties

This printing process involves the flow of a polymer solution inside a nozzle; hence, rheological properties of the solution inks are critical. The solution must exhibit a moderate viscosity, so it can flow easily through the fine nozzle and result in a stable filament. Since polymer solutions exhibit high viscosity, a shear-shinning behavior of the extruded material is favorable. The flow behavior of various PLA solutions under two different operating conditions (*i.e.*, nozzle diameter and applied pressure) was examined using capillary flow analysis from the process related raw data, as explained below. Because of the limitation of the balance precision, it's difficult to measure the weight of fiber fabricated using 30 wt% PLA solution. Hence, the

minimum diameter of the nozzle was 200 μm for 30 wt% PLA solution. Figure 4.2 shows the volumetric flow rate converted from mass flow rate with respect to the applied pressure. For all PLA solutions investigated, the flow rate increased with the applied pressure, as expected. Under the same pressure, the flow rate decreased as the PLA content increased (Figure 4.2a) and as the nozzle diameter decreased (Figure 4.2b).

Because the ratio of micronozzle length (L) to diameter (D) is larger than 50, the end effects in the capillary flow analysis was neglected[17]. It is also assumed that the pressure has negligible effect on the viscosity. The process-related wall shear stress τ_w is calculated from the following equation:

$$\tau_w = \Delta P \cdot R/2L \tag{4.1}$$

where ΔP is the applied pressure during the process, and R is the nozzle inner radius. The wall shear rate $\dot{\gamma}_w$ is determined from the volumetric flow rate Q, by first calculating the Newtonian shear rate $\dot{\gamma}_{Newt}$:

$$\dot{\gamma}_{Newt} = 4Q/\pi R^3 \tag{4.2}$$

and correcting for non-Newtonian effects using

$$\dot{\gamma}_w = \dot{\gamma}_{Newt}\,(3n+1)/4n \tag{4.3}$$

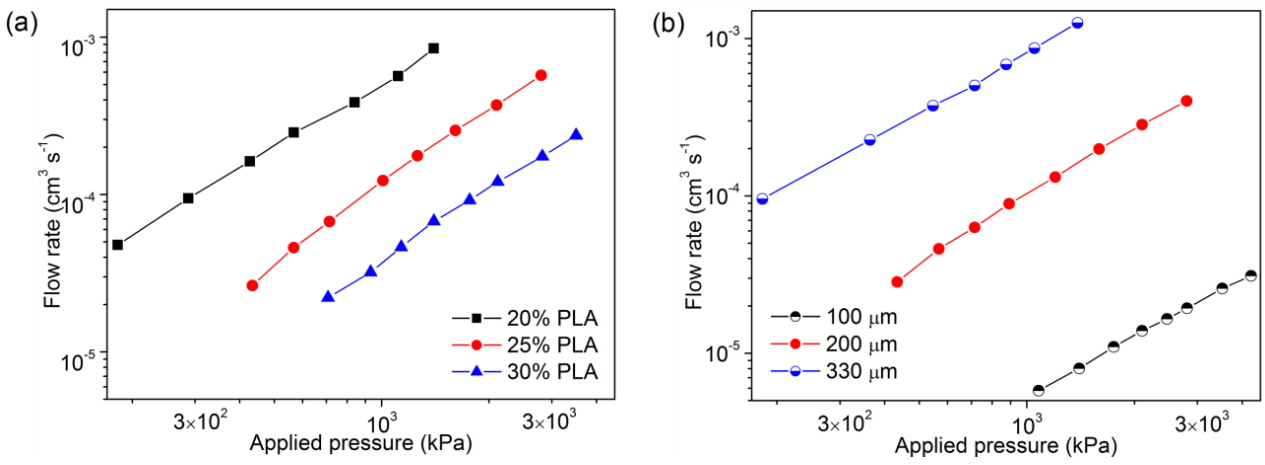

Figure 4.2 Raw data of the capillary flow experiments: volumetric flow rate as a function of the applied pressure for (a) three PLA solutions (20, 25, and 30 wt%) deposited using a 200 μm nozzle and (b) a 25 wt% PLA solution deposited using three different nozzle diameters (100, 200, and 330 μm).

where the bracketed term is the Rabinowitch-Mooney correction. The parameter n is defined by

$$n = d\log(\tau_w)/d\log(\dot{\gamma}_w) \tag{4.4}$$

which can be determined from the slope of the log-log plot of τ_w versus $\dot{\gamma}_{Newt}$. Therefore with Equation (4.3) that represents the process-related shear rate, the apparent viscosity of the polymer solution can be determined from:

$$\eta_{app} = \tau_w/\dot{\gamma}_W \tag{4.5}$$

The solid symbols in Figure 4.3 represent the apparent process viscosity as a function of the process-related shear rate $\dot{\gamma}_w$ for three different solutions (*i.e.*, 20, 25 and 30 wt% PLA content), calculated from the capillary flow data obtained using a nozzle diameter of 200 μm. The three PLA solutions exhibited a shear-thinning behavior over the investigated shear rates. The lower shear rate limit was attributed to the balance precision used to determine the mass flow rate. This lower limit decreased as the PLA content increased. In addition, the results of apparent viscosity

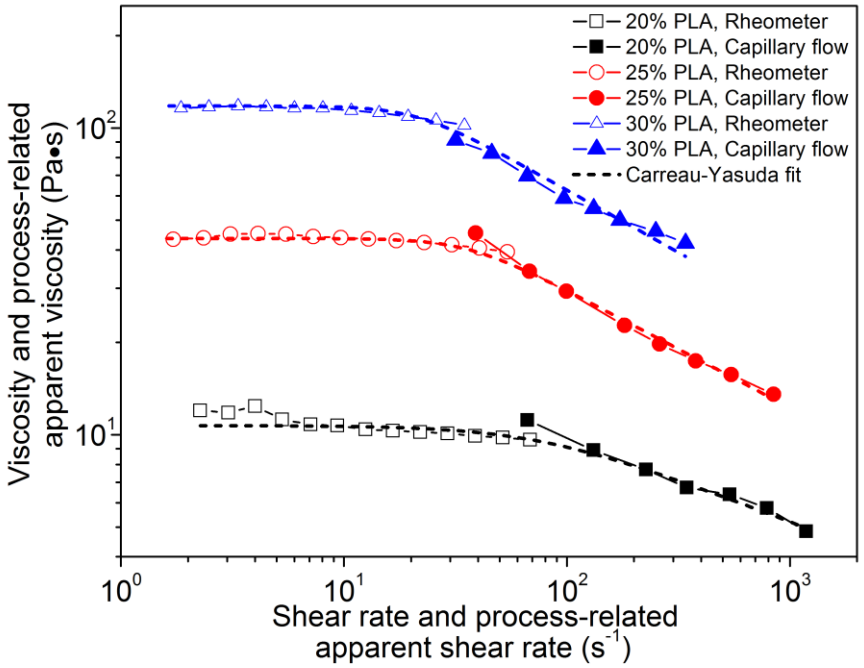

Figure 4.3 Viscosity as a function of shear rate for three PLA solutions. (open symbols: data obtained using a concentric cylinder flow geometry in steady simple shear, solid symbols: data obtained by extrusion of the PLA solutions with a 200 μm nozzle in capillary flow analysis, dashed lines: fits of Carreau-Yasuda model with parameters of the fit given in Table 4.2).

as a function of the process-related shear rate for the 25 wt% PLA solution for two other nozzle diameters (*i.e.*, 100 and 330 μm) (not shown here) indicated no specific dependence of the apparent viscosity on nozzle size, hence no obvious wall effects.

The open symbols in Figure 4.3 show the viscosities of the three PLA solutions (*i.e.*, 20, 25 and 30 wt%) as functions of shear rate, measured in rotational rheometry under ambient pressure and steady simple shear. The three PLA solutions exhibited a Newtonian behavior over the range of low to moderate shear rates ($\sim$ 2 - 80 s^{-1}) allowable during the rotational rheometry tests. The upper limitation of achievable high shear rate was due to flow instabilities of the polymer solutions, where the viscosities sharply decreased. The upper limit of shear rate increased slightly as the PLA content decreased from 30 wt% to 20 wt% because the latter is less elastic. In addition, the flow behavior of the three PLA solutions under different applied pressures (1.0, 2.0 and 4.0 MPa) was nearly the same (not shown here), which demonstrated that the pressure range used in the fabricating process had negligible effect on the ink's viscosity. The rotational rheometry and process-related data agree reasonably well, showing a bimodal behavior from a nearly Newtonian regime followed by a significant power-law drop. The rheological measurements also revealed that the viscosity of PLA solutions was greatly affected by PLA content. Under the same shear rate, the viscosity of the 30 wt% PLA solution was almost one order of magnitude superior to that of the 20 wt% PLA solution.

The dashed lines in Figure 4.3 represent the fits of the Carreau-Yasuda model, which is quite flexible in fitting the non-Newtonian behavior of $\eta(\dot{\gamma})$ over a wide range of shear rate, and is expressed as follows

$$\frac{\eta-\eta_\infty}{\eta_0-\eta_\infty} = [1 + |t_1\dot{\gamma}|^a]^{(n-1)/a} \tag{4.6}$$

where η_0 is the zero-shear-rate viscosity, η_∞ is the infinite-shear-rate viscosity, t_1 is a critical time constant, (n-1) is the power law exponent, and a is a dimensionless parameter that describes the width of the transition between the zero-shear-rate and power-law regions. For polymer solutions, $\eta_\infty \approx 0$. The fitting parameters of Equation (4.6) for the curves superimposed on the experimental data of Figure 4.3 are given in Table 4.2. The relatively good fit of the Carreau-Yasuda model confirms that the calculation of the viscosity from the process-related data gives quite reasonable values. The η_0 values increase with PLA content, as expected, and the transition from Newtonian to power-law regime is shifted to lower shear rates. The shear-thinning character also increases

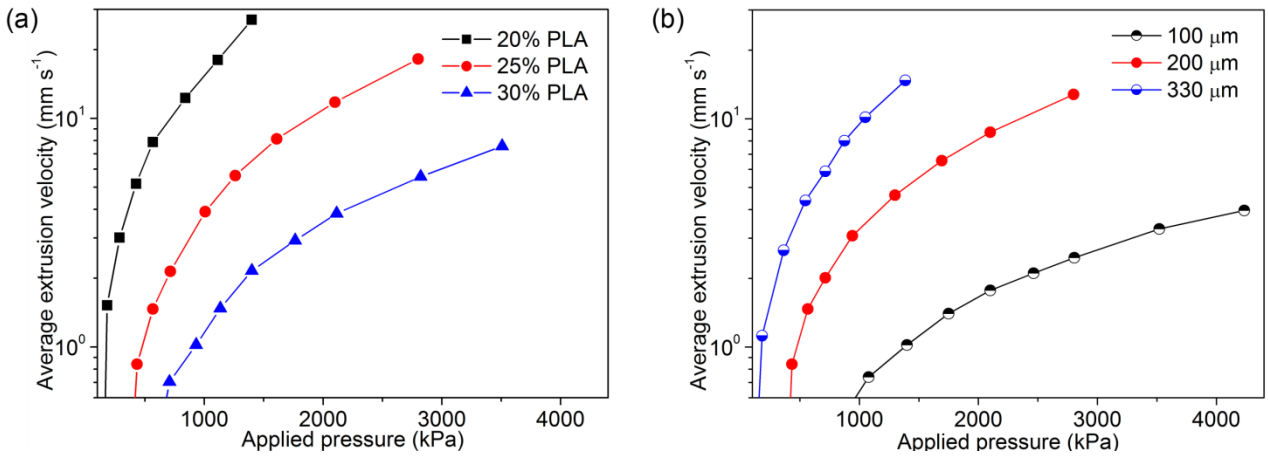

Figure 4.4 Average extrusion velocity as a function of applied pressure for (a) different PLA solutions (20, 25 and 30 wt%) deposited using a 200 µm nozzle, and (b) a 25 wt% PLA solution deposited using three different nozzle diameters (100, 200 and 330 µm) (data from Figure 4.2).

with PLA concentration (lower *n*). The parameters listed in Table 4.2 may be useful for further modeling purposes of the printing process.

Table 4.2 Parameter values of the Carreau-Yasuda model fit for the PLA solutions (data from Figure 4.3).

PLA content (wt%)	η_0 (Pa • s)	t1 (s)	a -	n -	adj. R2 -
20	10.7	0.013	1.62	0.72	0.91
25	43.6	0.028	3.15	0.62	0.98
30	118	0.047	3.36	0.59	0.98

Figure 4.4 presents the calculated average material extrusion velocity as a function of the applied pressure for the same PLA contents extruded from a nozzle diameter of 200 µm (Figure 4.4a), and for the 25 wt% PLA solution extruded from different nozzle diameters (100, 200 and 330 µm) (Figure 4.4b). The velocity data were calculated from the raw volumetric flow rate data (Figure 4.2) divided by the nozzle cross-sectional area. These plots are important to set the

fabrication parameters for successful 3D printing, by adjusting the pressure of the dispenser system with the corresponding robot velocity for various inks and nozzle sizes. The polymer solutions exhibited different flow behaviors where higher PLA contents led to higher viscosities and hence lower average velocities (Figure 4.4a). Moreover, larger nozzle diameters caused higher average velocities for the same PLA solution (Figure 4.4b). At the same pressure, the average extrusion velocity from the 330 μm nozzle was approximately 10 times that of the 100 μm nozzle. In addition, the extrapolation of the velocity curves toward low pressures shows a minimum pressure required for flow, as observed during the printing process. This minimum pressure may have similarity with the concept of yield stress, though this is not expected from a polymer solution and is most likely inherent to the process itself.

Solvent Evaporation Rate

After the filament extrusion from the micronozzle, the solvent evaporation plays a crucial role in the phase change from solution to solid to guarantee geometric retention. There are three mechanisms of solvent removal from the extruded filament: 1) flash vaporization, 2) diffusion within the filament, and 3) convective transfer from the filament surface to the surrounding air.[36-38] Flash vaporization takes place near the nozzle tip due to a high-pressure drop after the filament extrusion. Next, the solvent molecules must diffuse through the filament (internal diffusion) in order to evaporate at the air/filament interface (external convection). In this work, the solvent evaporation behavior was investigated by monitoring the weight reduction of deposited filaments as a function of time using a high-precision balance. Figure 5a shows the evolution with time of the normalized solvent content (divided by the solvent content at the measurement starting point) for short filaments (length of $\sim$ 5 mm) deposited using three different PLA solutions (20, 25 and 30 wt%) through a 510 μm inner diameter nozzle. Since there were initial fluctuations of the balance readings during the first 10 s, the mechanism of flash vaporization was not adequately captured during the experiments and is not reported. For the filaments extruded using different PLA solutions, the plots of normalized solvent content versus time had no distinct difference (Figure 4.5a). In other words, the initial solvent contents had no obvious effects on the solvent internal diffusion, which was also shown by Kojić *et al*.[39] However, when raw evaporation data is examined[35] (*i.e.*, not normalized), the most concentrated PLA solution is the one that solidifies the fastest. Figure 4.5b displays the normalized evaporation data for filaments extruded using the 20 wt% PLA solution through different nozzle diameters (200, 330 and 510 μm). The solvent evaporation

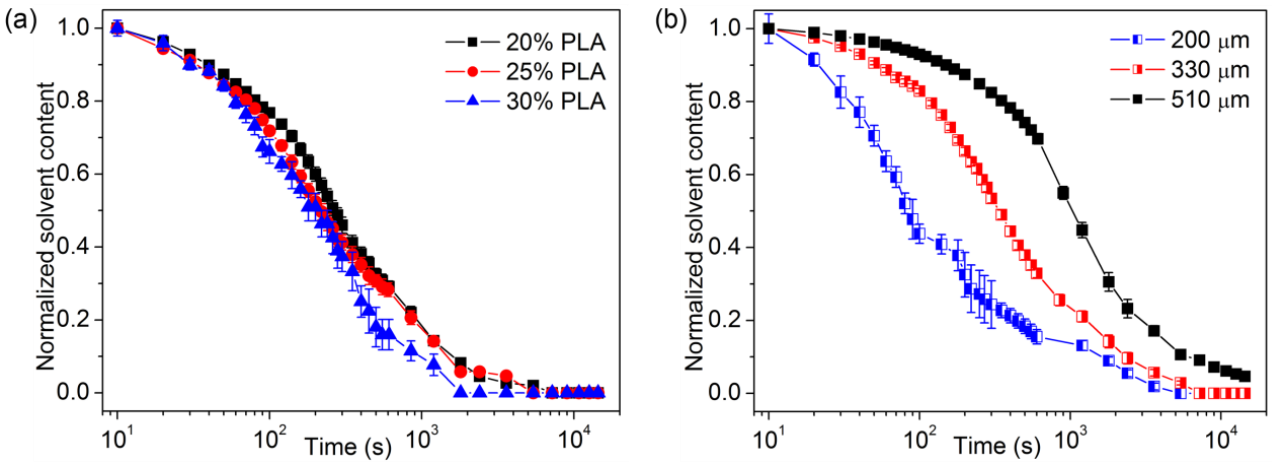

Figure 4.5 Normalized solvent content as a function of time for (a) three 5 mm long PLA filaments deposited using a 510 μm nozzle under 0.42 MPa applied pressure and 1 mm s^{-1} robot velocity and (b) 20 wt% PLA solution deposited using three different nozzles under 0.42 MPa applied pressure and 1 mm s^{-1} robot velocity for 5 s.

rate significantly increased as the filament diameter decreased, because the solvent internal diffusion was greatly accelerated by shortening the diffusion distance. From the results of Figure 4.5, it seems that the internal diffusion of the solvent through the filament is the governing process for the solvent removal of the extrudates. In other words, the smaller the extruded filament is, the faster does its rigidity increase.

Microstructure Fabrication

The four main printing parameters in this work are PLA content, applied pressure, nozzle diameter, and robot velocity, which greatly affect the diameter of the extruded filament and the solvent evaporation rate (corresponding to filament rigidity increase). The fastest solvent evaporation could be achieved by either increasing the PLA content[35] or the robot velocity, or by decreasing either the applied pressure or the nozzle diameter. The applied pressure and robot velocity can be appropriately set from 0 to 4.2 MPa, and from 0.1 to 500 mm s^{-1}, respectively, guided by the rheological data shown in Figure 4.4 and trial error. Three PLA solutions (PLA content of 20, 25, and 30 wt%) and six nozzles (D = 100, 150, 200, 250, 330, and 510 μm) were used in this process mapping. The successful fabrication of different geometries (*e.g.*, 1D filament,

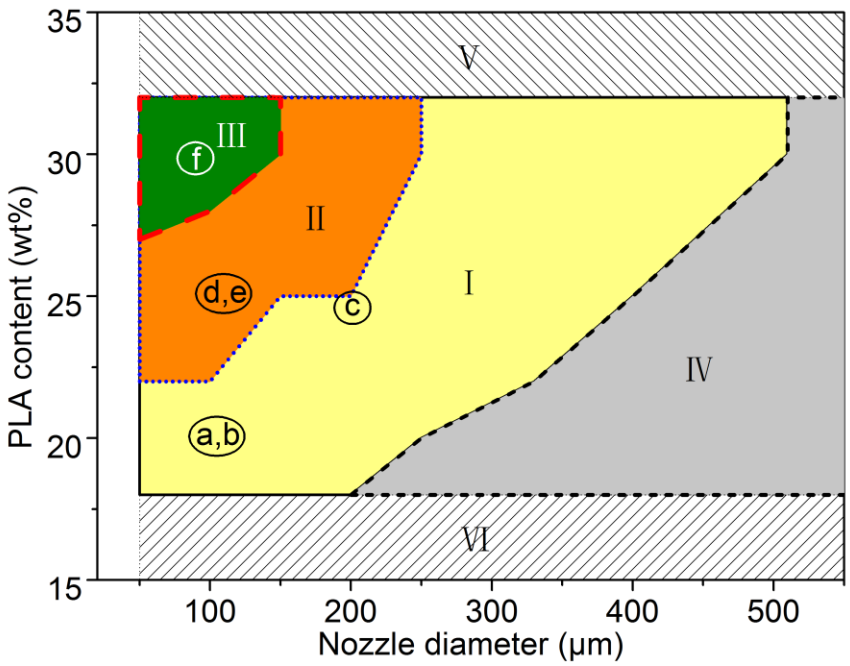

Figure 4.6 Solvent-cast printing processing map showing the parameter ranges for different microstructures fabrication. I: zone for 1D filament, II: zone for 2D filament array or 3D layer-by-layer structure; III: zone for 3D freeform geometry; IV: zone where filaments break; V: zone where PLA is not dissolvable; VI: zone where PLA solutions are too dilute for the process. The letters a-f represent the fabrication parameters of different geometries shown in Figure 4.7.

2D network, 3D layer-by-layer, and freeform structure) required different solidification speeds, hence different solvent evaporation rates, formulations and operating conditions. Figure 4.6 shows a processing map with approximate ranges of PLA content and nozzle diameter for the fabrication of different geometries. Zone I in Figure 4.6 indicates that a 1D filament could be easily fabricated using a wide range of parameters values. As part of zone I, zone II reveals that the fabrication of a 2D network or a 3D layer-by-layer structure needed faster solvent evaporation rate, which meant a narrower range of parameter values. Moreover, to fabricate 3D freeform structures, the solvent must evaporate much faster so that the geometry exhibits enough rigidity to support itself right after extrusion. Therefore, zone III indicates that successful 3D freeform fabrication could only be achieved using much smaller nozzles and the more viscous PLA solutions. In addition, zone IV displays that it was difficult to fabricate continuous and smooth filament using larger nozzle

diameters. Finally, zone V indicates that PLA was insoluble in DCM at high content (> 32%), and zone VI shows that more dilute PLA solutions could be used in solvent-cast printing.

Various geometries with different dimensions were printed using the right conditions indicated in Figure 4.6. Figure 4.7a shows SEM images of a typical filament circular cross-section with a diameter of ～ 100 μm, which was fabricated with the 20 wt% PLA solution using a 100 μm inner diameter nozzle, under an applied pressure of 0.4 MPa and 1.0 mm s^{-1} robot velocity. Figure 4.7b displays a close-up view of the relatively smooth surface of the PLA filament. Figure

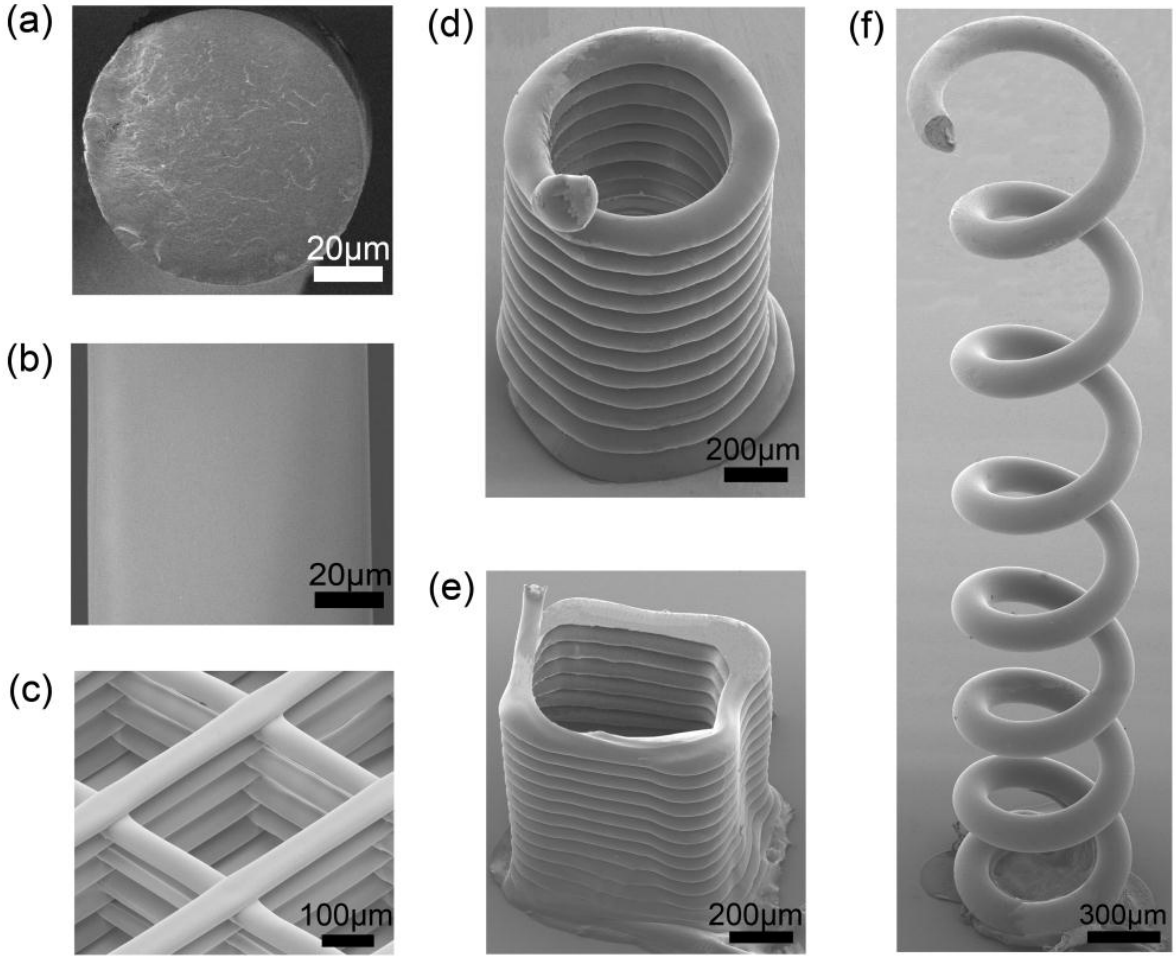

Figure 4.7 Morphology of various printed microstructures. (a) Representative SEM image of the PLA filament circular cross section. (b) Representative SEM image of the filament smooth surface. (c) Inclined top view SEM image of PLA 9-layer scaffold. (d) SEM image of a PLA circular tower. (e) SEM image of a PLA square tower. (f) Inclined top view SEM image of a PLA circular spiral.

4.7c reveals a scaffold consisting of nine 2D filament layers, which was fabricated with the 25 wt% PLA solution using a 100 μm inner diameter nozzle, under an applied pressure of 1.4 MPa and 1.0 mm s^{-1} robot velocity. The scaffold was almost identical to its programmed deposition paths because the printing layer was always supported by the underlying layer. Figure 4.7d,e show 3D circular and square towers, which were built with the 25 wt% PLA solution using a nozzle with a 100 μm inner diameter, under an applied pressure of 1.05 MPa and 0.2 mm s^{-1} robot velocity. The circular tower had 1.0 mm diameter and 1.5 mm height, while the square tower had 1.0 mm side length and 1.5 mm height. Finally, Figure 4.7f presents a 3D freeform helical microstructure, which was fabricated with the 30 wt% PLA solution using a micronozzle with a 100 μm inner diameter, under an applied pressure of 1.75 MPa and 0.1 mm s^{-1} robot velocity. The pitch of the circular spiral was 0.5 mm and the radius of the coil was 0.5 mm. Consequently, the solvent-cast printing method was demonstrated to be a flexible micromanufacturing process to fabricate unique structures, giving that the process and material parameters are correctly selected. These more complex structures are generally difficult to produce by conventional single-stage processing methods.

Thermal and Crystallization Analysis

The thermal, mechanical and barrier properties of PLA are dependent on its crystalline structure and content, which are largely determined by the processing parameters.[40,41] DSC experiments were carried out to investigate the crystallization behavior of PLA filaments fabricated under various operating conditions within the range shown in Figure 4.6 for successful printing. Figure 4.8 shows the effects of the four main process parameters (*i.e.*, PLA content, applied pressure, nozzle diameter and robot velocity) on the heat flow recorded during a temperature sweep on different PLA filaments. All heat flow curves show peaks representing the glass transition (T_g), cold crystallization (T_{cc}) and melting (T_m) temperatures at approximately 65, 100, and 166 ℃, respectively. Since the T_g and T_m of PLA are strongly dependent on both the molecular weight and the optical purity (*i.e.*, fraction of the *L*-isomer lactide) of the polymer, the four process parameters had no significant effects on T_g and T_m within the range investigated. In addition, for the curves exhibiting cold crystallization at 100 ℃, a small exothermic peak (denoted as T_{exo}) prior to the melting peak was observed at 153 ℃, which is generally attributed to a transformation of the crystalline phase from the disordered α′ structure to the ordered α structure.[40,42] For PLA content

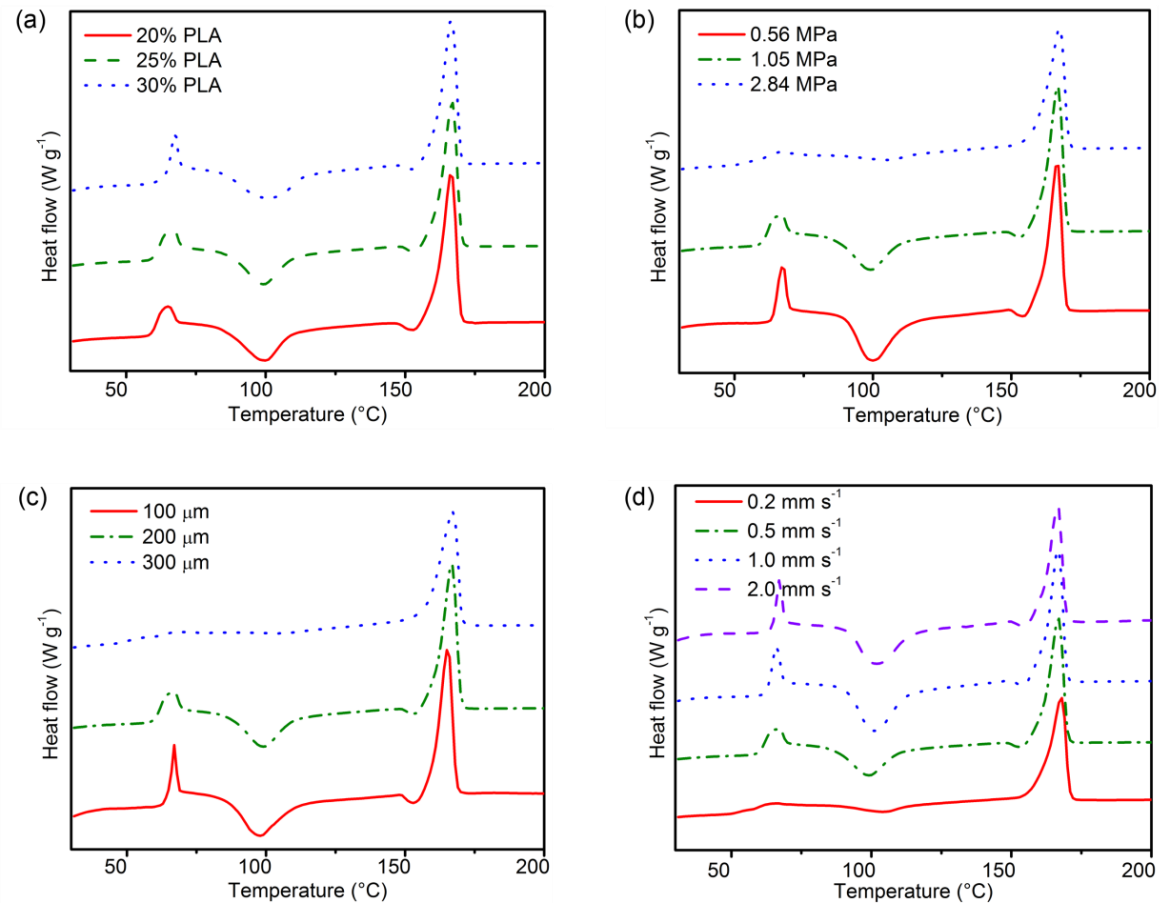

Figure 4.8 DSC thermogram of PLA filaments obtained at a heating rate of 10 ℃ min^{-1} for different printing parameters: (a) PLA content, (b) applied pressure, (c) nozzle diameter, and (d) robot velocity.

between 20 and 30 wt%, the thermograms obtained show similar trends (Figure 4.8a). Increasing the applied pressure from 0.56 to 2.84 MPa, the peak of cold crystallization decreased to nearly disappearing (Figure 4.8b). Similar evolution of cold crystallization was observed when the nozzle diameter changed from 100 to 330 μm, or the robot velocity decreased from 2.0 to 0.2 mm s^{-1} (Figure 4.8c,d). This might be due to the fact that larger applied pressure, thicker nozzle or smaller robot velocity lead to thicker filaments, which could result in lower solvent evaporation rate (Figure 4.5b) and consequently more time for polymer chains to rearrange in crystalline domains.

Table 4.1 shows the crystallization data of PLA filaments calculated from the DSC results. The melting enthalpy of the total crystalline phase (ΔH_m) corresponds to the sum of the melting enthalpies of the original crystalline phase (ΔH_{mc}) and the crystallized phase during the DSC test,

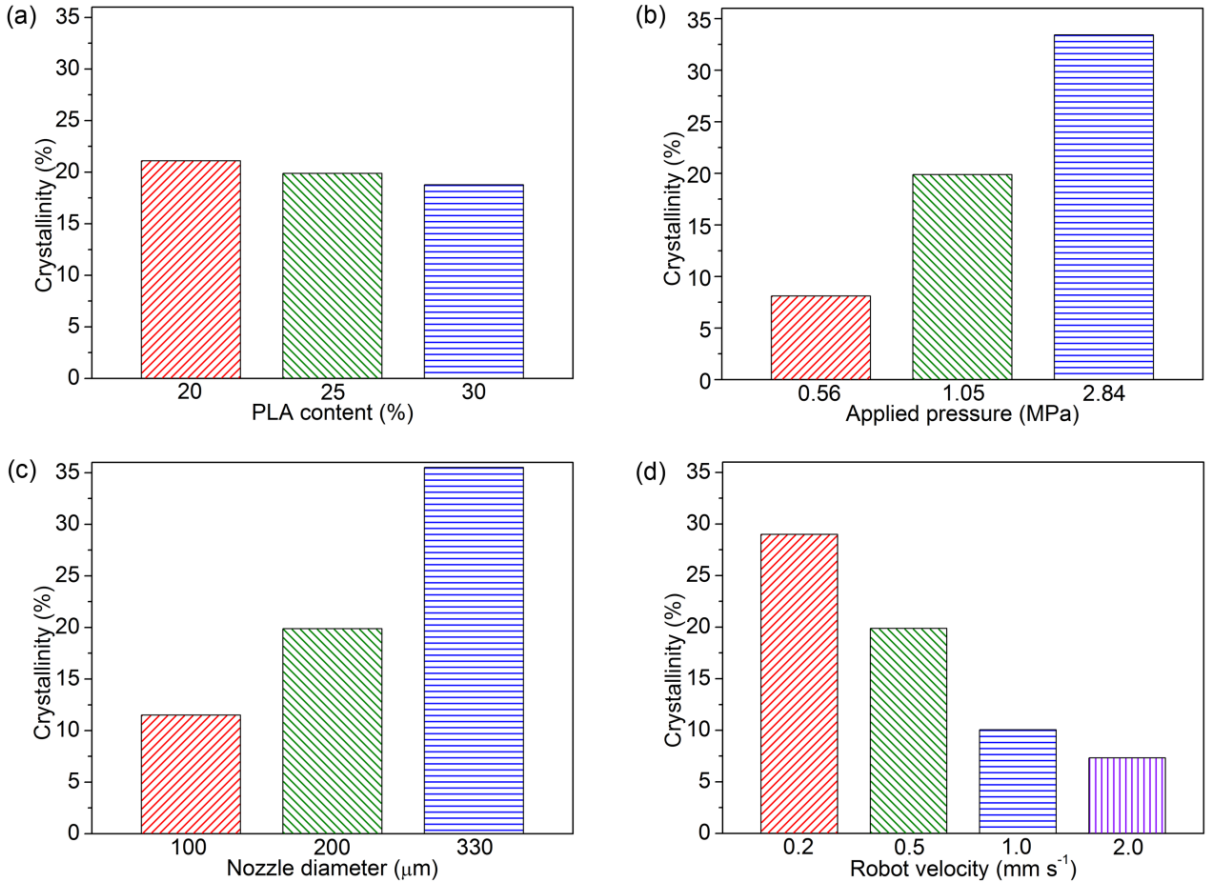

Figure 4.9 Effects of different printing parameters: (a) PLA content in solution, (b) applied pressure, (c) nozzle diameter, and (d) robot velocity on the crystallinity of PLA filaments. The data and process parameters are listed in Table 4.1.

including cold crystallization (ΔH_{cc}) and α′-to-α phase transition ($\Delta H_{\alpha\prime\to\alpha}$).[42,43] Crystallinity of the original PLA filament (χ_c), therefore, was estimated using the equation:

$$\chi_c = \frac{\Delta H_m - \Delta H_{cc} - \Delta H_{\alpha'\to\alpha}}{\Delta H_m^0} \times 100 \quad (4.7)$$

where ΔH_m^0 (93.6 J g^{-1}) is the enthalpy of fusion of 100% crystalline PLA.[44,45] Figure 4.9 shows the comparison of the crystallinity of the PLA filaments manufactured under different conditions. For the filaments made from various PLA contents but using the same processing conditions, the values of crystallinity were nearly the same (Figure 4.9a), which agrees with the results of the normalized solvent evaporation rates shown in Figure 4.5a. This may be attributed to the fact that

similar solvent evaporation time results in equivalent crystallinity evolution for the different PLA solutions. In addition, as seen in Figure 4.9(b-d), the crystallinity was significantly enhanced by increasing the applied pressure and nozzle diameter, or decreasing the robot velocity. These results are in agreement with the variation of the cold crystallization peak shown in Figure 4.8. The higher crystallinity the original filament had, the smaller cold crystallization peak in the thermogram was. Therefore, wise choice of operating conditions and ink formulation may determine the ability of PLA to complete the crystallization process during the printing stage. Furthermore, the properties of PLA structures such as heat resistance, tensile strength and barrier that benefit from high crystallization may be tuned according to the application requirements.

4.5 Conclusions

In this work, the process of solvent-cast 3D printing of PLA solutions was thoroughly investigated. Parameters such as ink rheological properties, solidification kinetics, operating conditions, and crystallinity of microstructures were examined. The PLA solutions behaved as shear-shinning fluids inside the nozzle and the process apparent viscosity was greatly dependent on the polymer content. Faster solvent evaporation could be achieved by decreasing the diameter of extrudates, which could be realized by increasing the robot velocity, or decreasing the applied pressure and nozzle diameter. However, higher crystallization of the extruded geometries could benefit from the slower solvent evaporation. As the fabrication complexity of microgeometries evolves from 1D filament, 2D fiber array to 3D scaffold and freeform spiral, the rigidity of the filament needs to increase faster as well. Thus the processing map for the most complex geometry gets narrower. The results presented in this work provide a useful insight into the whole process of solvent-cast printing and offer a general guideline for microstructures fabrication. Furthermore, this novel microfabrication approach that uses PLA solutions can be readily extended to other thermoplastic polymers and nanocomposites and enables a broad array of applications including tissue engineering scaffolds (*e.g.*, biocompatible and biodegradable 3D cylindrical meshes for stents), stimuli-responsive materials (*e.g.*, freestanding strain sensors), and microelectronic devices (*e.g.*, micro Ka band helical antenna).

ACKNOWLEDGMENT

The authors acknowledge the financial support from NSERC (Natural Sciences and Engineering Research Council of Canada) and Canada Research Chair. A scholarship for Mr. Guo

was also provided by the China Scholarship Council (CSC).

REFERENCE

1. Lebel, L. L.; Aissa, B.; El Khakani, M. A.; Therriault, D. Ultraviolet-assisted direct-write fabrication of carbon nanotube/polymer nanocomposite microcoils. Adv. Mater. 2010, 22 (5), 592-596.
2. Brown, T. D.; Dalton, P. D.; Hutmacher, D. W. Direct writing by way of melt electrospinning. Adv. Mater. 2011, 23 (47), 5651-5657.
3. Barry, R. A.; Shepherd, R. F.; Hanson, J. N.; Nuzzo, R. G.; Wiltzius, P.; Lewis, J. A. Direct-write assembly of 3D hydrogel scaffolds for guided cell growth. Adv. Mater. 2009, 21 (23), 2407-2410.
4. Zheng, J.; Xie, H.; Yu, W.; Tan, M.; Gong, F.; Liu, X.; Wang, F.; Lv, G.; Liu, W.; Zheng, G.; Yang, Y.; Xie, W.; Ma, X. Enhancement of surface graft density of MPEG on alginate/chitosan hydrogel microcapsules for protein repellency. Langmuir 2012, 28 (37), 13261-13273.
5. Gratson, G. M.; Garc á-Santamar á, F.; Lousse, V.; Xu, M.; Fan, S.; Lewis, J. A.; Braun, P. V. Direct-write assembly of three-dimensional photonic crystals: conversion of polymer scaffolds to silicon hollow-woodpile structures. Adv. Mater. 2006, 18 (4), 461-465.
6. Wu, W.; DeConinck, A.; Lewis, J. A. Omnidirectional printing of 3D microvascular networks. Adv. Mater. 2011, 23 (24), H178-H183.
7. Therriault, D.; Shepherd, R. F.; White, S. R.; Lewis, J. A. Fugitive inks for direct-write assembly of three-dimensional microvascular networks. Adv. Mater. 2005, 17 (4), 395-399.
8. Hanson Shepherd, J. N.; Parker, S. T.; Shepherd, R. F.; Gillette, M. U.; Lewis, J. A.; Nuzzo, R. G. 3D microperiodic hydrogel scaffolds for robust neuronal cultures. Adv. Funct. Mater. 2011, 21 (1), 47-54.
9. Karageorgiou, V.; Kaplan, D. Porosity of 3D biomaterial scaffolds and osteogenesis. Biomaterials 2005, 26 (27), 5474-5491.

10. Farahani, R. D.; Dalir, H.; Borgne, V. L.; Gautier, L. A.; Khakani, M. A. E.; Lévesque, M.; Therriault, D. Direct-write fabrication of freestanding nanocomposite strain sensors. Nanotechnology 2012, 23 (8), 085502.

11. Yang, W.; Ratinac, K. R.; Ringer, S. P.; Thordarson, P.; Gooding, J. J.; Braet, F. Carbon nanomaterials in biosensors: should you use nanotubes or graphene? Angew. Chem. Int. Ed. 2010, 49 (12), 2114-2138.

12. Chan, V.; Zorlutuna, P.; Jeong, J. H.; Kong, H.; Bashir, R. Three-dimensional photopatterning of hydrogels using stereolithography for long-term cell encapsulation. Lab Chip 2010, 10 (16), 2062-2070.

13. van Blaaderen, A.; Ruel, R.; Wiltzius, P. Template-directed colloidal crystallization. Nature 1997, 385 (6614), 321-324.

14. Gratson, G. M.; Xu, M.; Lewis, J. A. Microperiodic structures: direct writing of three-dimensional webs. Nature 2004, 428 (6981), 386-386.

15. Therriault, D.; White, S. R.; Lewis, J. A. Chaotic mixing in three-dimensional microvascular networks fabricated by direct-write assembly. Nat. Mater. 2003, 2 (4), 265-271.

16. Lewis, J. A. Direct ink writing of 3D functional materials. Adv. Funct. Mater. 2006, 16 (17), 2193-2204.

17. Lewis, J. A.; Gratson, G. M. Direct writing in three dimensions. Mater. Today 2004, 7 (7–8), 32-39.

18. Farahani, R. D.; Dalir, H.; Aissa, B.; El Khakani, M. A.; Lévesque, M.; Therriault, D. Micro-infiltration of three-dimensional porous networks with carbon nanotube-based nanocomposite for material design. Composites, Part A 2011, 42 (12), 1910-1919.

19. Lebel, L. L.; Aïssa, B.; Paez, O. A.; Martina, K.; Therriault, D. Three-dimensional micro structured nanocomposite beams by microfluidic infiltration. J. Micromech. Microeng. 2009, 19 (12), 125009.

20. Bruneaux, J.; Therriault, D.; Heuzey, M. C. Micro-extrusion of organic inks for direct-write assembly. J. Micromech. Microeng. 2008, 18 (11), 115020.

21. Smay, J. E.; Gratson, G. M.; Shepherd, R. F.; Cesarano, J.; Lewis, J. A. Directed colloidal

assembly of 3D periodic structures. Adv. Mater. 2002, 14 (18), 1279-1283.

22. Smay, J. E.; Cesarano, J.; Lewis, J. A. Colloidal inks for directed assembly of 3-D periodic structures. Langmuir 2002, 18 (14), 5429-5437.

23. Adams, J. J.; Duoss, E. B.; Malkowski, T. F.; Motala, M. J.; Ahn, B. Y.; Nuzzo, R. G.; Bernhard, J. T.; Lewis, J. A. Conformal printing of electrically small antennas on three-dimensional surfaces. Adv. Mater. 2011, 23 (11), 1335-1340.

24. Gratson, G. M.; Lewis, J. A. Phase behavior and rheological properties of polyelectrolyte inks for direct-write assembly. Langmuir 2005, 21 (1), 457-464.

25. Xu, M.; Lewis, J. A. Phase behavior and rheological properties of polyamine-rich complexes for direct-write assembly. Langmuir 2007, 23 (25), 12752-12759.

26. Malda, J.; Visser, J.; Melchels, F. P.; Jüngst, T.; Hennink, W. E.; Dhert, W. J. A.; Groll, J.; Hutmacher, D. W. 25th anniversary article: engineering hydrogels for biofabrication. Adv. Mater. 2013, 25 (36), 5011-5028.

27. Melchels, F. P. W.; Domingos, M. A. N.; Klein, T. J.; Malda, J.; Bartolo, P. J.; Hutmacher, D. W. Additive manufacturing of tissues and organs. Prog. Polym. Sci. 2012, 37 (8), 1079-1104.

28. Schuurman, W.; Levett, P. A.; Pot, M. W.; van Weeren, P. R.; Dhert, W. J. A.; Hutmacher, D. W.; Melchels, F. P. W.; Klein, T. J.; Malda, J. Gelatin-methacrylamide hydrogels as potential biomaterials for fabrication of tissue-engineered cartilage constructs. Macromol. Biosci. 2013, 13 (5), 551-561.

29. Drumright, R. E.; Gruber, P. R.; Henton, D. E. Polylactic acid technology. Adv. Mater. 2000, 12 (23), 1841-1846.

30. Fambri, L.; Pegoretti, A.; Fenner, R.; Incardona, S. D.; Migliaresi, C. Biodegradable fibres of poly(-lactic acid) produced by melt spinning. Polymer 1997, 38 (1), 79-85.

31. Gupta, B.; Revagade, N.; Hilborn, J. Poly(lactic acid) fiber: An overview. Prog. Polym. Sci. 2007, 32 (4), 455-482.

32. Yamada, A.; Niikura, F.; Ikuta, K. A three-dimensional microfabrication system for biodegradable polymers with high resolution and biocompatibility. J. Micromech. Microeng.

2008, 18 (2), 025035.

33. Berry, S. M.; Warren, S. P.; Hilgart, D. A.; Schworer, A. T.; Pabba, S.; Gobin, A. S.; Cohn, R. W.; Keynton, R. S. Endothelial cell scaffolds generated by 3D direct writing of biodegradable polymer microfibers. Biomaterials 2011, 32 (7), 1872-1879.

34. Vozzi, G.; Flaim, C.; Ahluwalia, A.; Bhatia, S. Fabrication of PLGA scaffolds using soft lithography and microsyringe deposition. Biomaterials 2003, 24 (14), 2533-2540.

35. Guo, S.-Z.; Gosselin, F.; Guerin, N.; Lanouette, A.-M.; Heuzey, M.-C.; Therriault, D. Solvent-cast three-dimensional printing of multifunctional microsystems. Small 2013, 9 (24), 4118-4122.

36. Gou, Z.; McHugh, A. J. Two-dimensional modeling of dry spinning of polymer fibers. J. Non-Newtonian Fluid Mech. 2004, 118 (2–3), 121-136.

37. Gou, Z.; McHugh, A. J. A comparison of Newtonian and viscoelastic constitutive models for dry spinning of polymer fibers. J. Appl. Polym. Sci. 2003, 87 (13), 2136-2145.

38. Deng, G.; Xia, Q.; Xu, Y.; Zhang, Q. Simulation of dry-spinning process of polyimide fibers. J. Appl. Polym. Sci. 2009, 113 (5), 3059-3067.

39. Kojić, N.; Kojić, A.; Kojić, M. Numerical determination of the solvent diffusion coefficient in a concentrated polymer solution. Commun. Numer. Meth. Engng. 2006, 22 (9), 1003-1013.

40. Naga, N.; Yoshida, Y.; Inui, M.; Noguchi, K.; Murase, S. Crystallization of amorphous poly(lactic acid) induced by organic solvents. J. Appl. Polym. Sci. 2011, 119 (4), 2058-2064.

41. Lim, L. T.; Auras, R.; Rubino, M. Processing technologies for poly(lactic acid). Prog. Polym. Sci. 2008, 33 (8), 820-852.

42. Zhang, J.; Tashiro, K.; Tsuji, H.; Domb, A. J. Disorder-to-order phase transition and multiple melting behavior of poly(l-lactide) investigated by simultaneous measurements of WAXD and DSC. Macromolecules 2008, 41 (4), 1352-1357.

43. Tsai, C.-C.; Wu, R.-J.; Cheng, H.-Y.; Li, S.-C.; Siao, Y.-Y.; Kong, D.-C.; Jang, G.-W. Crystallinity and dimensional stability of biaxial oriented poly(lactic acid) films. Polym.

Degrad. Stab. 2010, 95 (8), 1292-1298.

44. Fischer, E.; Sterzel, H. J.; Wegner, G. Investigation of the structure of solution grown crystals of lactide copolymers by means of chemical reactions. Colloid Polym. Sci. 1973, 251 (11), 980-990.

45. Wang, D.-Y.; Gohs, U.; Kang, N.-J.; Leuteritz, A.; Boldt, R.; Wagenknecht, U.; Heinrich, G. Method for Simultaneously Improving the Thermal Stability and Mechanical Properties of Poly(lactic acid): Effect of high-energy electrons on the morphological, mechanical, and thermal properties of PLA/MMT nanocomposites. Langmuir 2012, 28 (34), 12601-12608.

CHAPTER 5: Article 3: 3D Printing of Multifunctional Nanocomposite Helical Liquid Sensor

Shuangzhuang Guo, Xuelu Yang, Marie-Claude Heuzey and Daniel Therriault, submitted to *Advanced Materials*, May 12, 2014.

5.1 Abstract

Three-dimensional structures fabricated from electrically conductive nanocomposites may find widespread technological applications as sensors, actuators and electromagnetic interference shielding. Here, micro geometries in a freeform fashion were fabricated using solvent-cast 3D printing technique and the performance of these geometries was examined in the scope of liquid sensors in four different organic solvents (i.e. acetone, toluene, ethyl acetate, and ethanol). The helical liquid sensor featured multifunctional properties such as electrically conductivity and liquid trapping, which promoted the sensor with excellent sensitivity and selectivity, even for very short immersion time (1s) in the solvents, where the sensing response was governed by a combination of the polymer/solvent interaction parameter and the solvent vapor pressure.

5.2 Main text

Conductive polymer nanocomposites (CPNs) with relatively low loading of conductive particles such as graphene,[1] carbon nanotubes (CNT),[2] and silver nanowires[3] can benefit from multifunctional properties such as high mechanical strength and stiffness, thermal and electrical conductivity. Those properties make CPNs suitable for a broad range of applications such as sensors,[4] actuators,[5] electromagnetic interference shielding,[6] as well as energy and gas storage.[7] Among these applications, CPNs have been used for various types of sensors based on the polymer reaction to environmental changes which affects the electrically conductive particle network.[8-10] External stimuli such as temperature shift,[11] mechanical deformation,[12] and the presence of gases and vapors[13] or solvents[14] can lead to measurable electrical resistance changes of the CPNs. For example, CPNs can be used as liquid sensors since the presence of organic liquids can result in the local disconnection of electrical contacts between individual nanoparticles.[15-17] These sensory structures can provide reliable and locally resolved analysis of organic solvent leakages of tanks in ships and trucks or piping systems, or volatile organic compound detection and discrimination in air quality monitoring.[18] A few manufacturing

techniques have been reported to fabricate liquid sensors such as melt spinning,[16] and compression molding.[19, 20] However, the geometries of liquid sensors are limited to unidirectional (1D) fibers,[16] planar (i.e., two-dimensional, 2D) films[19-21] and textiles[18] , and their size are in centimeter level, which lack portability and low power consumption.

CPNs-based sensors could benefit from the ability to pattern micro-sized features in complex three-dimensional (3D) architectures. The 3D printing technique allows functional inks to be precisely patterned in filamentary form into various geometries.[22, 23] For example, thermoset polymers and their nanocomposites have been employed in UV-assisted 3D printing to fabricate microcoils[24] and strain sensors.[4] Also, a thermoplastic polymer, polylactide (PLA), has been used in solvent-cast 3D printing to build various microsystems including microstructured fibers, helical fluidic microchannels and copper plated micro-antennas.[25, 26]

In the present work, PLA/multi-walled carbon nanotubes (MWCNT) solutions were developed to fabricate helical liquid sensor in a freeform fashion using the solvent-cast 3D printing technique (Figure 5.1a). This original nanocomposite microstructure can exhibit multifunctional properties such as electrical functions (e.g., conductivity, strain sensitive resistivity), and structural functions (e.g., liquid trapping, light weight, compactness), which make it ideal candidate for liquid sensing applications. The inks were prepared by dissolving a

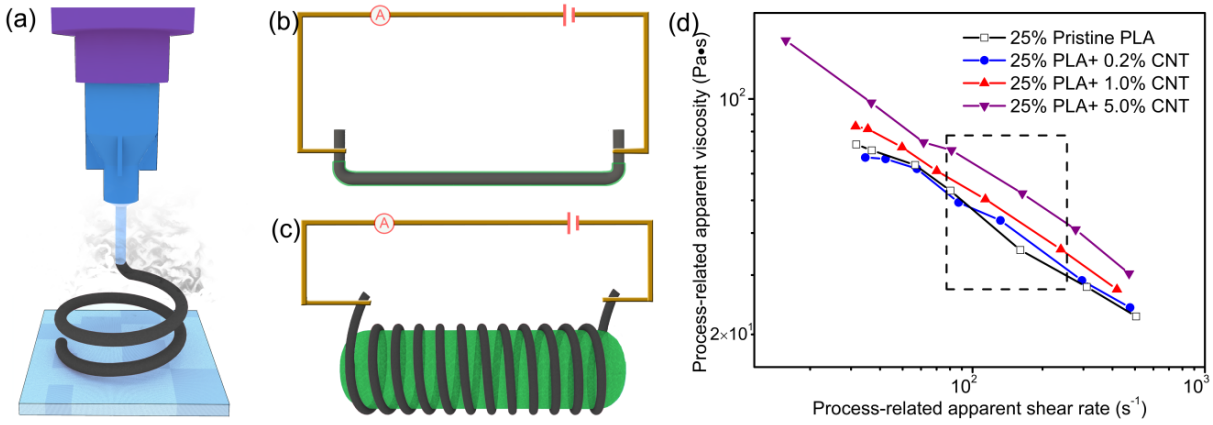

Figure 5.1 (a) Schematic representation of the solvent-cast 3D printing of nanocomposite microstructures. Schematic circuits of the liquid sensing test for (b) the straight line sensor and (c) the 3D helical sensor. (d) Process-related apparent viscosity of PLA nanocomposite solutions (typical processing window used in this work is shown by the dashed box).

masterbatch PLA/MWCNT nanocomposite in a low boiling point solvent (dichloromethane, DCM). The nanocomposite solutions were then loaded in a syringe and extruded from a micronozzle under a specific constant pressure. The rigidity of the extruded filament rapidly changed from fluid-like to solid-like due to the rapid solvent evaporation, which could lead to highly accurate freestanding features, when using the appropriately adjusted process parameters and ink properties, similar to the approach described before.[26] Two geometries, a 1D straight line and a freeform 3D helix, were fabricated and tested as liquid sensors (see Figure 5.1b,c).

The process-related viscosity of the nanocomposite inks is critical, which determines its flowing behavior inside the nozzle and the initial rigidity of the extruded filament. The CPNs-based inks exhibited shear-thinning, and the magnitude of apparent viscosity with respect to neat PLA was affected for MWCNT loading of 1 wt% and above (Figure 5.1d). The process-related apparent viscosity of the ink with 5 wt% MWCNT loading was 40% higher than that of the neat PLA ink (Figure 5.1d), which means its extruded filaments were more rigid and self-supporting. Hence, the ink (5 wt% MWCNT) could successfully be used to fabricate 3D freeform helix (Figure 5.2a) using a 150 μm inner diameter nozzle, and the typical applied pressures were between 1.4 to 2.5 MPa, which correspond to process-related shear rates of $\sim$ 80 - 220 s^{-1} (dashed box in Figure 5.1d).

The electrical property of the fabricated helix is critical in the case of sensing applications. In this solvent-cast 3D printing approach, the electrical conductivities of the extruded nanocomposite filaments showed typical concentration percolation behavior with increasing MWCNT loadings, and the electrical percolation threshold was found to be approximately 0.3 wt% (Figure 5.2b) after fitting the data using a power-law expression.[27] In order to compensate for variation of filler orientation due to processing and changes in resistivity, the filler level should be well above the percolation threshold for sensing applications.[28] In the present work the nanocomposite straight line and 3D helix were fabricated using a 30 wt% PLA solution with 5wt% MWCNT loading, approximately one order of magnitude above the percolation threshold. The measured current-voltage curve for the printed 3D helix (Figure 5.2c) showed that its electrical conductivity was about 23 S m^{-1}. Finally to demonstrate that the helix exhibited adequate mechanical stiffness and electrical conductivity, a small LED bulb (weight of 2.5 mg) could be fully lighted up under an applied voltage of $\sim$30 V (Figure 5.2d) while being supported by two

helixes.

The driving mechanisms in liquid sensing made of polymer/CNT nanocomposites are polymer matrix swelling, due to the solvent molecule penetration, and resultant disconnection of the conductive CNT network.[19] The corresponding change of resistivity is thereby related to the

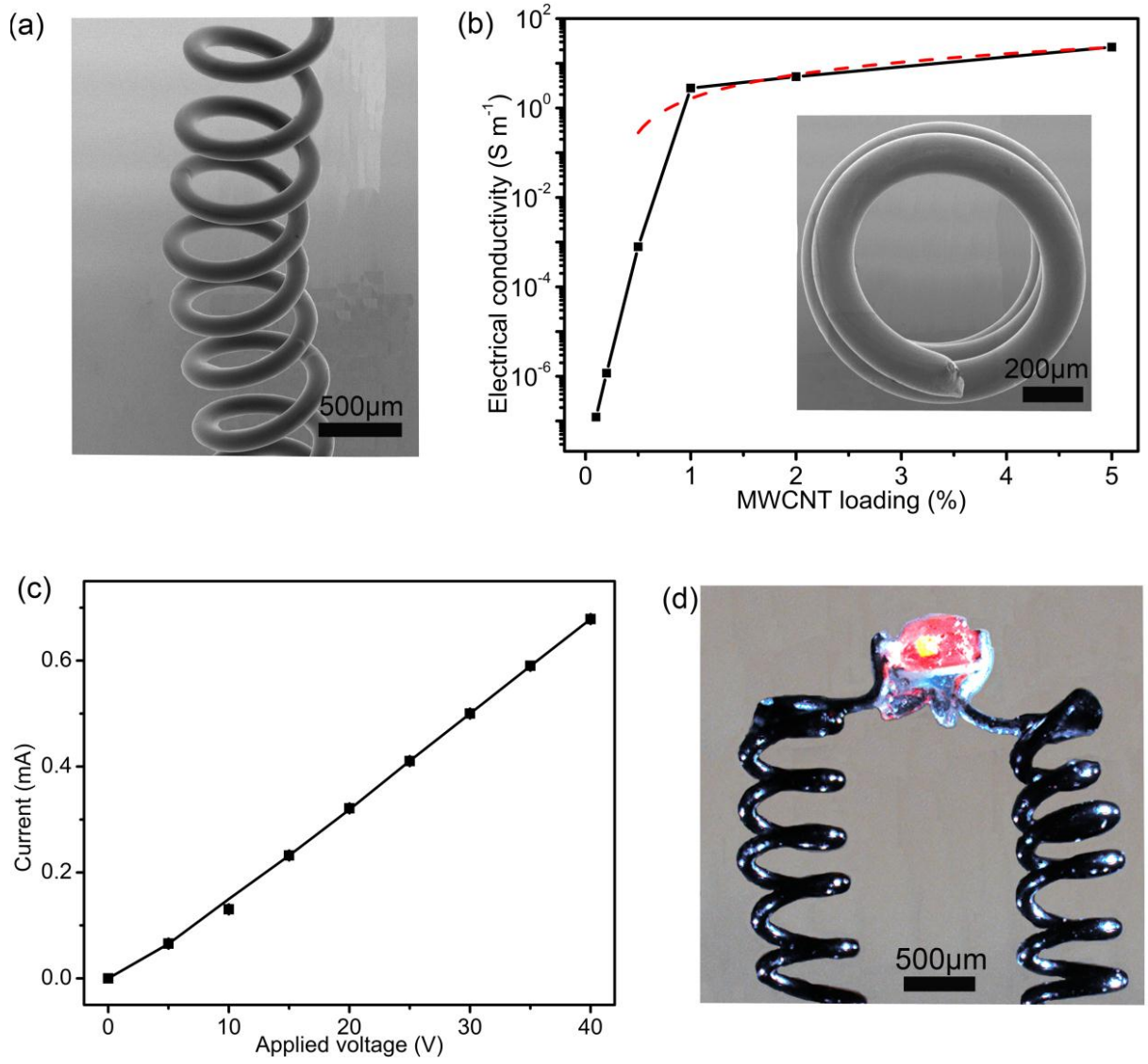

Figure 5.2 (a) Inclined side view SEM image of the nanocomposite helix. (b) Electrical conductivity of PLA nanocomposite as a function of MWCNT loading. The dashed line is a power-law expression fit[27] and the inset is a top view SEM image of the nanocomposite helix. (c) Measured current upon applied voltage between two ends of the 3D helical sensor. (d) Optical image of two helical sensors mechanically supporting and electrically sourcing a luminous LED bulb.

Table 5.1 Characteristics of PLA and solvents used for sensing experiments.[29]

Material	Solubility parameter δ_T ($MPa^{0.5}$)	Boiling point (℃)	Vapor pressure (kPa, 20 ℃)	Molar volume ($cm^3\ mol^{-1}$)	χ_{12}
Polylactide	21.2	-	-	-	-
Acetone	19.9	56.2	24.6	73.4	0.05
Ethyl acetate	18.2	77.5	9.9	98.2	0.36
Toluene	18.2	110.6	2.9	105.9	0.39
Ethanol	26.6	78.4	5.8	58.4	0.70

local volumetric solvent absorbing. When a dry CPN sensor specimen is immersed into a solvent, the swelling process starts at the material's surface and gradually develop into its core region.[18] Thus, the electrical response of the sensor depends on its geometry, the penetrating ability of the solvent and contact time.

The two different nanocomposite configurations (i.e., straight line and 3D helix) were characterized as liquid sensors in four different solvents (i.e., acetone, ethyl acetate, toluene, and ethanol) which were selected for their different solubility parameters, vapor pressures and molecular sizes (Table 5.1). The 3D helical sensor had a typical coil diameter of 1 mm and a length of 5 mm. The diameter of the filament was about 160 μm. The straight line sensor had similar filament diameter and length than the helix for comparison purposes. During the short immersion test, the sensors were cyclically immersed in a solvent at room temperature for 1 s, then taken out and left to dry in ambient air for 10 min. The change in electrical resistance of the sensors was monitored using a multimeter. In the case of the straight line sensor, a small amount of solvent remained on its surface when it was taken out of the liquid, as shown by fluorescent microscopy (Figure 5.3a). Thus the straight line sensor rapidly dried and 90% of the solvents evaporated within 10 - 40 s (Figure 5.3b), and hence led to a very short contact time with the solvents. However for the 3D helical sensor, a large amount of liquid estimated at $\sim$3.9 mm^3 was trapped inside the structure after removal from the liquid. Figure 5.3c,d show that the trapped liquid appears like a circular cylinder with a weight of $\sim$2.1 times the weight of the helix. As a

result, the helical sensor took much longer to dry (100-360 s) (Figure 5.3d). The 3D helical sensor can greatly benefit from this structural function of liquid trapping, which provides a longer contact time with the solvents. The evaporation time of the four solvents was correlated to their respective vapor pressure (Table 5.1). In other words, a higher solvent vapor pressure corresponds to a faster evaporation rate. Hence, acetone evaporated the fastest (100 s), toluene took the longest time to dry (360 s), and ethyl acetate (160 s) and ethanol (280 s) were in between the former two solvents.

The penetrating ability of a solvent is mainly determined by its interaction with the polymer, which is expressed by Flory-Huggins interaction parameter χ_{12}:

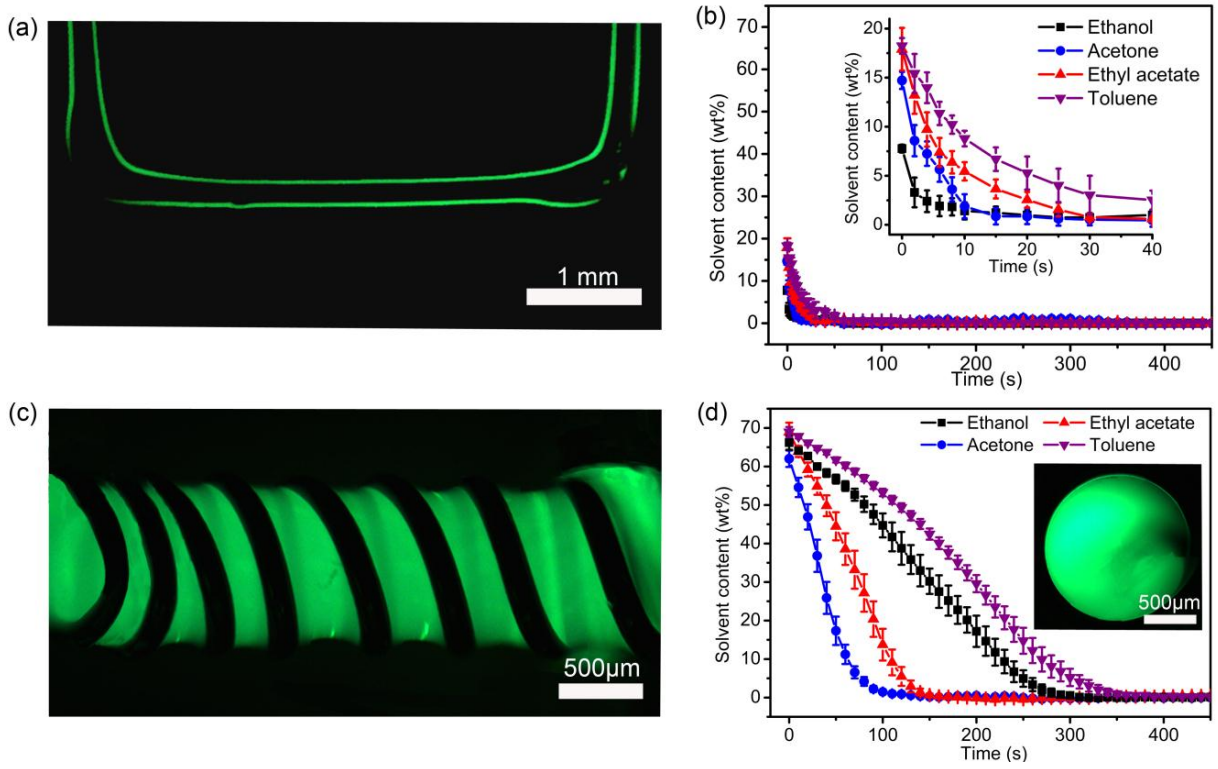

Figure 5.3 (a) Fluorescent microscopy side view image of a straight line sensor with liquid on its surface. (b) Solvent content as a function of time for the straight line sensor during drying process. (c) Fluorescent microscopy side view image of the liquid trapped in a 3D helical sensor. (d) Solvent content as a function of time for the 3D helical sensor during drying process (inset is a top view image of the helical sensor with fluorescent liquid trapped).

$$\chi_{12} = \frac{V_{sol}\left(\delta_{T\,pol} - \delta_{T\,sol}\right)^2}{RT} \quad (5.1)$$

where V_{sol} is the molar volume of the solvent, $\delta_{T\,sol}$ and $\delta_{T\,pol}$ are the solvent and polymer solubility parameters, respectively, T is the absolute temperature, and R is the ideal gas constant (R = 8.314 J K^{-1} mol^{-1}). The parameter χ_{12} was calculated for the various PLA/solvent pairs and is reported in Table 5.1. Low values of χ_{12} indicate strong interactions between the solvent and the polymer. Consequently, acetone ($\chi_{12} = 0.05$) possesses the maximum penetrating ability in PLA, ethyl acetate ($\chi_{12} = 0.36$) and toluene ($\chi_{12} = 0.39$) are almost equally second and ethanol ($\chi_{12} = 0.70$) has the lowest ability. Accordingly, amorphous PLA is known to be soluble in acetone, swells in ethyl acetate and toluene, and is insoluble in ethanol.[29]

During the short immersion cycling tests, the observed relative resistance change (R_{rel}) of the straight line sensor was inferior to 5 % for the four solvents (Figure 5.4a). The reason is that the straight line had a small amount of solvent remaining on its surface, so that the solvents evaporated very fast without obviously swelling the polymer. Besides, the similar amplitudes of the R_{rel} for the four solvents indicate that the straight line sensor had no obvious selectivity to the solvents.

Compared to the straight line sensor, the liquid sensing behavior of the 3D helical sensor was quite different under the same short immersion cycling conditions (Figure 5.4b). Its R_{rel} for toluene reached 15 % in a few seconds and decreased as the solvent evaporated. Similarly, the maximum measured amplitudes for ethyl acetate and acetone were 13.7 and 9.4 %, respectively (Figure 5.4c). Hence, the helical sensor was more than three times sensitive than the straight line sensor to these three solvents. However, the low response amplitude for ethanol (～ 1.6 %) was similar to that of the straight line sensor. The quite different responses for the four solvents mean that the helical sensor was very selective even for very short contact time. This enhanced behavior can be explained by the solvent trapping feature of the 3D helix, which prolongs the solvent interaction with the polymer. Therefore, the sensing behavior can be affected by solvent properties such as χ_{12} and vapor pressure (Figure 5.4c). Since ethanol is a poor solvent for PLA, the polymer matrix just underwent light swelling [29] and the resistance of the sensor almost did not change. While for acetone, even though it is a good solvent for PLA, the amplitude of the relative resistance change (9.4%) was smaller than that for toluene and ethyl acetate, most

probably because the faster evaporation of acetone led to shorter polymer contact time. In addition, the sensing behavior also exhibited an excellent repeatability during the five cycles tested.

However when longer immersion tests were performed, the selectivity and sensitivity of the 3D helical sensor were quite different. Figure 5.4d shows the R_{rel} of the helical sensor during five

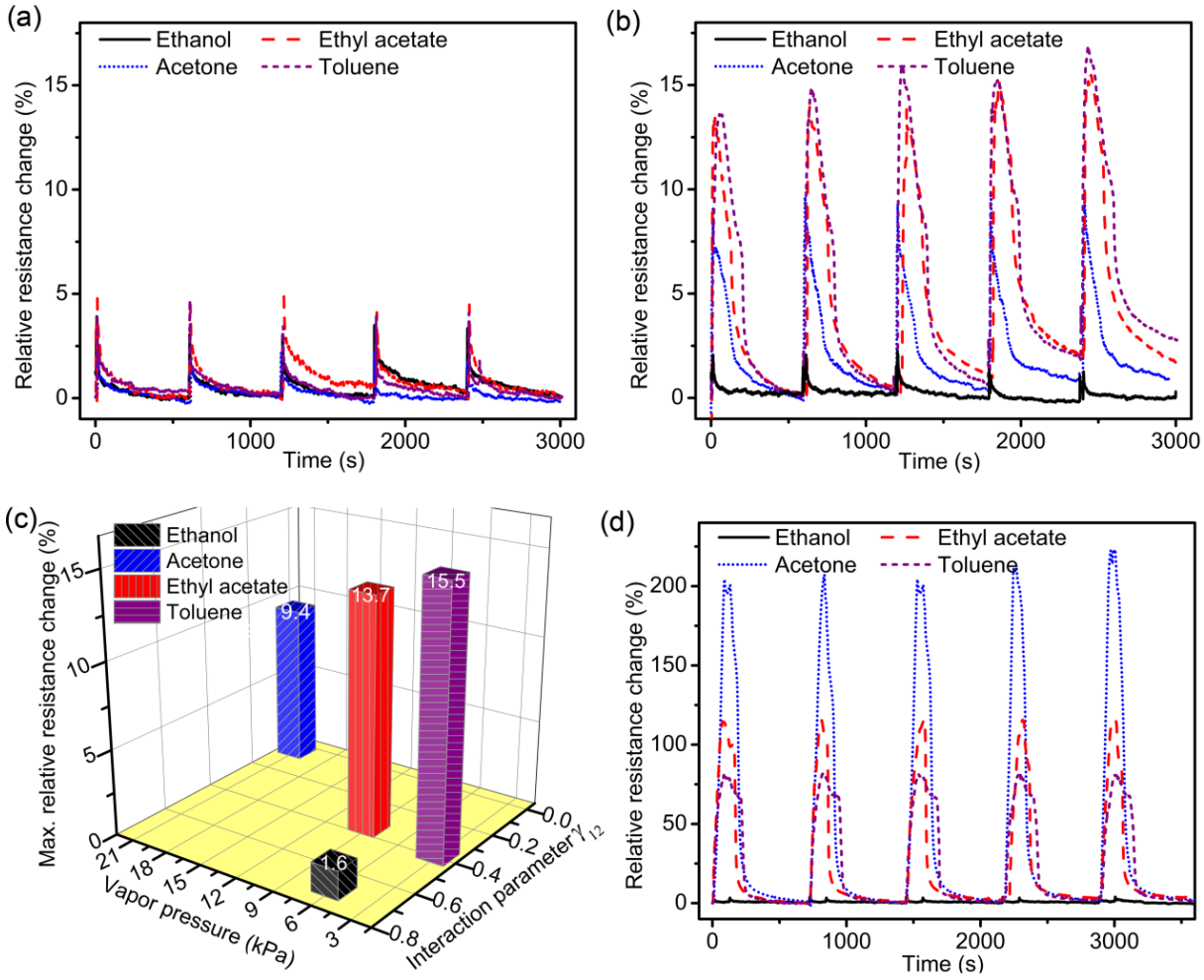

Figure 5.4 Relative electrical resistance change of (a) the straight line and (b) 3D helical sensors at short immersion cycles of (1 s) / drying (600 s) with four solvents. (c) Effect of vapor pressure and Flory-Huggins interaction parameter on the maximum relative resistance change of the helical sensor in short immersion tests. (d) Relative electrical resistance change of a 3D helical sensor during long immersion cycles of (120 s) / drying (600 s) in four solvents.

cycles of 120 s immersion in the four solvents followed by 10 min drying. The sensitivity of the sensor sharply increased, where the response amplitudes for the solvents toluene, ethyl acetate, and acetone were 81, 114, and 205 %, respectively. While the amplitudes for the ethanol slightly increased to 3.5 %. This seems to indicate that the selectivity of the 3D helical sensor is determined by the Flory-Huggins interaction parameter when in contact with a solvent for a long time (120 s vs. 1 s). Villmow et al. found that the electrical response of a polycarbonate-based sensor upon immersion into "good" solvents was governed by the solvents molecular size.[19] In other words, when the Hansen solubility parameters of the solvents were very close to each other, the selectivity of the sensor was determined by the solvent molar volume. This phenomenon is in agreement with our findings based on the expression of the Flory-Huggins interaction parameter that contains the molar volume of the solvent (Eq. (5.1).

In summary, we designed and printed a 3D liquid sensor made of a PLA/MWCNT nanocomposite in a novel freeform helical geometry. The structural feature of liquid trapping prompted the helical sensor with excellent sensitivity and selectivity, even for short immersion in the solvents, where the sensing response was governed by a combination of the polymer/solvent interaction parameter and the solvent vapor pressure. On the other hand, a straight line sensor fabricated with the same printing technique had no obvious sensing ability in short immersion tests. In addition, it was found that the sensing ability of the helix was mainly determined by the polymer/solvent interaction parameter in long immersion tests. Although the geometry of the sensor was not fully optimized and only four solvents were tested, we believe that this work opens new avenues for the 3D printing of sensing architectures from functional nanocomposite materials. This PLA/MWCNT multifunctional system not only possesses relatively high electrical conductivity, but also light weight, compactness and good mechanical stiffness coupled a structural capability fully integrated with sensing functions. Furthermore, these devices could find widely potential applications in micro- and nanoscale systems for precision measurements, human skins and person health monitoring, pollutants detection in natural environments and remote-controlled smart devices.

5.3 Experimental section

PLA/MWCNT nanocomposite inks: Pellets of polylactide (PLA 4032D, Natureworks LLC) and multi-walled carbon nanotubes (MWCNT, NC7000, Nanocyl) were dried in a vacuum oven

(G05053-10, Cole-Parmer Instrument Company) for 12 h at 50 ℃ before processing. The MWCNT had a typical diameter of 9.5 nm, average length of 1.5 μm and purity of 90 %, as provided by the manufacturer. Firstly, the PLA pellets and 5.0 wt% of MWCNT were premixed and then fed into a micro-compounder (5 mL, DSM Xplore) at 170 ℃ and 100 rpm. After a mixing time of 5 min at 180 ℃ and 300 rpm, the masterbatch of the PLA nanocomposite was extruded as strands. Then, the inks were prepared by diluting the masterbatch with desired amount of neat PLA in dichloromethane (DCM, Sigma-Aldrich) to prepare nanocomposite solutions of 30 wt% PLA concentration and various MWCNT loadings (0.1, 0.2, 0.5, 1.0, 2.0, 5.0 wt%). After dissolving for 12 h, the solution inks were stirred and sonicated in an ultrasonic bath (Ultrasonic cleaner 8891, Cole-Parmer) for 1 h. The inks were then stored in sealed bottles until processing. The process-related apparent viscosities of the inks were calculated from constant-pressure capillary flow data as described before.[26]

Solvent cast 3D printing: The deposition system consisted of a computer controlled robot (I&J2200-4, I&J Fisnar) moving a dispensing apparatus (HP-7X, EFD) along the *x*, *y* and *z* directions. The nanocomposite solution inks were housed in syringes (3 mL barrel, EFD), which were attached to a micronozzle. The 1D straight line and 3D helical sensors were fabricated with the PLA/MWCNT 5 wt% nanocomposite solution using a micronozzle with a 150 μm inner diameter (5130-0.25-B, EFD) under an applied pressure of 1.75 MPa and 0.1 mm s^{-1} robot velocity. The length of the straight line was 5 mm and the diameter of the filament was ～ 160 μm. The pitch of the helix was 0.5 mm and the radius of the coil was 0.5 mm. The morphology of the microstructures was characterized using optical microscopy (BX-61, Olympus) and SEM (JSM-7600F, JEOL. Ltd.).

Liquid evaporation tests: The drying behavior of the sensor was evaluated by resting the sensor on a high-precision balance (GH-202, A&D Engineering) right after immersion in the solvent. Firstly, the straight line and 3D helical sensors were immersed in four different solvents (i.e., acetone, toluene, ethyl acetate, and ethanol) for 1 s. Then the wet sensors were hung on a metal holder on the precision balance for 10 min to record the weight change at room temperature. Following this recording period, the sensors were dried in an oven (G05053-10, Cole-Parmer) at 50 ℃ for 5 h and weighed again. The mass of the dried sensors was then used to calculate the real-time solvent content.

Liquid sensor tests: The liquid sensing capability of the sensors was monitored by recording the resistance change during several immersion / drying cycles at room temperature. The straight line and 3D helical sensor were hung up between two copper electrical probes separated by a distance of 5 mm. Only the nanocomposite sensor part was immersed in the liquid to keep the electrodes dry. The resistance was continuously monitored using a digital multimeter (6517B, Keithley), interfaced with Lab View software. Five short immersion (1 s) / drying (600 s) cycles were periodically performed on the straight line and helical sensors in four different solvents (i.e., acetone, toluene, ethyl acetate and ethanol). Another set of immersion tests in the form of longer cycles (120 s) / drying (600 s) were also carried on the helical sensor in the four solvents. The relative resistance change R_{rel} was calculated by dividing the difference between the actual resistance (R) and the initial resistance (R_i) by R_i.

Acknowledgements

We acknowledge the financial support from NSERC (Natural Sciences and Engineering Research Council of Canada) and Canada Research Chair. A scholarship for Mr. Guo was also provided by the China Scholarship Council (CSC). We also acknowledge the technical support of Maxime Arguin from the LM^2 group during the electrical measurements.

[1] T. H. Seah, M. Pumera, *Sens. Actuators, B* **2011**, *156*, 79.

[2] J. Benson, I. Kovalenko, S. Boukhalfa, D. Lashmore, M. Sanghadasa, G. Yushin, *Adv. Mater.* **2013**, *25*, 6625.

[3] S. I. White, R. M. Mutiso, P. M. Vora, D. Jahnke, S. Hsu, J. M. Kikkawa, J. Li, J. E. Fischer, K. I. Winey, *Adv. Funct. Mater.* **2010**, *20*, 2709.

[4] R. D. Farahani, H. Dalir, V. L. Borgne, L. A. Gautier, M. A. E. Khakani, M. Lévesque, D. Therriault, *Nanotechnology* **2012**, *23*, 085502.

[5] L. Lu, J. Liu, Y. Hu, Y. Zhang, H. Randriamahazaka, W. Chen, *Adv. Mater.* **2012**, *24*, 4317.

[6] M. Mahmoodi, M. Arjmand, U. Sundararaj, S. Park, *Carbon* **2012**, *50*, 1455.

[7] M. F. De Volder, S. H. Tawfick, R. H. Baughman, A. J. Hart, *Science* **2013**, *339*, 535.

[8] J. F. Feller, J. Lu, K. Zhang, B. Kumar, M. Castro, N. Gatt, H. J. Choi, *J. Mater. Chem.* **2011**, *21*, 4142.

[9] B. Kumar, M. Castro, J. F. Feller, *Sens. Actuators, B* **2012**, *161*, 621.

[10] D. R. Kauffman, A. Star, *Angew. Chem. Int. Ed.* **2008**, *47*, 6550.

[11] Alamusi, Y. Li, N. Hu, L. Wu, W. Yuan, X. Peng, B. Gu, C. Chang, Y. Liu, H. Ning, J. Li, Surina, S. Atobe, H. Fukunaga, *Nanotechnology* **2013**, *24*, 455501.

[12] Y. Wang, A. X. Wang, Y. Wang, M. K. Chyu, Q.-M. Wang, *Sens. Actuators, A* **2013**, *199*, 265.

[13] S. J. Park, O. S. Kwon, J. Jang, *Chem. Commun.* **2013**, *49*, 4673.

[14] T. Villmow, S. Pegel, P. Pötschke, G. Heinrich, *Polymer* **2011**, *52*, 2276.

[15] K. Kobashi, T. Villmow, T. Andres, L. Häußler, P. Pötschke, *Smart Mater. Struct.* **2009**, *18*, 035008.

[16] P. Pötschke, T. Andres, T. Villmow, S. Pegel, H. Brünig, K. Kobashi, D. Fischer, L. Häussler, *Compos. Sci. Technol.* **2010**, *70*, 343.

[17] R. Rentenberger, A. Cayla, T. Villmow, D. Jehnichen, C. Campagne, M. Rochery, E. Devaux, P. Pötschke, *Sens. Actuators, B* **2011**, *160*, 22.

[18] T. Villmow, S. Pegel, A. John, R. Rentenberger, P. Pötschke, *Mater. Today* **2011**, *14*, 340.

[19] T. Villmow, A. John, P. Pötschke, G. Heinrich, *Polymer* **2012**, *53*, 2908.

[20] K. Kobashi, T. Villmow, T. Andres, P. Pötschke, *Sens. Actuators, B* **2008**, *134*, 787.

[21] P. Pötschke, K. Kobashi, T. Villmow, T. Andres, M. C. Paiva, J. A. Covas, *Compos. Sci. Technol.* **2011**, *71*, 1451.

[22] D. Therriault, R. F. Shepherd, S. R. White, J. A. Lewis, *Adv. Mater.* **2005**, *17*, 395.

[23] J. A. Lewis, *Adv. Funct. Mater.* **2006**, *16*, 2193.

[24] L. L. Lebel, B. Aissa, M. A. El Khakani, D. Therriault, *Adv. Mater.* **2010**, *22*, 592.

[25] S.-Z. Guo, F. Gosselin, N. Guerin, A.-M. Lanouette, M.-C. Heuzey, D. Therriault, *Small* **2013**, *9*, 4118.

[26] S.-Z. Guo, M.-C. Heuzey, D. Therriault, *Langmuir* **2014**, *DOI: 10.1021/la4036425*.

[27] S. Abbasi, P. J. Carreau, A. Derdouri, M. Moan, *Rheologica Acta* **2009**, *48*, 943.

[28] F. Du, J. E. Fischer, K. I. Winey, *Phys. Rev. B* **2005**, *72*, 121404.

[29] S. Sato, D. Gondo, T. Wada, S. Kanehashi, K. Nagai, *J. Appl. Polym. Sci.* **2013**, *129*, 1607.

CHAPTER 6: General Discussion

The general discussion presented in this chapter is divided into two sections. First, the 3D printing technique using thermoplastic polymers is discussed in the scope of this work. Then, the fabrication of multifunctional nanocomposites microstructures and their applications are examined in the light of the results presented in the previous chapters.

6.1 3D printing of thermoplastic polymers

In spite of the various ink materials that have been employed for the direct-write assembly (3D printing) under different shape retention mechanisms, thermoplastic polymers are still not well adapted for this technique. Few research works [19] and all the commercial 3D printers (Figure 6.1a) using thermoplastics are based on the fused deposition modeling (FDM), where the high viscosity, melting temperature and thermal degradation of the polymer during the process may limit their applications. The ink materials for the commercial 3D printers are usually limited to polylactide and acrylonitrile butadiene styrene (ABS). In order to feed the printer, the materials should be in filament form with a diameter of 1.75 mm and usually purchased from the same company as that of the printer. These features limit the printers mainly used by designer to produce printable models without functional properties (Figure 6.1b-d), ranging from toys to architectures. However, various materials such as organic fugitive or colloidal inks, concentrated polyelectrolytes and UV curable thermosets have been developed as inks for the direct ink write assembly in lab with different applications [138, 139]. The resolution of the most accurate printers is about 100 μm, and the print speed is in the range of 3 - 300 mm s^{-1} [140]. As for the direct ink write assembly, the resolution is depend on the materials and applications, which could be up to 1 μm. In addition, the 3D printer should be used to print layer-by-layer 3D geometries, while freeform structures could be fabricated using direct ink write assembly.

For successful 3D printing of microstructures, the inks should meet specific requirements in terms of rheological properties. First, the ink viscosity should be low to moderate to facilitate its extrusion through a capillary micronozzle under the attainable applied pressure. Second, the rigidity of the filament after extrusion must quickly increase for shape retention. Here, a solvent-cast 3D printing technique was developed using high concentered thermoplastic polymer solutions as inks and was described in Chapters 3-4. Under applied pressure, the polymer solution,

Figure 6.1(a) A typical commercial 3D printer. Examples of printed models (a) famous buildings in France (c) a horse, and (d) a hand ring [141].

which underwent capillary shear flow inside the micronozzle, was extruded in the filament form. Due to rapid solvent evaporation, the rigidity of the filament changed from fluid-like to solid-like, that facilitated the shape retention of the deposited geometries, even with freeform features.

In this work, the inks were prepared by dissolving PLA in a high volatile solvent dichloromethane (DCM). During the capillary flow, the PLA solutions exhibited a rheological shear-thinning behavior, which enhanced the inks processability when extruded through the micronozzle. Other process parameters such as applied pressure, nozzle diameter and robot velocity, were also critical during the fabrication. Generally, these parameters influenced the solvent evaporation rate through affecting the filament diameter, and had further impacts on the properties of the extruded structures such as shape and crystallinity. Basically, lower PLA concentration, larger applied pressure, thicker nozzle or smaller robot velocity could lead to thicker filaments, which in turn resulted in lower solvent evaporation rate.

After carefully controlling these parameters, various microstructures including 1D filament, 2D network, 3D layer-by-layer and freeform structures could be successfully fabricated. However, several challenges were faced for the fabrication of the 3D freeform structures. Because the solvent must evaporate much faster so that the geometry exhibits enough rigidity to support itself right after extrusion, it could be achieved only using much smaller nozzles ($\leq$ 100 μm), and more

viscous PLA solutions (～ 30 wt%). Besides, the applied pressure and robot velocity should be carefully adjusted to make sure the proper solvent evaporation rate.

In conclusion, the solvent-cast printing method was demonstrated to be a flexible micromanufacturing process to fabricate complex structures, which are generally difficult to produce by conventional single-stage processing methods. Furthermore, different microsystems including high-toughness microstructured fiber, microfluidic channel and micro antenna have been developed to demonstrate the fabrication capabilities of this method. However, this method uses a very high volatile solvent (DCM) to enable the fast rigidity increasing after filament extrusion, which may hamper extending this technique to other thermoplastic polymers. For the 3D printing of specific polymer insoluble in DCM, the solvent selection and process conditions should be further investigated.

6.2 Multifunctional nanocomposites microstructures and their applications

The fabrication of 3D nanocomposite microstructures implies two challenges, i. e. the preparation of the nanocomposites themselves and the fabrication of the multifunctional microstructures, which were described in Chapter 5. Melt mixing and solution processing are the two most popular methods to disperse CNTs in thermoplastic polymers. The high-shear mixing condition is provided by melt mixing to obtain the desired nanofiller dispersion. However, this method may decrease the nanofiller' aspect ratio and degrade the polymer matrix. As for the solution processing, excellent dispersion of the nanofillers requires very low viscosity solution, which is not desired in the solvent-cast printing technique. In this work, a masterbatch PLA/MWCNT nanocomposite was firstly prepared using the melt mixing process in a micro compounder. Then the inks for the 3D printing were prepared by diluting the masterbatch nanocomposite with neat PLA in DCM. This strategy could achieve excellent nanofiller dispersion without obviously degrading the polymer or handling large amount of solvent. The Figure 6.2 shows that the process-related apparent viscosity of the pristine PLA solution was about twice of that of the processed PLA solution after melt mixing process at the same shear rate, probably because the PLA underwent a thermal degradation during the processing.

Standard microfabrication techniques such as photolithography [142] and electrospinning [143, 144] possess sufficient resolution to manufacture nanocomposite microstructures for various applications. However, the materials constraint such as transparency and low viscosity limits their applications for the fabrication of CNT-based nanocomposites structures, and these techniques are less efficient to fabricate 3D complex microstructures. The solvent-cast 3D printing technique described before is a flexible, fast and cost-effective method for the fabrication of 3D nanocomposite microstructures. Interestingly, the incorporation of CNT into the polymer solutions increases their viscosity and made them more suitable than neat polymer solutions for use in this technique. The freeform helix could be fabricated using a larger diameter nozzle of 150 μm with the 30 wt% PLA nanocomposite solution (5 wt% MWCNT loading). The processability of other dilute nanocomposite solutions may be also improved, which is affected by the CNT loading and need to be further investigated.

The microstructures fabricated using electrically conductive polymer nanocomposite can benefit from multifunctional properties such as high mechanical strength and stiffness, thermal and electrical conductivity. Meanwhile, the resistance changes to external stimuli make the

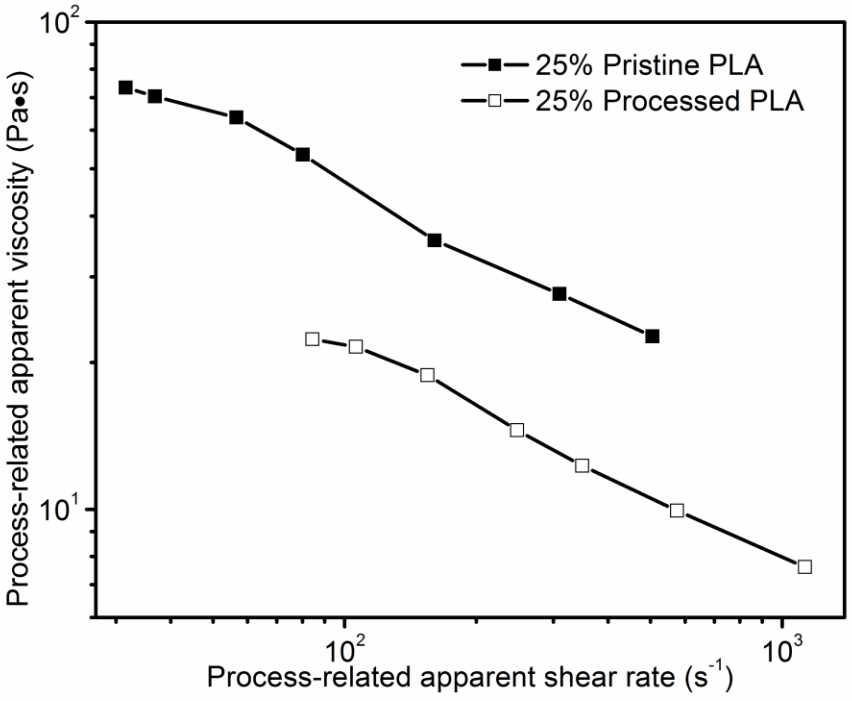

Figure 6.2 Comparison of the process-related apparent viscosity for pristine and processed PLA solutions.

nanocomposite structures suitable for use as sensors. Due to strong swelling in the organic solvents, the thermoplastic nanocomposite is a good candidate for liquid sensing. However, the geometries of liquid sensors are limited to fibers [136], films [131, 132, 135] and textiles [128]. In this work, a 3D micro helix was fabricated using the solvent-cast 3D printing method with the PLA/MWCNT nanocomposite solution as the ink. The 3D helix with a feature of liquid trapping was demonstrated to be a liquid sensor with excellent sensitivity and selectivity. In addition, a 1D straight line sensor was built and tested as control.

Generally, the liquid sensing behavior of conductive polymer nanocomposite (CPN) is determined by the affinity between the CPN and solvent, represented by the difference of Hansen solubility parameters between the polymer matrix and the solvent. However, when the solvents have a similar chemical structure (i. e. close solubility parameters), the electrical response of the CPC is governed by the solvents molecular size [8], where the relative resistance change rate decreases with increasing molecular size. In addition, the effect of temperature can be ignored when the tests are performed at room temperature. In our work, the Flory-Huggins interaction parameter χ_{12} between the solvent and polymer was used to express the dissolution behavior. The defined equation of χ_{12} as taken into account the four parameters including polymer and solvent solubility parameters, solvent molecular size and temperature. Lower values of χ_{12} indicate stronger interactions between the solvent and the polymer matrix. However, this expression was not sufficiently accurate to be correlated with the electrical response of the sensors in our work, and more research work is required. Besides, during the short immersion tests, the solvent vapor pressure also played an important role on the electrical response of the 3D helical sensor. Faster solvent evaporation led to a shorter contact time and smaller relative resistance change. In conclusion, the manufacturing technique presented here opens new prospects for the achievement of cost-effective geometry-optimized nanocomposite microdevices for microelectronics applications.

CHAPTER 7: Conclusions and Recommendations

7.1 Conclusions

In this thesis, the solvent-cast 3D printing technique was developed to fabricate various microstructures using thermoplastic polymer polylactide (PLA) and their nanocomposites solutions. The effects of polymer content, applied pressure, nozzle diameter and robot velocity on the ink viscosity, filament evaporation rate, microstructure geometry and crystallinity were characterized. In addition, electrically conductive PLA/MWCNT nanocomposite solutions were prepared using a combination of melt mixing and solution processes, and were used to manufacture multifunctional microstructures. As an example, a nanocomposite 3D spiral with a liquid trapping feature was investigated as a liquid sensor. The following conclusions are drawn from this work:

PLA solutions in dichloromethane (DCM) (20, 25, 30 wt%) behaved as shear-shinning fluids inside the nozzle and the process apparent viscosity was greatly dependent on the polymer content, while it was hardly affected by the nozzle diameter and robot velocity. Faster solvent evaporation could be achieved by decreasing the diameter of the extrudates, which could be realized by increasing the robot velocity or decreasing the applied pressure and nozzle diameter. However, higher crystallization in the extruded geometries could benefit from slower solvent evaporation.

The 30 wt% PLA solution was successfully used to fabricate 3D freeform structures because of its relatively high viscosity, while the 25 wt% PLA solution was more suitable for 2D conformal printing. As for the 20 wt% PLA solution, it was difficult to form continuous smooth filaments for all the nozzles used (inner diameter ranging from 510 to 100 μm). Hence, as the fabrication complexity of micro geometries evolved from 1D filament, 2D fiber array to 3D scaffold and freeform spiral, the rigidity of the filament needed to increase faster as well. Consequently, the processing map for the most complex geometries became narrower from Zone I to Zone III. The 3D layer-by-layer scaffold and the micro-cup were almost identical to their respective programmed deposition paths because the printing layer was supported by the underlying layer. However, the deposition of 3D freeform sharp turns lead to some geometric discrepancies.

The inks of PLA/MWCNT solutions also exhibited shear-thinning, and the magnitude of the rheological properties was affected for MWCNT loadings of 1 wt% and above. The process-related viscosity of the ink with 5 wt% MWCNT loading was 40% higher than that of the neat PLA ink. The electrical conductivity of the extruded nanocomposite filaments showed a typical nonlinear increase with MWCNT loading, exhibiting an electrical percolation threshold at about 0.3 wt% MWCNT, and the maximum conductivity was about 23 S m^{-1} with 5 wt% MWCNT loading.

The structural feature of liquid trapping prompted the PLA/MWCNT-based 3D helical sensor with excellent sensitivity and selectivity, even for short immersion time (1 s) in different solvents, where the sensing response was governed by a combination of polymer/solvent interaction parameter and solvent vapor pressure. In addition, it was found that the sensing ability of the helix was mainly determined by the polymer/solvent interaction parameter in long immersion tests (120 s).

The solvent-cast 3D printing technique developed in this work offered a low-cost, highly flexible and powerful fabrication route for microsystems featuring mechanical, microfluidic and/or electrical functionalities. The results presented here provide a useful insight on the whole process of solvent-cast printing, and offer a general guideline for microstructures fabrication. Furthermore, this novel microfabrication approach that uses PLA solutions can be readily extended to other thermoplastic polymers and nanocomposites and enables a broad array of applications.

7.2 Recommendations

The following aspects are recommended for more exploration in future work:

1) The modeling and simulation of the solvent-cast 3D printing process should be performed, which could be helpful in deeply understanding the process and predicting the time-dependent behavior of the microfabrication.

2) The effects of parameters such as PLA content, applied pressure, nozzle diameter and robot velocity on the electrical and mechanical properties of the nanocomposite structures should be characterized.

3) The nanotube orientation inside the microstructures should be systematically studied at different shear conditions, which could be used to find the correlations between the final

electrical conductivities and the process parameters.

4) The effects of geometry shape, filament diameter, CNT loading and contact time on the liquid sensing ability of the multifunctional microstructures should be further investigated.

5) The application of microfluidic channels using PLA as a sacrificial material should be systematically examined, which could be used as particle separator or self-healing network.

6) Other functional materials such as conductive polymer (Polyaniline), and visible-light curable epoxy may be developed as new inks for the 3D printing technique.

REFERENCES

[1] W. Bauhofer and J. Z. Kovacs, "A review and analysis of electrical percolation in carbon nanotube polymer composites," *Composites Science and Technology,* vol. 69, pp. 1486-1498, 2009.

[2] C. Biswas and Y. H. Lee, "Graphene Versus Carbon Nanotubes in Electronic Devices," *Advanced Functional Materials,* vol. 21, pp. 3806-3826, 2011.

[3] M. T. Byrne and Y. K. Gun'ko, "Recent Advances in Research on Carbon Nanotube–Polymer Composites," *Advanced Materials,* vol. 22, pp. 1672-1688, 2010.

[4] M. H. Al-Saleh, *et al.*, "Copper nanowire/polystyrene nanocomposites: Lower percolation threshold and higher EMI shielding," *Composites Part A: Applied Science and Manufacturing,* vol. 42, pp. 92-97, 2011.

[5] R. D. Farahani, *et al.*, "Direct-write fabrication of freestanding nanocomposite strain sensors," *Nanotechnology,* vol. 23, p. 085502, 2012.

[6] L. Lu, *et al.*, "Highly Stable Air Working Bimorph Actuator Based on a Graphene Nanosheet/Carbon Nanotube Hybrid Electrode," *Advanced Materials,* vol. 24, pp. 4317-4321, 2012.

[7] M. Mahmoodi, *et al.*, "The electrical conductivity and electromagnetic interference shielding of injection molded multi-walled carbon nanotube/polystyrene composites," *Carbon,* vol. 50, pp. 1455-1464, 2012.

[8] M. F. De Volder, *et al.*, "Carbon nanotubes: present and future commercial applications," *Science,* vol. 339, pp. 535-539, 2013.

[9] J. A. Lewis and G. M. Gratson, "Direct writing in three dimensions," *Materials Today,* vol. 7, pp. 32-39, 2004.

[10] D. Therriault, *et al.*, "Fugitive Inks for Direct-Write Assembly of Three-Dimensional Microvascular Networks," *Advanced Materials,* vol. 17, pp. 395-399, 2005.

[11] G. M. Gratson, *et al.*, "Microperiodic structures: Direct writing of three-dimensional webs," *nature,* vol. 428, pp. 386-386, 2004.

[12] J. E. Smay, *et al.*, "Directed Colloidal Assembly of 3D Periodic Structures," *Advanced*

Materials, vol. 14, pp. 1279-1283, 2002.

[13] B. Y. Ahn, *et al.*, "Printed Origami Structures," *Advanced Materials,* vol. 22, pp. 2251-2254, 2010.

[14] J. J. Adams, *et al.*, "Conformal Printing of Electrically Small Antennas on Three-Dimensional Surfaces," *Advanced Materials,* vol. 23, pp. 1335-1340, 2011.

[15] J. N. Hanson Shepherd, *et al.*, "3D Microperiodic Hydrogel Scaffolds for Robust Neuronal Cultures," *Advanced Functional Materials,* vol. 21, pp. 47-54, 2011.

[16] R. A. Barry, *et al.*, "Direct-Write Assembly of 3D Hydrogel Scaffolds for Guided Cell Growth," *Advanced Materials,* vol. 21, pp. 2407-2410, 2009.

[17] L. L. Lebel, *et al.*, "Ultraviolet-Assisted Direct-Write Fabrication of Carbon Nanotube/Polymer Nanocomposite Microcoils," *Advanced Materials,* vol. 22, pp. 592-596, 2010.

[18] R. E. Drumright, *et al.*, "Polylactic Acid Technology," *Advanced Materials,* vol. 12, pp. 1841-1846, 2000.

[19] A. Yamada, *et al.*, "A three-dimensional microfabrication system for biodegradable polymers with high resolution and biocompatibility," *Journal of Micromechanics and Microengineering,* vol. 18, p. 025035, 2008.

[20] S. M. Berry, *et al.*, "Endothelial cell scaffolds generated by 3D direct writing of biodegradable polymer microfibers," *Biomaterials,* vol. 32, pp. 1872-1879, 2011.

[21] G. Vozzi, *et al.*, "Fabrication of PLGA scaffolds using soft lithography and microsyringe deposition," *Biomaterials,* vol. 24, pp. 2533-2540, 2003.

[22] M. Jollands and R. K. Gupta, "Effect of mixing conditions on mechanical properties of polylactide/montmorillonite clay nanocomposites," *Journal of Applied Polymer Science,* vol. 118, pp. 1489-1493, 2010.

[23] F. Qin and H.-X. Peng, "Ferromagnetic microwires enabled multifunctional composite materials," *Progress in Materials Science,* vol. 58, pp. 183-259, 2013.

[24] G. Pandey and E. T. Thostenson, "Carbon Nanotube-Based Multifunctional Polymer Nanocomposites," *Polymer Reviews,* vol. 52, pp. 355-416, 2012/07/01 2012.

[25] R. Vennix. Mechanical, physical and environmental properties of materials [Online]. Available: http://www.matbase.com/index.php

[26] J. Ahmed and S. K. Varshney, "Polylactides—Chemistry, Properties and Green Packaging Technology: A Review," *International Journal of Food Properties,* vol. 14, pp. 37-58, 2010.

[27] H. A. Becerril, *et al.*, "Evaluation of Solution-Processed Reduced Graphene Oxide Films as Transparent Conductors," *ACS Nano,* vol. 2, pp. 463-470, 2008.

[28] L. T. Lim, *et al.*, "Processing technologies for poly(lactic acid)," *Progress in Polymer Science,* vol. 33, pp. 820-852, 2008.

[29] J. Ahmed, *et al.*, "Thermal properties of polylactides: Effect of molecular mass and nature of lactide isomer," *Journal of Thermal Analysis and Calorimetry,* vol. 95, pp. 957-964, 2009.

[30] K. Madhavan Nampoothiri, *et al.*, "An overview of the recent developments in polylactide (PLA) research," *Bioresource Technology,* vol. 101, pp. 8493-8501, 2010.

[31] A. Södergård, *et al.*, "Hydrolytic degradation of peroxide modified poly(L-lactide)," *Polymer Degradation and Stability,* vol. 51, pp. 351-359, 1996.

[32] A. Södergård and M. Stolt, "Properties of lactic acid based polymers and their correlation with composition," *Progress in Polymer Science,* vol. 27, pp. 1123-1163, 2002.

[33] H. Dong, *et al.*, "Chemical Treatment of Poly(lactic acid) Fibers to Enhance the Rate of Thermal Depolymerization," *ACS Applied Materials & Interfaces,* vol. 4, pp. 503-509, 2012.

[34] K. I. Park and M. Xanthos, "A study on the degradation of polylactic acid in the presence of phosphonium ionic liquids," *Polymer Degradation and Stability,* vol. 94, pp. 834-844, 2009.

[35] R. Auras, *et al.*, "An Overview of Polylactides as Packaging Materials," *Macromolecular Bioscience,* vol. 4, pp. 835-864, 2004.

[36] X. Xu, *et al.*, "Preparation of Core-Sheath Composite Nanofibers by Emulsion Electrospinning," *Macromolecular Rapid Communications,* vol. 27, pp. 1637-1642, 2006.

[37] J. J. Cooper-White and M. E. Mackay, "Rheological properties of poly(lactides). Effect of molecular weight and temperature on the viscoelasticity of poly(l-lactic acid)," *Journal of Polymer Science Part B: Polymer Physics,* vol. 37, pp. 1803-1814, 1999.

[38] L. I. Palade, *et al.*, "Melt rheology of high L-content poly (lactic acid)," *Macromolecules,* vol. 34, pp. 1384-1390, 2001.

[39] J. R. Dorgan, *et al.*, "Melt rheology of poly (lactic acid): Entanglement and chain architecture effects," *Journal of rheology,* vol. 43, p. 1141, 1999.

[40] H. J. Lehermeier and J. R. Dorgan, "Melt rheology of poly(lactic acid): Consequences of blending chain architectures," *Polymer Engineering & Science,* vol. 41, pp. 2172-2184, 2001.

[41] E. Fischer, *et al.*, "Investigation of the structure of solution grown crystals of lactide copolymers by means of chemical reactions," *Colloid & Polymer Science,* vol. 251, pp. 980-990, 1973.

[42] J. R. Sarasua, *et al.*, "Crystallinity and mechanical properties of optically pure polylactides and their blends," *Polymer Engineering & Science,* vol. 45, pp. 745-753, 2005.

[43] J. Li, *et al.*, "Crystallization morphology and crystallization kinetics of poly(lactic acid): effect of N-Aminophthalimide as nucleating agent," *Polymer Bulletin,* vol. 67, pp. 775-791, 2011.

[44] M. Pyda, *et al.*, "Heat capacity of poly(lactic acid)," *The Journal of Chemical Thermodynamics,* vol. 36, pp. 731-742, 2004.

[45] B. Kumar, *et al.*, "Poly(lactic acid)–multi-wall carbon nanotube conductive biopolymer nanocomposite vapour sensors," *Sensors and Actuators B: Chemical,* vol. 161, pp. 621-628, 2012.

[46] S. Sato, *et al.*, "Effects of various liquid organic solvents on solvent-induced crystallization of amorphous poly(lactic acid) film," *Journal of Applied Polymer Science,* vol. 129, pp. 1607-1617, 2013.

[47] F. Gardea and D. C. Lagoudas, "Characterization of electrical and thermal properties of carbon nanotube/epoxy composites," *Composites Part B: Engineering,* vol. 56, pp. 611-620, 2014.

[48] J. R. Bautista-Quijano, *et al.*, "Tensile piezoresistivity and disruption of percolation in singlewall and multiwall carbon nanotube/polyurethane composites," *Synthetic Metals,* vol.

185–186, pp. 96-102, 2013.

[49] Y. Li, *et al.*, "Electrically Conductive Polymeric Materials with High Stretchability and Excellent Elasticity by a Surface Coating Method," *Macromolecular Rapid Communications,* vol. 32, pp. 289-294, 2011.

[50] P. Costa, *et al.*, "Extruded thermoplastic elastomers styrene–butadiene–styrene/carbon nanotubes composites for strain sensor applications," *Composites Part B: Engineering,* vol. 57, pp. 242-249, 2014.

[51] J. Benson, *et al.*, "Multifunctional CNT-Polymer Composites for Ultra-Tough Structural Supercapacitors and Desalination Devices," *Advanced Materials,* vol. 25, pp. 6625-6632, 2013.

[52] M. Pluta, *et al.*, "Polylactide/montmorillonite nanocomposites: Structure, dielectric, viscoelastic and thermal properties," *European Polymer Journal,* vol. 43, pp. 2819-2835, 2007.

[53] J. H. Park and B. K. Kim, "Infrared light actuated shape memory effects in crystalline polyurethane/graphene chemical hybrids," *Smart Materials and Structures,* vol. 23, p. 025038, 2014.

[54] L. Ma, *et al.*, "Photoelectrochemical and electrochromic properties of polyimide/graphene oxide composites," *Carbon,* vol. 67, pp. 488-499, 2014.

[55] I. D. Vukoje, *et al.*, "Characterization of silver/polystyrene nanocomposites prepared by in situ bulk radical polymerization," *Materials Research Bulletin,* vol. 49, pp. 434-439, 2014.

[56]J. Liang, *et al.*, "Elastomeric polymer light-emitting devices and displays," *Nature Photonics,* vol. 7, pp. 817-824, 2013.

[57] M. H. Al-Saleh and U. Sundararaj, "A review of vapor grown carbon nanofiber/polymer conductive composites," *Carbon,* vol. 47, pp. 2-22, 2009.

[58] A. Rybak, *et al.*, "Conductive polymer composites based on metallic nanofiller as smart materials for current limiting devices," *Composites Science and Technology,* vol. 70, pp. 410-416, 2010.

[59] H. Cong and T. Pan, "Photopatternable Conductive PDMS Materials for Microfabrication,"

Advanced Functional Materials, vol. 18, pp. 1912-1921, 2008.

[60] E. S. Kim, *et al.*, "Electrospinning of polylactide fibers containing silver nanoparticles," *Macromolecular Research,* vol. 18, pp. 215-221, 2010.

[61] R. Jain, *et al.*, "Processing, Structure, and Properties of PAN/MWNT Composite Fibers," *Macromolecular Materials and Engineering,* vol. 295, pp. 742-749, 2010.

[62] M. D. Sanchez-Garcia, *et al.*, "Effect of addition of carbon nanofibers and carbon nanotubes on properties of thermoplastic biopolymers," *Composites Science and Technology,* vol. 70, pp. 1095-1105, Jul 2010.

[63] S. G. Hatzikiriakos and K. B. Migler, in *Polymer processing instabilities: Control and understanding,* S. G. Hatzikiriakos and K. B. Migler, Eds., ed: CRC, 2005, p. p87.

[64] E. Laredo, *et al.*, "AC Conductivity of Selectively Located Carbon Nanotubes in Poly(ε-caprolactone)/Polylactide Blend Nanocomposites," *Biomacromolecules,* vol. 11, pp. 1339-1347, 2010.

[65] D. S. Bangarusampath, *et al.*, "Rheology and properties of melt-processed poly(ether ether ketone)/multi-wall carbon nanotube composites," *Polymer,* vol. 50, pp. 5803-5811, 2009.

[66] T. Villmow, *et al.*, "Influence of twin-screw extrusion conditions on the dispersion of multi-walled carbon nanotubes in a poly(lactic acid) matrix," *Polymer,* vol. 49, pp. 3500-3509, 2008.

[67] D. Zhang, *et al.*, "Poly(l-lactide) (PLLA)/Multiwalled Carbon Nanotube (MWCNT) Composite: Characterization and Biocompatibility Evaluation," *The Journal of Physical Chemistry B,* vol. 110, pp. 12910-12915, 2006.

[68] S. Sinharay and M. Bousmina, "Biodegradable polymers and their layered silicate nanocomposites: In greening the 21st century materials world," *Progress in Materials Science,* vol. 50, pp. 962-1079, 2005.

[69] D. H. Park, *et al.*, "Effect of multi-walled carbon nanotube dispersion on the electrical and rheological properties of poly(propylene carbonate)/poly(lactic acid)/multi-walled carbon nanotube composites," *Journal of Materials Science,* vol. 48, pp. 481-488, 2012.

[70] R. Mathur, *et al.*, "Electrical and mechanical properties of multi-walled carbon nanotubes

reinforced PMMA and PS composites," *Polymer Composites,* vol. 29, pp. 717-727, 2008.

[71] V. Skákalová, *et al.*, "Electrical and mechanical properties of nanocomposites of single wall carbon nanotubes with PMMA," *Synthetic Metals,* vol. 152, pp. 349-352, 2005.

[72] I. Alig, *et al.*, "Conductivity spectroscopy on melt processed polypropylene-multiwalled carbon nanotube composites: Recovery after shear and crystallization," *Polymer,* vol. 48, pp. 1020-1029, 2007.

[73] H.-D. Bao, *et al.*, "Effect of electrically inert particulate filler on electrical resistivity of polymer/multi-walled carbon nanotube composites," *Polymer,* vol. 49, pp. 3826-3831, 2008.

[74] J. A. King, *et al.*, "Electrical conductivity of carbon-filled polypropylene-based resins," *Journal of Applied Polymer Science,* vol. 112, pp. 425-433, 2009.

[75] G. Liang, *et al.*, "Microstructure and properties of polypropylene composites filled with silver and carbon nanotube nanoparticles prepared by melt-compounding," *Materials Science and Engineering: B,* vol. 142, pp. 55-61, 2007.

[76] A. K. Kota, *et al.*, "Electrical and Rheological Percolation in Polystyrene/MWCNT Nanocomposites," *Macromolecules,* vol. 40, pp. 7400-7406, 2007.

[77] B. Lin, *et al.*, "Electrical, Morphological and Rheological Study of Melt-Mixed Polystyrene/Copper Nanowire Nanocomposites," *Macromolecular Materials and Engineering,* vol. 293, pp. 631-640, 2008.

[78] S. I. White, *et al.*, "Electrical Percolation Behavior in Silver Nanowire–Polystyrene Composites: Simulation and Experiment," *Advanced Functional Materials,* vol. 20, pp. 2709-2716, 2010.

[79] X. Zhang, *et al.*, "A novel low-melting-point alloy-loaded polymer composite. I. Effect of processing temperature on the electrical properties and morphology," *Journal of Applied Polymer Science,* vol. 77, pp. 1044-1050, 2000.

[80] R. A. Mrozek, *et al.*, "Highly conductive, melt processable polymer composites based on nickel and low melting eutectic metal," *Polymer,* vol. 51, pp. 2954-2958, 2010.

[81] R. Zhang, *et al.*, "Conductive network formation in the melt of carbon nanotube/thermoplastic polyurethane composite," *Composites Science and Technology,* vol.

69, pp. 1499-1504, 2009.

[82] H. Koerner, *et al.*, "Deformation-morphology correlations in electrically conductive carbon nanotube--thermoplastic polyurethane nanocomposites," *Polymer,* vol. 46, pp. 4405-4420, 2005.

[83] A. Lonjon, *et al.*, "New Highly Conductive Nickel Nanowire-Filled P(VDF-TrFE) Copolymer Nanocomposites: Elaboration and Structural Study," *The Journal of Physical Chemistry C,* vol. 113, pp. 12002-12006, 2009.

[84] M. Weber and M. R. Kamal, "Estimation of the volume resistivity of electrically conductive composites," *Polymer Composites,* vol. 18, pp. 711-725, 1997.

[85] W. Ning, *et al.*, "Partially miscible poly(lactic acid)- blend-poly(propylene carbonate) filled with carbon black as conductive polymer composite," *Polymer International,* vol. 57, pp. 1027-1035, 2008.

[86] E. Bormashenko, *et al.*, "Development of a novel composite based on polyethylene and low melting point metal alloy," in *Smart Structures and Materials 2002: Electroactive Polymer Actuators and Devices*. vol. 4695, Y. BarCohen, Ed., ed Bellingham: Spie-Int Soc Optical Engineering, 2002, pp. 465-472.

[87] X. Zhang, *et al.*, "Novel low melting point alloy-loaded polymer composite. II. Resistivity–temperature behavior," *Journal of Applied Polymer Science,* vol. 77, pp. 756-763, 2000.

[88] J. Du and H.-M. Cheng, "The Fabrication, Properties, and Uses of Graphene/Polymer Composites," *Macromolecular Chemistry and Physics,* vol. 213, pp. 1060-1077, 2012.

[89] V. Singh, *et al.*, "Graphene based materials: Past, present and future," *Progress in Materials Science,* vol. 56, pp. 1178-1271, 2011.

[90] Z. Wang, *et al.*, "Fabrication of fluorinated polyimide optical waveguides by micropen direct writing technology," *Optics and Lasers in Engineering,* vol. In Press, Corrected Proof.

[91] S. M. Berry, *et al.*, "Characterization and modeling of direct-write fabrication of microscale polymer fibers," *Polymer,* vol. 52, pp. 1654-1661, 2011.

[92] J. F. Feller, *et al.*, "Novel architecture of carbon nanotube decorated poly(methyl methacrylate) microbead vapour sensors assembled by spray layer by layer," *Journal of*

Materials Chemistry, vol. 21, pp. 4142-4149, 2011.

[93] H. He and N. J. Tao, "Electrochemical fabrication of metal nanowires," *Encyclopedia of nanoscience and nanotechnology,* vol. 2, pp. 755-772, 2003.

[94] Y.-H. Yu, *et al.*, "Morphology, Electrical, and Rheological Properties of Silane-Modified Silver Nanowire/Polymer Composites," *Macromolecular Materials and Engineering,* vol. 295, pp. 1017-1024, 2010.

[95] M. Mohamoud, "Polyaniline/poly(vinyl alcohol) (PAN/PVA) composite films: the synergy of film structural stiffening, redox amplification, and mobile species compositional dynamics," *Journal of Solid State Electrochemistry,* vol. 17, pp. 2771-2782, 2013/11/01 2013.

[96] D. Müller, *et al.*, "Chemical in situ polymerization of polypyrrole on bacterial cellulose nanofibers," *Synthetic Metals,* vol. 161, pp. 106-111, 2011.

[97] S. R. Dupont, *et al.*, "Decohesion Kinetics of PEDOT:PSS Conducting Polymer Films," *Advanced Functional Materials,* vol. 24, pp. 1325-1332, 2014.

[98] Q. Zhang, *et al.*, "Use of Dynamic Rheological Behavior to Estimate the Dispersion of Carbon Nanotubes in Carbon Nanotube/Polymer Composites," *The Journal of Physical Chemistry B,* vol. 112, pp. 12606-12611, 2008/10/09 2008.

[99] N. Grossiord, *et al.*, "On the influence of the processing conditions on the performance of electrically conductive carbon nanotube/polymer nanocomposites," *Polymer,* vol. 49, pp. 2866-2872, 2008.

[100] J.-C. Huang, "Carbon black filled conducting polymers and polymer blends," *Advances in Polymer Technology,* vol. 21, pp. 299-313, 2002.

[101] S. Abbasi, *et al.*, "Carbon Nanotube Conductive Networks through the Double Percolation Concept in Polymer Systems," *International Polymer Processing*, vol. 29, pp. 13-27, 2014/03/28 2014.

[102] C.-L. Huang and C. Wang, "Rheological and conductive percolation laws for syndiotactic polystyrene composites filled with carbon nanocapsules and carbon nanotubes," *Carbon,* vol. 49, pp. 2334-2344, 2011.

[103] S. Lordan, *et al.*, "Cytotoxic effects induced by unmodified and organically modified nanoclays in the human hepatic HepG2 cell line," *Journal of Applied Toxicology,* vol. 31, pp. 27-35, 2011.

[104] Z. Jin, *et al.*, "Poly(vinylidene fluoride)-assisted melt-blending of multi-walled carbon nanotube/poly(methyl methacrylate) composites," *Materials Research Bulletin,* vol. 37, pp. 271-278, 2002.

[105] K.-t. Lau, *et al.*, "A critical review on nanotube and nanotube/nanoclay related polymer composite materials," *Composites Part B: Engineering,* vol. 37, pp. 425-436, 2006.

[106] R. E. Conn, *et al.*, "Safety assessment of polylactide (PLA) for use as a food-contact polymer," *Food and Chemical Toxicology,* vol. 33, pp. 273-283, 1995.

[107] C. Danyluk, *et al.*, "Industrial Composting of Poly(Lactic Acid) Bottles," *Journal of Testing and Evaluation,* vol. 38, p. 7, 2010.

[108] N. G. Sahoo, *et al.*, "Effect of Functionalized Carbon Nanotubes on Molecular Interaction and Properties of Polyurethane Composites," *Macromolecular Chemistry and Physics,* vol. 207, pp. 1773-1780, 2006.

[109] J. Lei and H. Ju, "Nanotubes in biosensing," *Wiley Interdisciplinary Reviews: Nanomedicine and Nanobiotechnology,* vol. 2, pp. 496-509, 2010.

[110] Y. Qin, *et al.*, "Microfibre–nanowire hybrid structure for energy scavenging," *nature,* vol. 451, pp. 809-813, 2008.

[111] X. Lu, *et al.*, "One-dimensional conducting polymer nanocomposites: Synthesis, properties and applications," *Progress in Polymer Science,* vol. 36, pp. 671-712, 2011.

[112] F. P. W. Melchels, *et al.*, "A review on stereolithography and its applications in biomedical engineering," *Biomaterials,* vol. 31, pp. 6121-6130, 2010.

[113] J. A. Lewis, "Direct Ink Writing of 3D Functional Materials," *Advanced Functional Materials,* vol. 16, pp. 2193-2204, 2006.

[114] J. Huang, *et al.*, "Carbon nanofiber based electrochemical biosensors: A review," *Analytical Methods,* vol. 2, pp. 202-211, 2010.

[115] B. Gupta, *et al.*, "Poly(lactic acid) fiber: An overview," *Progress in Polymer Science,* vol.

32, pp. 455-482, 2007.

[116] S. Maruo and K. Ikuta, "Submicron stereolithography for the production of freely movable mechanisms by using single-photon polymerization," *Sensors and Actuators A: Physical,* vol. 100, pp. 70-76, 2002.

[117] F. P. W. Melchels, *et al.*, "A poly(d,l-lactide) resin for the preparation of tissue engineering scaffolds by stereolithography," *Biomaterials,* vol. 30, pp. 3801-3809, 2009.

[118] J. E. Smay, *et al.*, "Colloidal Inks for Directed Assembly of 3-D Periodic Structures," *Langmuir,* vol. 18, pp. 5429-5437, 2002.

[119] D. Therriault, *et al.*, "Chaotic mixing in three-dimensional microvascular networks fabricated by direct-write assembly," *Nature Materials,* vol. 2, pp. 265-271, 2003.

[120] G. M. Gratson and J. A. Lewis, "Phase Behavior and Rheological Properties of Polyelectrolyte Inks for Direct-Write Assembly," *Langmuir,* vol. 21, pp. 457-464, 2005.

[121] R. A. B. III, *et al.*, "Direct-Write Assembly of 3D Hydrogel Scaffolds for Guided Cell Growth," *Advanced Materials,* vol. 21, pp. 2407-2410, 2009.

[122] M. Bouchaar, "CONCEPTION D'UN MONTAGE DE MICROFABRICATION POUR LES NANOCOMPOSITES À BASE DE RÉSINES THERMOPLASTIQUES," MA ÎTRISE ÈS SCIENCES APPLIQUÉES, ÉCOLE POLYTECHNIQUE DE MONTRÉAL, 2011.

[123] D. R. Kauffman and A. Star, "Carbon Nanotube Gas and Vapor Sensors," *Angewandte Chemie International Edition,* vol. 47, pp. 6550-6570, 2008.

[124] Alamusi, *et al.*, "Temperature-dependent piezoresistivity in an MWCNT/epoxy nanocomposite temperature sensor with ultrahigh performance," *Nanotechnology,* vol. 24, p. 455501, 2013.

[125] Y. Wang, *et al.*, "Fabrication and characterization of carbon nanotube–polyimide composite based high temperature flexible thin film piezoresistive strain sensor," *Sensors and Actuators A: Physical,* vol. 199, pp. 265-271, 2013.

[126] S. J. Park, *et al.*, "A high-performance hydrogen gas sensor using ultrathin polypyrrole-coated CNT nanohybrids," *Chemical Communications,* vol. 49, pp. 4673-4675, 2013.

[127] T. Villmow, *et al.*, "Polymer/carbon nanotube composites for liquid sensing: Model for electrical response characteristics," *Polymer,* vol. 52, pp. 2276-2285, 2011.

[128] T. Villmow, *et al.*, "Liquid sensing: smart polymer/CNT composites," *Materials Today,* vol. 14, pp. 340-345, 2011.

[129] C. Wei, *et al.*, "Multifunctional Chemical Vapor Sensors of Aligned Carbon Nanotube and Polymer Composites," *Journal of the American Chemical Society,* vol. 128, pp. 1412-1413, 2006/02/01 2006.

[130] Q. Fan, *et al.*, "Vapor sensing properties of thermoplastic polyurethane multifilament covered with carbon nanotube networks," *Sensors and Actuators B: Chemical,* vol. 156, pp. 63-70, 2011.

[131] P. Pötschke, *et al.*, "Liquid sensing properties of melt processed polypropylene/poly(ε-caprolactone) blends containing multiwalled carbon nanotubes," *Composites Science and Technology,* vol. 71, pp. 1451-1460, 2011.

[132] T. Villmow, *et al.*, "Polymer/carbon nanotube composites for liquid sensing: Selectivity against different solvents," *Polymer,* vol. 53, pp. 2908-2918, 2012.

[133] P. Murugaraj and D. Mainwaring, "Electronic Functionality of Nanocomposites," *Advances in Diverse Industrial Applications of Nanocomposites,* vol. 23, pp. 549-578, 2011.

[134] K. Kobashi, *et al.*, "Investigation of liquid sensing mechanism of poly(lactic acid)/multi-walled carbon nanotube composite films," *Smart Materials and Structures,* vol. 18, p. 035008, 2009.

[135] K. Kobashi, *et al.*, "Liquid sensing of melt-processed poly(lactic acid)/multi-walled carbon nanotube composite films," *Sensors and Actuators B: Chemical,* vol. 134, pp. 787-795, 2008.

[136] P. Pötschke, *et al.*, "Liquid sensing properties of fibres prepared by melt spinning from poly(lactic acid) containing multi-walled carbon nanotubes," *Composites Science and Technology,* vol. 70, pp. 343-349, 2010.

[137] L. M. Bellan, *et al.*, "Current trends in nanobiosensor technology," *Wiley Interdisciplinary Reviews: Nanomedicine and Nanobiotechnology,* vol. 3, pp. 229-246, 2011.

[138] S.-Z. Guo, *et al.*, "Properties of Polylactide Inks for Solvent-Cast Printing of Three-Dimensional Freeform Microstructures," *Langmuir,* vol. DOI: 10.1021/la4036425, 2014.

[139] S.-Z. Guo, *et al.*, "Solvent-Cast Three-Dimensional Printing of Multifunctional Microsystems," *Small,* vol. 9, pp. 4118-4122, 2013.

[140] "3D printer comparison," *http://www.makershed.com/Articles.asp?ID=301*.

[141] "http://www.makerbot.com/thingiverse/."

[142] J. Yeom and M. A. Shannon, "Detachment Lithography of Photosensitive Polymers: A Route to Fabricating Three-Dimensional Structures," *Advanced Functional Materials,* vol. 20, pp. 289-295, 2010.

[143] M. Pakravan, *et al.*, "A fundamental study of chitosan/PEO electrospinning," *Polymer,* vol. 52, pp. 4813-4824, 2011.

[144] T. D. Brown, *et al.*, "Direct Writing By Way of Melt Electrospinning," *Advanced Materials,* vol. 23, pp. 5651-5657, 2011.

APPENDICES

Appendix A: Cover page of first paper in *Small*